DETERMINATION OF ABSOLUTE MATERIAL NONLINEARITY USING NONCONTACT DETECTION

A Dissertation
Presented to
The Academic Faculty

By

David Edward Torello

In Partial Fulfillment
of the Requirements for the Degree
Doctor of Philosophy in the
G.W. Woodruff School of Mechanical Engineering

Georgia Institute of Technology

August 2017

DETERMINATION OF ABSOLUTE MATERIAL NONLINEARITY USING NONCONTACT DETECTION

Approved by:

Dr. Laurence J. Jacobs, Co-Advisor
School of Mechanical Engineering
Georgia Institute of Technology

Dr. Jianmin Qu, Co-Advisor
School of Mechanical Engineering
Tufts University

Dr. Jin-Yeon Kim
School of Mechanical Engineering
Georgia Institute of Technology

Dr. Todd Sulchek
School of Mechanical Engineering
Georgia Institute of Technology

Dr. Michael Leamy
School of Mechanical Engineering
Georgia Institute of Technology

Date Approved: July 28, 2017

ACKNOWLEDGEMENTS

There is no way to possibly thank all the people that have influenced my journey through this PhD, and even if I had the space to do so I'm not entirely sure that I have the words. Eight years of living, loving, learning, succeeding, failing, and persevering has introduced me to some of the finest people this planet has to offer, and this is my meager attempt at thanking them for the impact they've had on my life.

First and foremost, Larry Jacobs - you gave me a second chance at one of the lowest points of my career, and for that alone I owe you my profound gratitude. Add to that your support through my research, always helping me see the forest for the trees (no matter how much I refused to let go. of. that. one. tree.), the hours of professional advice and counseling, and caring for me as a friend in addition to a graduate student, and I have difficulty expressing in words my appreciation and admiration. I hope that in my next steps as an educator I can provide even a shadow of your wisdom and guidance to my future students.

I would also like to thank my other committee members for their support over the years in various capacities and to varying degrees. While my co-adviser Jianmin Qu was always many states away, you always had helpful feedback, suggestions, and encouraging words at every stage of the process from publication to presentation. I'm not entirely sure that I would be confident or knowledgeable enough to call myself a doctor if not for the invaluable tutelage of Jin-Yeon Kim, without whom every doctoral and masters student passing through our lab would have been left adrift in the vast expanse of NDE literature. For every problem I had, you had three ideas to help me through, and for every idea I had, you could point out three problems to consider. There is nobody I trust more with technical (and golf) advice. I was always intimidated by the idea of nonlinear dynamics and analysis until I took a course on the subject with Michael Leamy, under whom I learned to stop worrying and love the nonlinearity. Thank you for your support and for your time in

helping me embrace the chaos. Finally, I'd like to thank Todd Sulchek, one of the very first professors that I met at Georgia Tech. You have always been a valuable source of advice, a stalwart lunch companion, and a hell of a teammate on the soccer field.

There are many other faculty at Georgia Tech that have provided me with wisdom, insight, and guidance over the years. Thank you Levent Degertekin under whom I earned a masters degree and a strong distaste for the cleanroom. Thank you to Wayne Whiteman, Aldo Ferri, Craig Forest, Wendy Newstetter, and all the other faculty who engendered my love of education and taught me that it was not only a viable career path, but a noble and worthy one as well. I cannot wait to continue my relationship with all of you as colleagues and friends.

I would like to thank the funding sources that made this research possible - the National Science Foundation, the Department of Energy Office of Nuclear Energy's Nuclear Energy University Programs, and the Electric Power Research Institute, particularly Joe Wall who is the man with the plan. I would also like to thank the powers that be in the Mechanical Engineering department who provided me with the Presidential Fellowship for my first four years as a student, and the Gilbert Amelio Fellowship for relieving the burden of starting a family and a life while living on a graduate stipend.

I would like to thank Ultran for making one hell of a transducer and Ritec for making one hell of an amplifier.

My labmates were my comrades in arms, with whom I manned the trenches and fought tooth and nail for the betterment of the scientific world. Thank you to "the Germans", who always brought a fresh pair of eyes and boundless enthusiasm for life to the lab every year. In particular, I would like to thank Sebastian Thiele for his major contributions to the early parts of my work. A special mention is required for the undergraduate students that have suffered my erratic mentoring style over the years, but who nonetheless managed to produce outstanding work worthy of awards. Harrison Bradley, your work on the Rayleigh measurements saved me countless headaches. Nicholas Selby... I don't even know where

to begin. You are my Goose, beach high five and all. Gun Kim, my coffee partner in crime at the secret garden and the guy who kept me going when times were tough. Katie Scott and Brian Fuchs, my current office mates and sanity checkers. And last but by no means least, Katie Matlack, who was an anchor in my life through some of the best, worst, and weirdest parts. You're one of the best labmates and friends that anyone could possibly wish for.

Life would be unfair without my dear friends, all of whom make the world brighter. Hommood Alrowais, Becky Katz, Barry Muldrey, Michael Giardino, Sarp Satir, Eliot Quon, Patrick Chang, David Haupt and Grace Ward, Christopher Phaneuf, Alex Coso and Scott Strong, Huy Tran, Toby Xu, Bernie Shieh, Nazli and Baris, the list goes on. Atlanta is either enriched by your presence or made much worse by your absence. Nortey Yeboah, I knew we were going to be tight after our first conversation, but I didn't know you'd ruin my life with fantasy sports. Daniel Katz and David Whitaker, my two rocks and fellow Bears. All of you - thank you, thank you, thank you.

My family is full of amazing, wonderful, loving people, all of whom I never would have survived this process without. To my Mom who is also my best friend, I promise to still call you after every soccer game. Dad - somehow being across country has made us even closer, and I treasure every conversation we have ever had. Sara - you are the coolest person I know, and I don't know how I got so lucky as to call you sister. Laura and Mike - you have become amazing adults and I feel your love always. Joe - your kindness and support is a thing of wonder. Grandma Marlene and Papa Jerry, whose warmth and pride I feel on my cheek as regular as the sun. Jay and Beth, who brought me in as their own and who keep me energized with a constant assortment of finely cooked meats. All of my aunts and uncles who make my visits home something to look forward to. And finally, to my late Grandpa Bill, who I wish could have seen me graduate but whose time was too short on this planet to do so. I love you all so much.

And finally, I want to thank my greatest love. Coffee. And also Elise, my partner in

life, crime, naps, and everything in-between. Half of this PhD belongs to you (the better half). I can't wait to begin the next chapter of my life with you at my side, Taco at my feet, and muffins along the way.

Thank you all for believing in me, my dreams, and my terrible, terrible jokes. Cheers.

TABLE OF CONTENTS

Acknowledgments iii

List of Tables xi

List of Figures xii

Chapter 1: Motivation and Objectives 1

1.1 Motivation 1

1.2 Structure of Thesis 7

Chapter 2: Review of Nonlinear Ultrasound and Experimental Techniques . . . 8

2.1 Overview 8

2.2 Second Harmonic Generation 9

2.2.1 Derivation of the Nonlinearity Parameter for Propagating Longitudinal Waves 10

2.2.2 Derivation of the Nonlinearity Parameter for Propagating Rayleigh Waves 12

2.2.3 Contributions of Microstructure to the Nonlinearity Parameter . . . 15

2.3 Ultrasonic Receivers 16

2.3.1 Contact Piezoelectric Transducers 16

2.3.2 Non-contact Receiving Technologies 20

2.4 Summary 25

Chapter 3: Source Characterization and System Nonlinearity 26

3.1 Motivation 26

3.2 Ultrasonic source characterization 27

3.2.1 Source amplitude profiles 28

3.2.2 Source linearity 34

3.2.3 System nonlinearity and windowing distortion 39

3.3 Summary 43

Chapter 4: Propagation Modeling and Nonlinear Optimization 45

4.1 Motivation 45

4.2 Longitudinal wave propagation modeling 46

4.2.1 Field modeling versus correction factors 47

4.2.2 Field modeling frameworks 49

4.2.3 Transmission of longitudinal wavefields across material interfaces . 61

4.2.4 Received pressure at surface of the air-coupled transducer 64

4.3 Rayleigh wave propagation modeling 66

4.3.1 Modeling of sample surface displacements 67

4.3.2 Modeling of leaked pressure wave from sample surface 70

4.3.3 Received pressure at surface of the air-coupled transducer 74

4.4 Inverse problem solution using nonlinear least-squares optimization 76

4.4.1 Optimization equations 76

4.4.2 Longitudinal waves 77

4.4.3 Rayleigh waves 77

4.5 Summary 80

Chapter 5: Receiver Characterization 82

5.1 Motivation 82

5.2 Self-reciprocity calibrations 83

5.2.1 Self-reciprocity calibration theory 83

5.2.2 Self-reciprocity calibration experimental setup 86

5.2.3 Results of self-reciprocity calibration 87

5.3 Model-based experimental calibration 89

5.3.1 Model-based calibration theory 90

5.3.2 Experimental Setup 94

5.3.3 Model-based calibration results 95

5.4 Summary 97

Chapter 6: Absolute Nonlinearity Parameter Measurements 99

6.1 Longitudinal wave nonlinearity parameter measurements 99

6.1.1 Experimental setup 99

6.1.2 Experimental Procedure 101

6.1.3 Data Processing 102

6.1.4 Longitudinal wave results and discussion 103

6.2 Rayleigh wave nonlinearity parameter measurements 108

6.2.1 Experimental setup and procedure 108

6.2.2 Data processing 110

6.2.3 Rayleigh wave results and discussion 111

6.3 Summary 117

Chapter 7: Conclusions and Future Work 120

7.1 Summary of Results 120

7.2 Recommendations for future work 123

7.3 Significance and Impact 125

References 125

LIST OF TABLES

3.1 Summary of nonlinearity parameters β of PZT and LiNbO3 crystals from literature. 38

4.1 Gaussian coefficients for a piston source as calculated by Wen and Breazeale for use in Eq. (4.18)[98] 57

6.1 Optimization variables for aluminum and fused silica specimens as a result of the process outlined in Sec. 4.4.2 107

6.2 Literature and current work data for nonlinearity parameter in comparable Al specimens 113

LIST OF FIGURES

1.1 Overview of steps required to obtain the absolute nonlinearity parameter, β, from air-coupled receiver SHG measurements for (a) longitudinal waves, (b) Rayleigh waves, and (c) general measurement cases. 5

2.1 Regions of effectiveness of linear and nonlinear ultrasonic methods and the types of deformations and damage to which each are sensitive and length scales at which those mechanisms occur. 9

2.2 Typical contact piezoelectric transducer setup for SHG measurements in longitudinal propagation[2]. 17

2.3 Design schematic of EMAT transducer and a comparison to the experimental configuration used in contact piezoelectric excitation[64]. 22

2.4 Rayleigh wave SHG experimental schematic for air-coupled piezoelectric receiver detection of leaked pressure waves from Rayleigh wave propagation along the sample surface. 24

3.1 (a) Typical contact piezoelectric transducer used to generate acoustic waves in SHG experiments. (b) Cut away section of a contact transducer in contact with a sample. Note the material layers between the actual transducer element and the sample, as well as the backing material behind the transducer element, both of which change the transducer frequency response and insertion losses. 27

3.2 Typical longitudinal wave NLU setup for SHG measurements. The generating transducer, labeled as ”transmitter” in (a) and (b), is a contact piezoelectric transducer that is held via a clamp to the sample. (a) shows a configuration in which the receiver is a contact transducer as well, while (b) shows an air-coupled receiver setup, which is similar except for the choice of receiver technology. 28

3.3 Experimental setup for source characterization using a laser interferometer to scan the transducer surface. 29

3.4 Results of laser interferometer scan of 5 MHz Panametrics V109 generating transducer. The transducer has a piston-like response from 1 MHz to 5 MHz. 30

3.5 Picture of the transducer/wedge assembly used to generate Rayleigh waves on a sample surface. The transducer is held in place with a clamping force provided by the screws, and the entire assembly is held in place by another clamping force. The effective source is the leading edge where the wedge meets the sample. 31

3.6 Experimental setup used to measure the transducer/wedge effective source profile with a laser interferometer. Each measurement point is signal processed in MATLAB by using a time domain Hanning window and taking an FFT to extract the fundamental and second harmonic signal content. . . . 32

3.7 Results of Rayleigh source profile measurements for the (a) fundamental and (b) second harmonic source response. The measurement error bounds for a 95 percent confidence interval (green dotted line) of the Gaussian fit (blue line) of the measured data (red dots) is shown for both frequencies. . . 33

3.8 Effect of source nonlinearity on the total measured second harmonic signal. 34

3.9 Schematic of CAN and the various states of closure of a crack or interface on the stress-strain relationship at that interface. (a) shows a crack or interface that is fully closed, (b) shows a crack or interface that is fully open, and (c) shows a crack or interface with partial closure[76] 36

3.10 Example of the nonlinearity present in an amplifier with increasing gain. The fundamental response remains linear [left], where the second harmonic generated due to nonlinearity in the amplifier changes with input level [right][5]. 40

3.11 Signal processing window FFTs for comparison of sidelobe amplitude and dropoff. In order, the window types are (a) Rectangular, (b) Gaussian, (c) Hamming, (d) Tukey 0.25, (e) Tukey 0.5, and (f) Tukey 0.75. All window responses (solid line) are superimposed over the Hanning window response (dotted line) for comparison[5]. 41

3.12 Two dimensional scans of Rayleigh wave propagation patern taken with Polytec laser interferometer used in this work. The source transducer is located to the right of the figures (a-d), and the Rayleigh wave propagates to the left. The fundamental (a and b) signals look as expected from the waveforms derived in ch. 2. However, the second harmonic (c and d) clearly doesn't increase with propagation distance, while we know this phenomenon to occur. In fact, its behavior clearly mimics the behavior of the fundamental, albeit at a reduced amplitude. The presence of this signal is masked from the demodulation noise in the Polytec interferometer. 43

4.1 Typical longitudinal wave NLU setup for longitudinal SHG measurements. The generating transducer, labeled as "transmitter", is a contact piezoelectric transducer that is held via a clamp to the sample. The receiver is an air-coupled transducer with an air gap separation from the surface of the sample. The propagation field from source to receiver must include the wavefields through both the sample and this air gap in order to provide useful information from air-coupled measurements about the state of the sample surface. 47

4.2 Geometry used in deriving the acoustic field of a baffled circular piston transducer[73]. 49

4.3 Transducer model as a superposition of an infinite number of radiating point sources. This diagram is the basis for the derivation of the RSI model[91]. . 51

4.4 Direct and edge waves generated by an impulsively excited circular piston transducer predicted by the RSI integral, as contrasted to models that only predict the direct wave components[91]. 53

4.5 (a) and (b) show the individual contributions from the individual coefficients from tab. 4.1. (c) shows a comparison of and ideal piston source in red to a 15 term MGB approximation using Eq. (4.18) in blue. (d) shows the plan view of the piston approximation. 58

4.6 Comparison of on-axis pressure fields for fundamental wave from a 15 term MGB model compared to the exact solution from the RSI model. 60

4.7 Schematic of the pressure fields for fundamental and second harmonic waves propagating through a sample. Parts and (a) and (c) show the wave fields for propagation starting at the transmitter at the bottom, traveling to the air/sample interface $(A_{\text{int},n}, B_{\text{int},n})$, transmitting into air, and impinging on the receiver surface at the top. Parts (b) and (d) show the pressure magnitude of the waves in air just after transmission across the interface calculated by Eq. (4.18) using the coefficients $(A_{\text{int},n}, B_{\text{int},n})$. Note that A_2 propagates as a second harmonic wave (Eq. (4.20)) with generation in the sample, but after transmission into the air, propagates as a fundamental wave (Eq. (4.19)). 62

4.8 Schematic of the interface between solid and air diagramming the relevant incident and transmitted waves. Note that A_2 propagates as a second harmonic wave with generation in the solid, but after transmission into the air, acts as a fundamental wave. Once the waves reach the receiver, they are integrated across the face of the transducer to obtain the force on the transducer face. 62

4.9 Contour map representation of the calculated wave fields in aluminum and air for the fundamental and second harmonic fields. The fundamental wave field for aluminum is shown in (a) and the fundamental wave field of the transmitted wave through air is shown in (b). Similarly, the second harmonic wave field in aluminum is shown in (c) and the second harmonic wave field of the transmitted wave through air is shown in (d). The contour lines are meant to highlight the diffraction and attenuation effects of the field components. 65

4.10 Model of a piezoelectric receiver for the measurement of the voltage and current when the receiver receives longitudinal acoustic waves[91]. 66

4.11 Plot demonstrating the differences in the apparent shapes of the pressure waves in the air column and the received force value when the center of the transducer is located at the same position. Both the fundamental (solid) and second harmonic (dashed) quantities are displayed. 67

4.12 Velocity distributions of the fundamental (top) and second harmonic (bottom) waves on the surface a sample modeled by eqs. (4.28) and (4.29). . . . 69

4.13 Demonstration of the physics behind leaked pressure waves from the surface of a sample as a Rayleigh wave propagates. (a) demonstrates the idea of the effects of infinite point sources acting as baffled simple sources radiating spherically into the air, forming a coherent wave front at an angle Θ_R from the vertical, and (b) shows how this sets up a propagating longitudinal wave at that same angle as the sources continue to oscillate[71]. 71

4.14 Diagramatic representation of the geometry in deriving the pressure at a point in the fluid from the combined contributions of a large number of line sources extending into the median plane[71]. 72

4.15 Comparison of the pressure field across the circular face of the receiver (left column for fundamental [top] and second harmonic [bottom]) and the projected field of view on the sample surface (right column for fundamental [top] and second harmonic [bottom]. 75

4.16 Diagrammatic representation of the curve-fitting procedure used to calculate the nonlinearity parameter of the measured specimen. (a) shows the signal from the receiving transducer (red) and the Hann window (dashed blue) used to filter it. This is processed with an FFT and (b) shows the frequency content at the fundamental (blue) and the second harmonic (red). The fundamental amplitude is then fit using Eq. (4.37) in (c), and the fit parameters $v_{0,1}$ and α_1 are extracted and used later to fit the second harmonic data. The second harmonic data without source correction is linearly fit using the first n data points (between 5 and 10) in order to get an initial value of $v_{0,2}$ to which the curve-fitting process is sensitive. This is then used in (e) to fit the A_2 data while correcting for the source nonlinearity. The resulting values of the fitting parameters are the desired results. 79

5.1 (A) Contact-transducer pitch catch operation schematic for SHG experiments. (B) Block diagram representation with the transducer conversion function between acoustic and electric energy domains[24]. 83

5.2 (A) Diagram of the receiving transducer calibration in self-reciprocity (pulse-echo) calibration. (B) Block diagram representation with the transducer conversion function for self-reciprocity calibration measurement[24]. 86

5.3 Pulse echo experimental setup for self-reciprocity calibration of the air-coupled transducer. Note that the acoustic medium in this configuration is air, and the back wall echo is off the air-metal interface. 87

5.4 FFTs of, starting from the top left and moving clockwise, the input current, the input voltage, the output voltage, and the output current read from the voltage and current probes in the experimental setup shown in Fig. 5.3. Note the irregularities of the output signals, particularly the high frequency noise and and the dual peaks near 4 MHz which are not characteristic of the NCT4-D13 transducer. 88

5.5 Result of self-reciprocity calibration from the pulse-echo experimental setup shown in Fig. 5.3 of the air-coupled transducer. Of note are the erroneous peaks around 4.2 MHz and the anti-resonance near 3 MHz, neither of which are characteristics of the NCT4-D13 transducers. 89

5.6 Experimental setup for model-based calibration method, using a commercial contact transducer coupled to an aluminum sample as the "calibrated reference sample". 91

5.7 (a) Data taken by laser interferometer [red line] compared to the MGB source model predicted by Eq. (4.18) [blue line] at 2 MHz. (b) Sample surface [right] compared to the modeling output of the source conditions [left] shown on the sample surface for the same measurement conditions as (a). 92

5.8 Maximum velocity amplitudes for calibration reference sample over the range of frequencies from 1 MHz to 6 MHz, which are then used to propagate acoustic waves through air to the receiver surface. 93

5.9 Modeling results and measurement scans from a frequency range of 2 to 5 MHz at 1 MHz increments. The first row contains the results from the lowest frequency and the last row contains the results from the highest frequency. The columns illustrate, from left to right, the laser scan of the aluminum calibration specimen surface at the interface between aluminum and air (plan view), the modeled pressure field in the air from sample surface to receiver surface (section view), and the result of the air-coupled transducer scan of the received pressure waves (plan view). The results in this figure highlight the quantitative and qualitative changes in the wave forms as the frequency of the input changes, most notably the decreasing radius of the main lobe in the measured results with increasing frequency. 96

5.10 Calibration curve for the Ultran NCT4-D13 air-coupled transducer which allows for the conversion from the measured transducer output voltage (V) to the received force on the transducer surface (F) in Newtons. 97

6.1 Typical longitudinal wave NLU setup for longitudinal SHG measurements. The generating transducer, labeled as "transmitter", is a contact piezoelectric transducer that is held via a clamp to the sample. The receiver is an air-coupled transducer with an air gap separation from the surface of the sample. The propagation field from source to receiver must include the wavefields through both the sample and this air gap in order to provide useful information from air-coupled measurements about the state of the sample surface. 100

6.2 Air-coupled transducer and laser interferometer scan results of aluminum and fused silica specimens. The aluminum fundamental (a) and second harmonic results (e) show strong radial symmetry characteristic of an accurate alignment of the air-coupled receiver. This is highlighted by the similarity to the laser interferometer scan results shown in (b) and (f). The air-coupled measurements in fused silica at the fundamental (c) and second harmonic (g) frequencies show more asymmetry in the second harmonic measurement as contrasted to the laser interferometer measurements in (d) and (h), indicating that improvements can be made to the air-coupled receiver alignment. These air-coupled measurements demonstrate what the air-coupled receiver "sees" when it area-weights the pressure field in air at each scan location. 103

6.3 Results of the nonlinear curve-fitting operation in aluminum and fused silica. The aluminum fundamental results (a) show very close alignment between the measured (red circle with error bars) and curve-fit (blue solid line) results, while the second harmonic (b) demonstrates very accurate results in the main lobe but differences in the side lobe amplitudes. The fused silica fundamental (c) is similarly accurate, while the second harmonic results (d) look much more like the modeling picture. The high variation in the fused silica data around the 5 mm measurement point is due to surface defects in the reflective tape used to make the laser interferometer measurement. 105

6.4 Nonlinear ultrasound testing results for the Al 2024 and 7075 samples. (a) and (b) show the fundamental amplitudes for the 2024 and 7075 specimens respectively. (c) and (d) show the second harmonic amplitudes for the 2024 and 7075 specimens respectively. Data points and best-fit lines from the optimization process outlined in figure 4.16 are shown for each case 111

6.5 (a) shows a set of nonlinear measurements versus propagation distance for a 2205 SS sample heat treated over 24 hours. The red dotted line shows a linear fit to the "linear region" of the data, which is identified subjectively. The black dash-dotted line represents the results of the nonlinear fitting procedure. (b) shows the results of 2205 duplex stainless steel nonlinear parameter measurements as a function of heat treatment time for both the original analysis using a linear fitting approach (Ruiz et al) and the nonlinear fitting approach (current work). The data point labeled (*) represents data collected at 10 minutes, and the data point labeled (**) represents data collected at 24 hours. The β_{11} values represented by each fitting procedure in (a) can clearly be seen as the last data point in (b). 119

SUMMARY

Quantitative evaluation of the microstructural state of a specimen can be deduced from knowledge of the sample's absolute acoustic nonlinearity parameter, β, making the measurement of β a powerful tool in the NDE toolbox. However, the various methods used in the past to measure β each suffer from significant limitations. Piezoelectric contact transducers are sensitive to nonlinear signals, cheap, and simple to use, but they are hindered by the variability of the interfacial contact between transducer and specimen surface. Laser interferometry provides non-contact detection, but requires carefully prepared specimens or complicated optics to maximize sensitivity to the higher harmonic components of a received waveform. Additionally, laser interferometry is expensive and relatively difficult to use in the field. Air-coupled piezoelectric transducers offer the strengths of both of these technologies and the weaknesses of neither, but are notoriously difficult to calibrate for use in nonlinear measurements.

This work proposes a hybrid modeling and experimental approach to air-coupled transducer calibration and the use of this calibration in a model-based optimization to determine the absolute β parameter of engineering materials. This approach is used to measure β in longitudinal wave second harmonic generation experiments by testing samples of aluminum and fused silica, which are both well-documented materials and provide a strong reference for comparison of experimental and modeling results. This work also proposes adaptations to current measurement techniques using Rayleigh waves by accounting for diffraction and attenuation affects, as well as source nonlinearity and their effects on the measured acoustic nonlinearity parameter β_{11}. Ultimately, this thesis provides a much needed tool in the NDE toolbox for measuring absolute material nonlinearity using a receiver type that has the potential to take NLU measurements from the lab to the field.

CHAPTER 1
MOTIVATION AND OBJECTIVES

1.1 Motivation

Nonlinear ultrasonic (NLU) techniques are an important part of the nondestructive evaluation (NDE) toolkit and have been successfully used to characterize material defects and microstructural evolution through various aging and deformation mechanisms such as fatigue[1–4], cold work[5], thermal aging[6, 7], creep[8], and radiation exposure[9] dating as far back as the 1960s[10–17]. These measurements all seek to capitalize on the change in the nonlinear stress-strain relationship that occurs as a material undergoes microstructual changes by measuring the distortion of ultrasonic waves as they propagate through the sample. Second harmonic generation (SHG) is a technique in the field of NLU where a monotonic ultrasonic input generates additional waves at harmonics of the input frequency as it propagates through the specimen. The second harmonic wave amplitude (A_2) is compared to the square of the fundamental amplitude (A_1^2), and the ratio of these two amplitudes is proportional to the acoustic nonlinearity parameter β. This β value can be correlated to the change in material microstructure due to external effects, and when this parameter is tracked over time or damage evolution, a useful picture of the material life (past and remaining) can be constructed that may inform engineering decisions regarding a variety of materials and situations such as replacement of near-failure components and structures or remedial action to change or prevent loading conditions leading to material degradation.

In order to determine the state of a material sample, tests are often performed relative to a base, unaltered state and the SHG measurements are tracked as the material state evolves[9, 18–20]. This type of measurement is referred to as a relative nonlinearity measurement and is typically performed with uncalibrated acoustic transducers that measure

the relative acoustic nonlinearity parameter β^*. This approach is used simply because the absolute signal amplitudes do not matter when the change in those amplitudes is the desired measurement result, which is often the case when a record of previous tests exist for unaltered material and structures. Relative nonlinearity measurements are fairly straightforward to make and for this reason they are preferred if the corresponding set of measurements to compare to exists. That being said, there are many situations in which this condition cannot be met such as in existing transportation or public utilities infrastructures. In these cases, approaching a sample with no prior knowledge of the material requires the measurement of the absolute nonlinearity parameter β, which can be used to predict material state through modeling and, by extension, remaining material life.

Many receiver technologies exist that can easily provide relative SHG measurements effectively and cheaply, most notably contact piezolectric transducers[2, 9, 18, 21]. These piezoelectric devices exhibit high sensitivity and desirable electronic and mechanical properties for use in NLU experiments, but because they are resonant devices they exhibit frequency dependent electroacoustic transfer functions that must be known to accurately interpret their responses to ultrasonic inputs[22, 23]. Contact piezoelectric transducers can be calibrated to provide absolute signal measurements[24–26], but there are some significant limitations associated with these calibrations. First, the calibration of contact transducers is dependent on the interface conditions between the transducer and the sample, typically through a fluid couplant layer, which is extremely difficult to control. Because the transducer and fluid couplant layer are calibrated together, a new calibration must be performed every time the couplant layer changes, which occurs with every new contact measurement and greatly limits measurement reproducability. Additionally, if the coupling of the transducer and the sample is poor, the electroacoustic transfer function obtained from experiment may be meaningless because of poor signal quality, harmonic generation from contact, or increased insertion losses[27–29]. While absolute measurements with contact piezoelectric transducers are certainly possible[2], a much more effective and robust ap-

proach is the use of non-contact receivers to measure the fundamental and second harmonic wave amplitudes.

Non-contact detection has been used for performing absolute SHG measurements with many receiving technologies, including capacitive electrostatic transducers[7, 17, 30–32], EMATs[33, 34], and laser interferometers[21, 31, 35, 36]. These techniques all have their advantages and disadvantages, but when it comes to measuring across a variety of samples under in-situ conditions with the greatest ease, laser interferometry is the most effective of these technologies. They offer a flat and broadband measurement bandwidth and give absolute displacement information with pre-determined calibration information requiring little to no user input. However, laser interferometers are expensive, bulky, and benefit from highly polished samples or reflective surfaces for effective use in detecting higher harmonic waves[35, 37] which ultimately detracts from their usefulness in field applications.

A very attractive alternative to laser interferometry is the use of air-coupled piezoelectric transducers, which exhibit the high sensitivity and low relative cost of contact piezoelectric transducers, and are well adapted for use in in-situ applications where laser interferometry would struggle. Electromechanical calibration of the transducer has proven elusive for use in SHG measurements up to this point, but because the couplant in this case is a repeatably controllable air gap, a single calibration of the transducer remains viable for all subsequent measurements given consistent environmental factors. This work provides the necessary theoretical and experimental frameworks to adapt air-coupled transducers for use in measuring absolute β, equipping the NDE community with a much needed tool for absolute NLU inspection of previously difficult to measure specimens in a broader variety of experimental conditions. **Therefore the overall objective of this work is to use air-coupled piezoelectric receivers to measure the absolute nonlinearity parameter of sample materials using SHG techniques.**

This objective is accomplished in three major steps, each of which is outlined individually in corresponding chapters of this dissertation, and the progression of these steps

is shown in fig. 1.1 below. First, the acoustic source must be modeled in order to pick an appropriate propagation modeling framework. Second, the acoustic wave propagation must be modeled and set up in such a way that it can be used to solve the inverse problem of relating measurements to material parameters. Finally, the acoustic receiver must be characterized in order to measure absolute acoustic displacements and velocities, which will make the measured values of β absolute quantities. Each of these steps is explained in more detailed below for the longitudinal wave measurement case (a), the Rayleigh wave measurement case (b), and the general process flow (c).

Step 1: Characterize ultrasonic sources for use in NLU measurements

To address this goal, a laser interferometer was used to determine the magnitude and phase characteristics of the ultrasonic source to identify the acoustic linearity and the amplitude distribution across the transducer profile. For the case of bulk wave measurements, the piezoelectric contact transducer source is in direct contact with the sample under test, so laser scans were conducted of the transducer face and a uniform piston like behavior was observed, allowing for the use of the uniform piston assumption in modeling. The Rayleigh wave case is more complicated, but an effective source location and amplitude profile was obtained and found to be Gaussian in nature, greatly simplifying the surface wave field modeling across the specimen surface. The linearity of the sources was examined and the effects of the source nonlinearity were measured and decoupled from the data using a nonlinear optimization algorithm, resulting in the separation of the source nonlinearity amplitude A_2^T from the material nonlinearity amplitude A_2^M, an essential step in the calculation of the absolute nonlinearity parameter. An examination of the use of the spectrally pure sources in the form of Lithium Niobate (LiNbO3) discs was conducted and was found to reduce the system nonlinearity significantly in the measurement, enabling more accurate detection of nonlinearity originating from material properties by minimizing A_2^T.

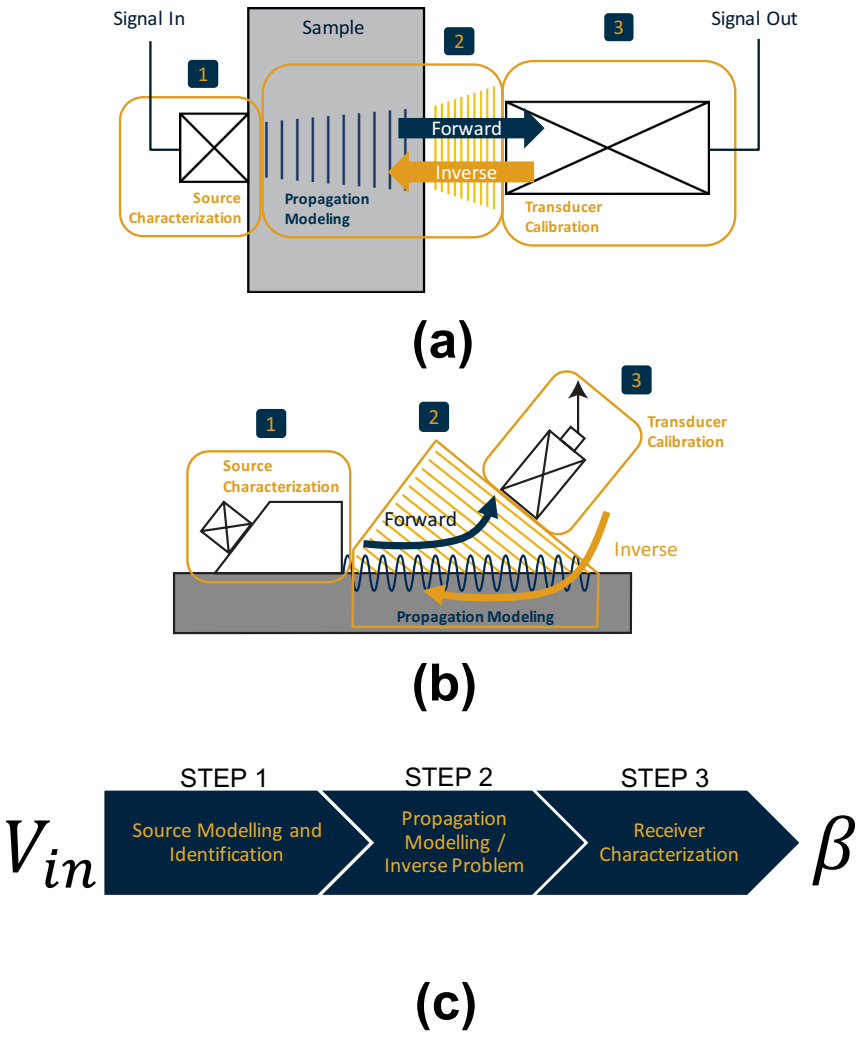

Figure 1.1: Overview of steps required to obtain the absolute nonlinearity parameter, β, from air-coupled receiver SHG measurements for (a) longitudinal waves, (b) Rayleigh waves, and (c) general measurement cases.

Step 2: Develop a nonlinear ultrasonic propagation model for waves through a solid and use it in an inverse problem solving algorithm to extract β from experimental data

To address this goal, several modeling approaches were developed to calculate the pressure and velocity wave fields in bulk and Rayleigh wave propagation conditions. In the bulk wave case, the method of multiple Gaussian beams was employed to create a fast

and efficient model for computing the linear and nonlinear portions of the wave field due to a propagating fundamental wave. This model was compared to experimental data and found to be in good agreement with measurements taken with a laser interferometer. In the Rayleigh wave case, a surface wave propagation model was developed by Shull et al. to model the velocity distribution across a sample and was found to be in good agreement with data. This information was then used to calculate the propagation of the sound wave through air to the air-coupled piezoelectric receiver using the Rayleigh Sommerfeld Integral approach, which is accurate but computationally very costly. These forward propagation models were then utilized in a nonlinear optimization algorithm to solve the inverse problem, starting with measured voltages from an air-coupled receiver and calculating the corresponding surface velocities and pressures.

Step 3: Characterize air-coupled piezoelectric transducers for use in NLU measurements

To address this goal, a hybrid experimental/model-based approach was employed to provide a transfer function between the received force on the surface of the air-coupled transducer and the output voltage from the transducer electrical port. The experimental portion of the calibration was confirmed with laser interferometric measurements of the surface displacement on a reference aluminum sample excited with a calibrated contact piezoelectric transducer. These surface displacements were used to provide inputs to a bulk wave beam field model based on the multiple Gaussian beam (MGB) formulation. The calibrated air-coupled transducer sensitivity was applied to air-coupled transducer measurements and used in the inverse problem solution algorithm outlined in objective 2 and the absolute nonlinearity parameter was obtained.

1.2 Structure of Thesis

This dissertation is organized as follows. This chapter introduces the topic of absolute nonlinearity measurement and nonlinear ultrasonic methods and outlines the goals of the research as well as a brief summary of the work. Chapter 2 provides an in-depth discussion of previous work, the state of the art in NDT, and the necessary background in NLU, transducer technologies, and propagation modeling to inform the rest of the work. Chapter 3 will discuss the challenges and methods pertinent to source characterization and the effects of and corrections for system nonlinearity present in NLU measurements. Chapter 4 will discuss methods and procedures in propagation modeling and the use of nonlinear optimization algorithms to extract values of β from experimental results. Chapter 5 will present receiver characterization challenges and discuss methods for overcoming calibration difficulties with non-contact transducers. Chapter 6 will discuss the experimental setups required to determine β from real samples and present experimental results for various materials and measurement configurations. Finally, chapter 7 will present a discussion of the results and chapter 8 will provide conclusions and a discussion of future work for further explorations in this field.

CHAPTER 2
REVIEW OF NONLINEAR ULTRASOUND AND EXPERIMENTAL TECHNIQUES

2.1 Overview

Nonlinear ultrasound (NLU) is a set of NDE techniques that monitors strength based parameters of materials and is sensitive to microstructural changes and material defects. These microstructural features are often precursors to macroscopic damage, and it is therefore useful to think of NLU testing as a way to tell when something is *beginning* to fail as opposed to *already* failing. The intent is to therefore use NLU measurements to enable engineers to take remedial steps to address design and material issues before those steps become too costly of otherwise difficult to carry out. NLU is thus useful to engineers and technicians in ways that linear ultrasonic (stiffness-based) methods that detect macro-scale damage like crack formation are not. Because propagating ultrasonic signals contain both the linear and nonlinear information, NLU methods are in many cases a supplemental form of measurement done in parallel with linear operations like time-of-flight (velocity) and attenuation measurements. However, NLU loses its usefulness when failure has already occurred or the size of the flaws and defects are on the order of the ultrasonic wavelength of the probing signal. NLU shines when the defects or changes are sub-wavelength in scale, which is when linear methods no longer provide useful information. Figure 2.1 details the useful length scales and types of damage to which linear and nonlinear methods are sensitive.

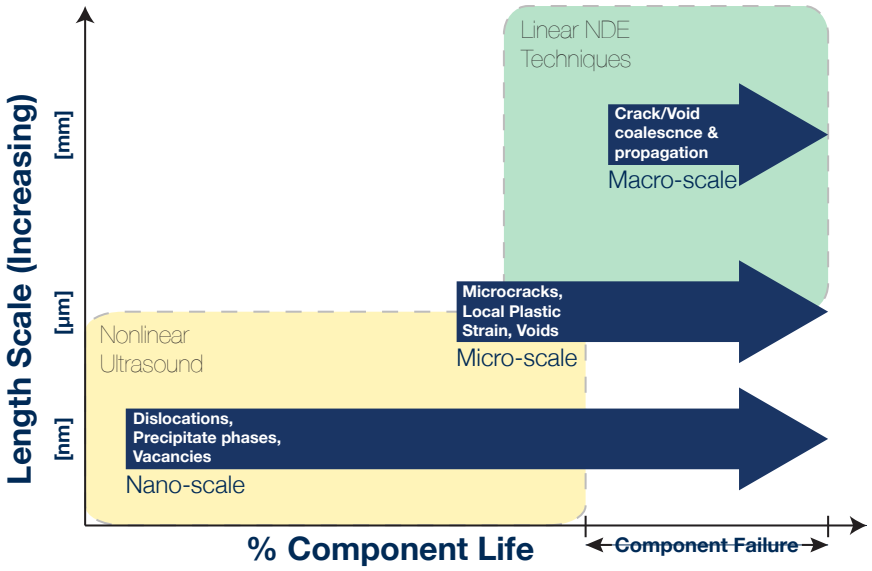

Figure 2.1: Regions of effectiveness of linear and nonlinear ultrasonic methods and the types of deformations and damage to which each are sensitive and length scales at which those mechanisms occur.

2.2 Second Harmonic Generation

Second Harmonic Generation (SHG) is a technique in NLU that exploits the distortion of a monotonic acoustic pulse as it propagates through a material with a nonlinear stress-strain relationship. As the single frequency acoustic wave moves through the material, it distorts according to the amount of nonlinearity present, physically transferring energy from the fundamental frequency component to waves at harmonics of that frequency. The amount of energy transferred from the fundamental to higher harmonics diminishes rapidly with each escalating harmonic number, but generally the second harmonic component (twice the input frequency) is detectable with sensitive equipment. Because this shunting of energy from the fundamental to the second harmonic wave continuously occurs as the wave propagates, the apparent effect is the ”generation” of the second harmonic wave with propagation distance. The rate at which this energy is transferred, and thus the amplitude of the second harmonic at a given point, is quantified through the nonlinearity parameter, β, which is related to microstructural features of the material under test. These features can

include the crystalline structure of the material as well as defects due to such features as dislocations or precipitates, which alter the local atomic strain fields at the microstructure level. Because these features are precursors to macroscopic damage, knowledge of the material nonlinearity parameter provides estimates of material state and thus holds particular significance to the NDE community. The derivation of this nonlinearity parameter is covered in the next section.

2.2.1 Derivation of the Nonlinearity Parameter for Propagating Longitudinal Waves

A longitudinal wave passing through an isotropic material of density ρ undergoes motion determined by the wave equation in one dimension:

$$\rho \frac{\partial^2 u}{\partial t^2} = \frac{\partial \sigma_{xx}}{\partial x} \tag{2.1}$$

where u is the particle displacement, σ_{xx} is the normal stress in the x direction, x is the distance along the propagation axis of the wave in the material, and t is the time variable. If we consider the material as having a quadratic nonlinear stress-strain relationship given by:

$$\sigma_{xx} = E\left(\frac{\partial u}{\partial x}\right) + \frac{1}{2}F\left(\frac{\partial u}{\partial x}\right)^2 + \dots \tag{2.2}$$

where E is the second order elastic constant (SOEC), F is a function of the third-order elastic constants (TOECs), and $\frac{\partial u}{\partial x}$ is the uniaxial strain in the material. Plugging 2.2 into 2.1, we derive the nonlinear wave equation for uniaxial longitudinal wave propagation:

$$\frac{\partial^2 u}{\partial t^2} = c\left[1 - \beta \frac{\partial u}{\partial x}\right]\frac{\partial^2 u}{\partial x^2} \tag{2.3}$$

where β is the material nonlinearity parameter an depends on the SOEC and TOECs of the material. This relationship in an unaltered material is governed by the equation:

$$\beta = -\frac{F}{E} = -\left(\frac{3C_{11} + C_{111}}{\sigma_1 + C_{11}}\right) \tag{2.4}$$

where C_{11} and C_{111} are the second- and third-order Brugger elastic constants. These constants are the material properties changing with material state and damage at the microstructural level, and it is this relationship that allows for measurement of β to be used as a damage indicator in NDE.

The time harmonic solution to Eq. 2.3, assuming a plane wave propagating through the material of monotonic frequency ω and a wave amplitude of A_0, is of the following form:

$$u_{out} = A_1 \sin(kx - \omega t) + A_2 \sin(2kx - 2\omega t) + \dots \tag{2.5}$$

where k is the wavenumber, and A_1 and A_2 are the fundamental and second harmonic wave amplitudes contained in the propagating wave. The second harmonic amplitude A_2, in the absence of any effects such as attenuation and diffraction, can be expressed by the following equation:

$$A_2 = \frac{\beta A_1^2 x k^2}{8} \tag{2.6}$$

This equation has a few key features that are worth examining. A_2 is shown to have a linear dependance on three important quantities for NLU measurements: A_1^2, β, and x. In order to isolate the effect of any one of these quantities on the second harmonic amplitude, the other two must be fixed or known as a function of position, which has major experimental implications and will be discussed at great length in later sections. By rearranging Eq. 2.6, we can express β in terms of the measurable fundamental and harmonic

wave amplitudes of the propagating waveform and basic acoustic quantities:

$$\beta = \frac{8A_2}{A_1^2 x k^2} \tag{2.7}$$

This expression for β is convenient for a variety of reasons; first and foremost it provides a blueprint by which to design an experiment from which we can determine the material nonlinearity. As was mentioned previously, the only experimental factors needed to determine the material nonlinearity are the second harmonic and fundamental wave amplitudes of the received signal, the wave number at the given fundamental frequency in the material under test, and the distance over which the wave propagates. Furthermore, it is apparent that β is proportional to the ratio of A_2 to A_1^2, which means that it can be related to the slope of a line drawn between points if those two quantities form the axes of a plot. Testing the relative changes across many samples can be simply performed by tracking the changes in the slope of A_2/A_1^2, using the unaltered base state of the material as a reference from which a relative β can be calculated. Finally, if the system, including electronic equipment and transducers, is calibrated correctly, absolute measures of β can be obtained directly from calculation of Eq. 2.7 in the absence of diffraction and attenuation effects. These effects cannot be ignored, however, especially where long propagation distances are concerned due to the effects they will have on measurement results[14, 31, 38]. Furthermore, attenuation and diffraction affect the fundamental and second harmonic waves differently, which will be discussed in a later section in more depth[31, 39, 40].

2.2.2 Derivation of the Nonlinearity Parameter for Propagating Rayleigh Waves

The formulation of the nonlinearity parameter for propagating Rayleigh waves must take into account the fact that a Rayleigh wave contains both longitudinal and shear wave components, accounting for particle motion in two directions simultaneously. If we consider the xy plane as the surface of the sample and the z direction to be facing positive into the bulk of the material, we can describe the x and z direction particle velocities in the

following set of equations[41, 42]:

$$v_x(x,y,0,t) = (\xi_t + \eta) \sum_{n=-\infty}^{\infty} v_n(x,y) e^{in(k_0 x - \omega_0 t)} \tag{2.8}$$

$$v_z(x,y,0,t) = (1 + \xi_l \eta) \sum_{n=-\infty}^{\infty} v_n(x,y) e^{in(k_0 x - \omega_0 t)} \tag{2.9}$$

where n denotes the harmonic number, $\xi_t = (1-\xi^2)^{1/2}$, $\xi_l = (1 - \xi^2 c_t^2/c_l^2)^{1/2}$, $\eta = -2(1-\xi^2)^{1/2}/(2-\xi^2)$, $\xi = c_R/c_t$, c_l is the longitudinal phase velocity, c_t is the shear phase velocity, and c_R is the Rayleigh phase velocity.

Shull et al. showed that by utilizing a quasilinear assumption, the fundamental and second harmonic equations of motion can be expressed as follows[41]:

$$\left(\frac{\partial}{\partial x} + \frac{1}{2ik_0} \frac{\partial^2}{\partial y^2} + \alpha_1 \right) v_1 = 0 \tag{2.10}$$

$$\left(\frac{\partial}{\partial x} + \frac{1}{4ik_0} \frac{\partial^2}{\partial y^2} + \alpha_2 \right) v_2 = \frac{\beta_{11} k_0}{2c_R} v_1^2 \tag{2.11}$$

where α_1 and v_1 represent the attenuation and out-of-plane particle velocity at the fundamental frequency and α_2 and v_2 represent the attenuation and velocity at the second harmonic frequency.

The nonlinearity parameter in the Rayleigh wave formulation, β_{11}, is different that the longitudinal wave nonlinearity parameter, β, and can be determined analytically by the equation:

$$\beta_{11} = \frac{4\mu R_{11}}{\zeta \rho c_R^2} \tag{2.12}$$

where μ is the shear modulus, ρ is the material density, $\zeta = \xi_t + \xi_t^{-1} + \eta^2(\xi_l + \xi_l^{-1}) + 4\eta$, and R_{11} is based on the TOECs of the material and is defined by Shull et al. elsewhere[43]. While Eq. 2.12 hints at the possibility of calculating β_{11} directly, it is practically very

difficult to determine the material TOECs from experimentation[44]. It is therefore more expedient and accurate to measure the nonlinearity parameter from SHG methods[1, 19, 20, 45].

If the source that generates the Rayleigh wave is a line source, and if that source has a Gaussian amplitude distribution and constant phase across the source profile, then the solutions to eqs. 2.10 and 2.11 have analytical solutions that may be found by following a Green's function integral approach. These solutions are given by the following set of equations[41]:

$$v_1(x,y) = \frac{v_0 e^{-\alpha_1 x}}{\sqrt{1+ix/x_0}} \exp\left(\frac{-(y/a_1)^2}{1+ix/x_0}\right) \tag{2.13}$$

$$\begin{aligned} v_2(x,y) =& \frac{i\sqrt{\pi}\beta_{11} v_{0,1}^2 k_0^2 a_1^2}{4c_{\mathrm{R}}\sqrt{i(\alpha_2-2\alpha_1)(x_0+ix)}} \times \\ & \exp\left(-\alpha_2 x - \frac{2(y/a_1)^2}{1+ix/x_0} + i(\alpha_2-2\alpha_1)x_0\right) \\ & \times \{\mathrm{erf}[\sqrt{i(\alpha_2-2\alpha_1)(x_0+ix)}] - \mathrm{erf}[\sqrt{i(\alpha_2-2\alpha_1)x_0}]\} \end{aligned} \tag{2.14}$$

where $x_0 = k_0 a_1^2/2$, which is the Rayleigh distance, signifying propagation distance that marks the transition from near field to far field effects.

From eqs. (2.13) and (2.14), it would appear to be a simple process to solve for β_{11} by measuring v_2 and filling in the values of the other variables. However, the source term $v_{0,1}$ an the attenuation coefficients are difficult to measure directly because of the physical limitations of the experimental setup. For this reason, it is simpler to fit these equations to experimentally determined values of v_1 and v_2 and extract the relevant values of these parameters through the use of nonlinear least squares optimization techniques[20, 45]. If the measured values of the surface velocities are absolute, then the extracted parameters will also be absolute parameters, including the Rayleigh nonlinearity parameter, β_{11}.

2.2.3 Contributions of Microstructure to the Nonlinearity Parameter

The ultimate goal of NLU is to connect the measured acoustic nonlinearity parameter to changes in material microstructure due to damage or other modifications. The basis of this endeavor is understanding the fundamental nonlinear acoustic properties of materials. It has also been shown that all real metallic materials have some degree of nonlinearity inherent in the material due to lattice anharmonicity in the crystalline structure[10]. The physical mechanism by which material nonlinearity develops can be explained largely in terms of dislocations, such as in the work of Hikata et al.[13] where a model connects dislocations to nonlinearity in aluminum samples and in Cantrell and Yost[46], where a model is presented that demonstrates the role of dislocation dipoles in the harmonic generation of ultrasonic signals. Extensions of the dislocation pinning based models were performed by Cash and Cai[47] to account for orientation dependencies of the dislocation line energy, which were confirmed with dislocation dynamics simulations. It also revealed that the relationship between β and stress is nonlinear and that measurements of the nonlinearity parameter could in fact have negative values, determined by measuring phase in addition to harmonic amplitude[48]. Zhang et al.[49, 50] extended the Hikata et al. model to account for different types of dislocations, and compared their predictions to previous measurements performed on stainless steel[18].

Two other major contributors to material acoustic nonlinearity are precipitates that form in the material and microcracks that develop on the surface and in the bulk of the material. While it is believed that precipitates themselves do not have a substantial impact on the measured β in a material[51], their interactions with dislocations do affect measured values of the acoustic nonlinearity[21, 51, 52]. Nonlinear contributions from microcracks stem from the nonlinear stress-strain relationship caused from contacting asperities at the crack interface[29, 53–56], and their effects have been demonstrated in fatigue induced damage[53] and models have been proposed for microcrack distributions and their effects on measured parameters[57].

2.3 Ultrasonic Receivers

Fundamental to NLU measurements is the choice of the acoustic receiver technology for the given application. It is important to understand the impacts of the varying types of transducers on what measurements may be performed and what information the data will provide, and thus a review of the dominant receiver technologies is provided here to clarify the pros and cons of each technology and to justify the choice of receivers used in this work. There are four dominant technologies in the current state-of-the-art: contact piezoelectric transducers, air-coupled piezoelectric transducers, laser interferometers, and electromagnetic acoustic transducers (EMATs).

2.3.1 Contact Piezoelectric Transducers

Contact receivers measure the mechanical particle displacement in a material through mechanical coupling with the material surface, and the most common type of contact transducer in ultrasonic experiments is the piezoelectric transducer. This is because of the ease with which the electrical signal outputs can be digitized and manipulated in addition to the robustness of the device itself. The two most common types of piezoelectric transduction technologies used in contact transducers are piezoceramic materials such as PZT and single crystal piezoelectric materials such as LiNbO3 (lithium niobate), quartz, etc. While PZT demonstrates very high piezoelectric coupling constants relative to single crystal materials, it tends to behave nonlinearly to high power acoustic inputs. This can have a particularly large impact on the generation side of NLU experiments by adding nonlinear signals to those created through second harmonic generation by the material under test[58]. Further, the quality factor Q, defined as the center frequency divided by the 3dB bandwidth, of single crystal piezoelectric materials tends to be an order of magnitude higher than comparable PZT technologies, which impacts the situations in which these materials will be useful[23]. For situations in which the transducer has little time to reach steady state (such

as in tone burst excitation with a small number of cycles), a high Q transducer can suffer from excessive ringing and will not yield useful data. However, a high Q transducer can be useful as a sort of analog filter with which to boost the signal to noise ratio (SNR) of the low amplitude second harmonic signals. These trade-offs and more must be balanced when choosing or designing appropriate piezoelectric receivers for SHG experiments[22, 59].

An example of a contact piezoelectric SHG experimental setup is show in Fig. 2.2 and highlights the general usage of piezoelectric contact transduction in NLU. The generating contact transducer is fed a signal from a combination of a function generator and high-power amplifier, which broadcasts the acoustic signal through the material to a receiving transducer, the output of which is measured by an oscilloscope and digitized. It is not uncommon for low Q, high bandwidth PZT receiving transducers to further pass through an analog filter at each frequency of interest in order to independently amplify the signal components to improve SNR. This is important because of dynamic range issues arising from the large disparity between the fundamental and second harmonic signal amplitudes[35].

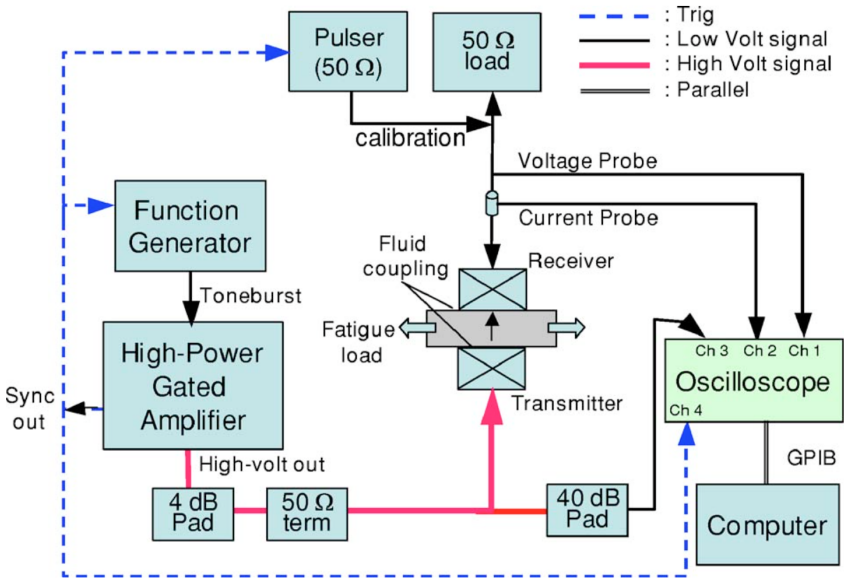

Figure 2.2: Typical contact piezoelectric transducer setup for SHG measurements in longitudinal propagation[2].

2.3.1.1 Relative Measurements

Contact piezoelectric transducers can immediately be used for relative β measurements in SHG because there is no need for calibration of the transducer itself, and their use in literature is well documented and widespread across many materials and types of damage[2, 9, 18, 21]. One of the most important problems when dealing with contact transducers is managing the contact conditions between the surface of the material and the sample[27, 28], which can have a profound impact on the transmitted and measured acoustic waves. This means that to make repeatable and accurate measurements the contact interface must be carefully controlled and accounted for. A common solution is to use a coupling fluid such as a low viscosity oil, the purpose of which is prevent air gaps between the transducer and the material at the interface[28]. This drastically increases the repeatability of SHG measurements and provides more reliable results by reducing partial reflections at this interface because of large acoustic impedance mismatches.

The advantages of making relative measurements are numerous. First, the exact values of acoustic wave amplitudes are not important to the result because every measurement is normalized by a base state measurement, which means that calibration of the transducers is not required. The nonlinearity of the generating electronics and other experimental components can be neglected over the course of the entire measurement because their effects will remain constant throughout the entire run of experiments (or care can be taken to make this approximately true). This, too, should be eliminated through the normalization process or some form of signal processing such as a mean reduction. These factors greatly reduce the experimental complexity of SHG measurements, and for situations in which base state information is available, mimic the cases of real-world usefulness of SHG techniques. However, for situations where this information is not available, which is far more common in the modern engineering world, a relative measurement has a greatly reduced efficacy. For these cases, an absolute measurement is required, and this requires a much more careful consideration of the transducers themselves.

2.3.1.2 *Absolute Measurements*

Absolute measurements of β are obtained by measuring the absolute displacement of the fundamental and second harmonic waves, and in order to do this with piezoelectric transducers, the relationship between the displacement and the voltage as a function of frequency must be known completely. One of the most widespread methods for determining this transfer function is the self-reciprocity calibration, originally adapted to SHG experimental setups by Dace et al.[24, 25], in which the transfer function $H(\omega)$ is determined by measuring the input and output current and voltages of the receiving transducer, from which the relationship between measured amplitude and output current is defined as:

$$A(\omega) = H(\omega)I'(\omega) \tag{2.15}$$

where $A(\omega)$ is the displacement amplitude of the acoustic wave and $I'(\omega)$ is the output current measured during the SHG experiment. $H(\omega)$ is defined as:

$$H(\omega) = \sqrt{\frac{\frac{I_{in}(\omega)V_{out}(\omega)}{I_{out}(\omega)} + V_{in}(\omega)}{w\omega^2\rho c_L \alpha I_{out}(\omega)}} \tag{2.16}$$

where I_{in}, I_{out}, V_{in}, and V_{out} are the input and output current and voltage signals, ρ is the material density, c_L is the longitudinal wave speed, and a is the transducer radius. The difficulty with this calibration is that it is contact condition dependent, so once the calibration is performed, the receiving transducer cannot be disturbed until the measurement is complete, and each time a measurement on a new sample must be performed, a new calibration is required. This adds a great deal of time to a set of measurement if multiple samples must be tested. Taking these factors into consideration, this calibration technique has been used to measure absolute β in a variety of settings[2, 31, 38, 60]. Ultimately, the desire to make measurements that completely disregard the contact conditions between receiver and sample would of great benefit to the NLU toolkit, increasing the practical viability of SHG

experiments in the field for in-situ measurements by reducing the variability of contact conditions on measured data. In order to accomplish this greater goal, non-contact receiving technologies are critical and will be discussed in the next section.

2.3.2 Non-contact Receiving Technologies

Given the difficulty in calibrating contact transducers and the problematic impact of the contact conditions on NLU experiments, non-contact receivers are particularly attractive as a method of measuring ultrasonic wave amplitudes because they eschew contact altogether. There are four major non-contact receiving technologies currently used to measure material nonlinearity: laser interferometers, capacitive transducers, EMATs, and air-coupled piezoelectric transducers.

2.3.2.1 Laser Interferometry

Laser interferometry is a powerful tool for measuring wave amplitudes in SHG experiments and has been used very effectively to characterize metallic specimens[20, 31, 35, 45, 61]. The most common type of interferometer used in SHG experiments is a heterodyne Michelson interferometer because of their insensitivity to low amplitude building vibrations and thermal drift[35], and because of the ease with which they can be calibrated[31, 35]. Perhaps the most powerful characteristic of the laser interferometer is that the output, once calibrated a single time, can be used almost immediately to give absolute displacement or velocity amplitudes. Because laser interferometers are essentially point detectors (compared to commercial ultrasonic transducers) and because they have a very wide, flat bandwidth, under many conditions they are the ideal measurement tool for SHG experiments.

There are many cases, however, in which laser interferometry is non-ideal, and many of these cases are actually quite common. Laser interferometers provide the best SNR on highly polished samples because the measurement resolution is directly related to the

intensity of the received light reflected from the material surface[35, 37], however many samples either cannot be polished to this level or doing so would be impractical. Additionally, heterodyne laser interferometers at some stage must demodulate the acoustic signal from a high frequency carrier signal, and this demodulation is a highly nonlinear process by design. If not careful, the nonlinear contribution to the output signal from the laser demodulation stage can overcome the measured material nonlinearity, making the SHG measurement impossible[35]. This can be overcome with careful analog demodulation, purely digital demodulation, and high laser power to boost signal SNR[37].

The main problem with laser interferometers is not related to their effectiveness in SHG measurements, but rather the size, impracticality of transportation, and high cost of systems suited for SHG measurements. Ultimately, the desired solution would be a device that offered non-contact, absolute measurements like a heterodyne interferometer, but with a smaller form factor, reduced cost, and more robustness for use in field measurements.

2.3.2.2 EMATs and Capacitive Receivers

Electro-magnetic acoustic transducers (EMATs) are a promising technology that induces or receives ultrasonic wave information from a sample via the interaction between two magnetic fields. A typical EMAT construction is shown in Fig. 2.3. The magnet creates a static or low frequency magnetic field that interacts with the acoustic waves on the surface, creating a current in the receiving EMAT coil which can be directly related to the acoustic disturbance amplitude[33, 34, 62, 63]. There are many positive characteristics to EMATs, such as being impervious to contact conditions including surface coatings, oxidation, and roughness, flexibility in mode selectivity based on coil design, and sensitivity to SH modes which is very difficult for other receiver types. However, they are at the moment limited to lower ultrasonic frequencies (below 3 MHz) and they are extremely sensitive to small fabrication variations[63]. Additionally, they are limited to use on metallic or magnetic materials, care must be taken with using them on samples that can magnetize and the sam-

ples may require degaussing[34], and they have low transduction efficiency which requires either a high power current generator or more sophisticated signal processing techniques to isolate signal from noise and make their use in SHG difficult[33]. Once these limitations can be addressed by manufacturers, EMATs will be attractive as an option for SHG measurements, but at this moment they are not ideal for this application.

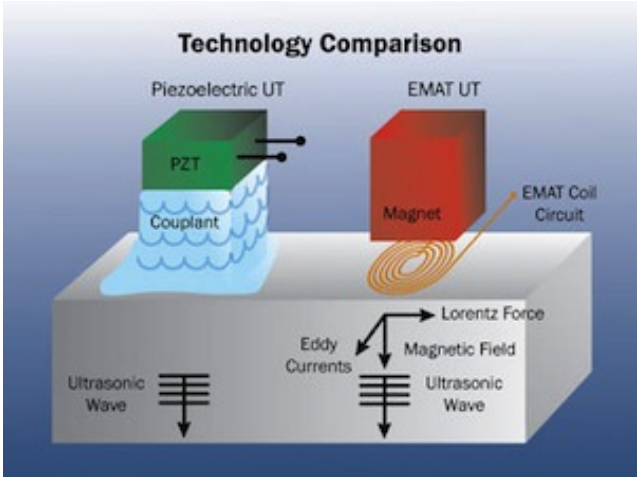

Figure 2.3: Design schematic of EMAT transducer and a comparison to the experimental configuration used in contact piezoelectric excitation[64].

Capacitive receivers are well researched in literature and have been used to great effect in SHG measurements with very high quality results[4, 30, 32, 65, 66], even providing the first absolute measurements of β by Gauster and Breazeale[17]. In this scheme, a capacitor is created between one electrode bonded to a sample and another suspended mechanically above it with a carefully controlled air gap between them. By adjusting the bias voltage in this capacitor, small changes in surface displacement shorten or lengthen the air gap, causing a voltage output proportional to this harmonic displacement according to the formula:

$$A(\omega) = \frac{dV_0(\omega)}{2V_b} \tag{2.17}$$

where $V_0(\omega)$ is the output voltage of the receiver, d is the air gap spacing, and V_b is the bias voltage between the capacitive plates. After a careful calibration process using a highly controlled input signal and comparing these to their corresponding outputs after heavy

filtering[31], this method provides measurement sensitivity up to 0.1 femtometers, which is more than enough to resolve nonlinear signals produced by SHG experiments. While this level of resolution and the generally high accuracy of these measurements make capacitive receivers attractive, there are a few very significant downsides to this process. The first is that one of the electrodes must be bound to the sample surface, so an extremely high degree of flatness is required on the sample over the receiver area which can be challenging to achieve even in laboratory settings on some specimens. The other major drawback is that the air gap must be held to a few microns, which is very difficult to fabricate accurately and repeatably. For these reasons, a highly accurate, easy to use solution becomes much more attractive, even at the expense of sensitivity as long as SHG wave detection is still possible.

2.3.2.3 Air-Coupled Piezoelectric Transducers

Air-coupled piezoelectric transduction is still a relatively new technology as far as NDE use is concerned for detection of nonlinear signal components in SHG experiments[20, 67], although they have been used in linear NDE for quite some time[68–70]. They combine the high sensitivity and ease of use of piezoelectric transducers with the non-contact benefits of laser ultrasonics, EMATs, and capacitive transducers. They operate on the principle that part of the ultrasonic energy that reaches the surface of the specimen either in bulk wave or surface wave propagation will leak into the air surrounding the specimen, which is then received by the transducer which is specially matched to air as a propagation medium making very small displacement detection possible. The relationship of this leaked wave to the wave at the surface can be easily determined by examining the displacement continuity at the interface[71], and in the case of surface waves, the angle at which the wave will propagate upon leaking into the surrounding air is directly found by application of Snells law:

$$\Theta_R = \sin^{-1}\left(\frac{c_{air}}{c_R}\right) \tag{2.18}$$

where Θ_R is the angle at which the wave will propagate after leaking from the surface of the material (known as the Rayleigh angle) and c_{air} and c_R are the longitudinal wave speed of sound in air and the Rayleigh wave speed in the sample respectively. With air-coupled transducer experiments, accurate alignment of the transducer to the sample surface is perhaps the most important experimental concern and has drastic consequences on the measured data[19, 20, 72], so great care must be taken to make sure this alignment is as accurate as possible. A sample schematic of an air-coupled receiver Rayleigh wave experimental setup is provided in Fig. 2.4

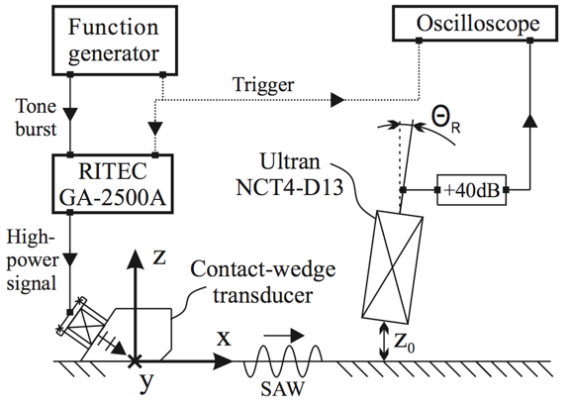

Figure 2.4: Rayleigh wave SHG experimental schematic for air-coupled piezoelectric receiver detection of leaked pressure waves from Rayleigh wave propagation along the sample surface.

The major drawback to using air-coupled piezoelectric detection is the same as the drawback to using any piezoelectric detection - the device itself must be calibrated carefully in order to detect absolute wave displacements of the leaked pressure waves. This is even trickier than in the case of contact transducers because self-reciprocity calibrations are very difficult to apply to these transducers due to their poor performance as ultrasonic sources and the highly attenuating nature of air as an ultrasonic medium. In order to calibrate these receivers, we will need to propose a new framework by which to calibrate these air-coupled transducers so that they may be used in absolute NLU experiments.

2.4 Summary

This chapter reviewed the concepts, theoretical derivations, and current literature on second harmonic generation techniques for conducting nonlinear ultrasonic experiments. The main points of this chapter are listed as follows:

- The main concept behind SHG is that a second harmonic wave is generated as an incoming wave interacts with the microstructural features and defects in a material, and it can be characterized by the nonlinearity parameter, β, as defined by its use in the nonlinear wave equation.

- The form of β differs greatly depending on the wave propagation mode through the material under test. In this work, the two major propagation modes examined are longitudinal wave propagation through the bulk of the material and Rayleigh wave propagation along its surface.

- There are various microstructural contributions to β, such as dislocations and precipitates. These are the underlying mechanisms through which β changes as a material is exposed to fatigue, thermal aging, cold work, and creep.

- Central to the measurement of β is the choice of receiver in the SHG experiment, which is determined by whether the measurement must be absolute or relative, how the material is prepared, and the desired sensitivity of the measuring technology among a great deal of factors. Primarily of interest is the use of air-coupled piezoelectric transducers because of their relative low-cost and robustness as compared to other absolute receiving technologies. However, as with all piezoelectric transducers, they must be calibrated for absolute measurement purposes, which is especially challenging given their operating principle.

CHAPTER 3

SOURCE CHARACTERIZATION AND SYSTEM NONLINEARITY

3.1 Motivation

The first step in calculating the acoustic nonlinearity parameter with SHG experiments is generating an acoustic wave through a sample. As was stated in the previous chapter this acoustic wave would ideally be a rectangular-gated tone burst with only the fundamental frequency component present over the duration of the pulse. In order to use the modeling assumptions presented in the background section and in the propagation modeling, we must confirm that the acoustic source acts accordingly. To measure the acoustic sources, a laser interferometer was used to determine the magnitude and phase characteristics to identify the linearity and the amplitude distribution across the transducer profile. For the case of bulk wave measurements, a piezoelectric contact transducer source is in direct contact with the sample, so laser scans were conducted of the transducer face to see if uniform, piston-like behavior is occurring, allowing for the use of the uniform piston assumption in modeling. The Rayleigh wave case is more complicated, but an effective source location and amplitude profile would ideally be Gaussian in nature, greatly simplifying the surface wave field modeling across the specimen surface. The linearity of the sources must also be examined and the effects of the source nonlinearity should be decoupled from the data, resulting in the separation of the source nonlinearity amplitude A_2^T from the material nonlinearity amplitude A_2^M, an essential step in the calculation of the absolute nonlinearity parameter. As part of the exploration into source linearity, we must also examine various source types, including the use of the spectrally pure sources in the form of Lithium Niobate (LiNbO3) discs, ideally enabling more accurate detection of nonlinearities originating from material properties by minimizing A_2^T.

3.2 Ultrasonic source characterization

Ultrasonic transducers for excitation of acoustic waves through materials are fairly limited in available technologies because of the fairly strenuous requirements. Ultrasonic sources in SHG experiments must be spectrally pure so that they do not negatively affect the generated second harmonic signal as the acoustic wave propagates, and they must also be able to generate enough acoustic power to create relative high amplitude waves in a material. The latter requirement is particularly important because the amplitude of the generated second harmonic wave is related to the amplitude of the fundamental propagating wave squared, A_1^2, as is shown in Eq. (2.6). Not many transducer technologies can withstand the high voltages required to generate these large amplitude disturbances, and fewer still can do so while producing a spectrally pure signal. Piezoelectric contact transducers of the type shown in Fig. 3.1 are therefore the common choice for these experiments, and in the following sections we will analyze the configurations and characteristics of the source transducers in both longitudinal wave and Rayleigh wave NLU testing environments.

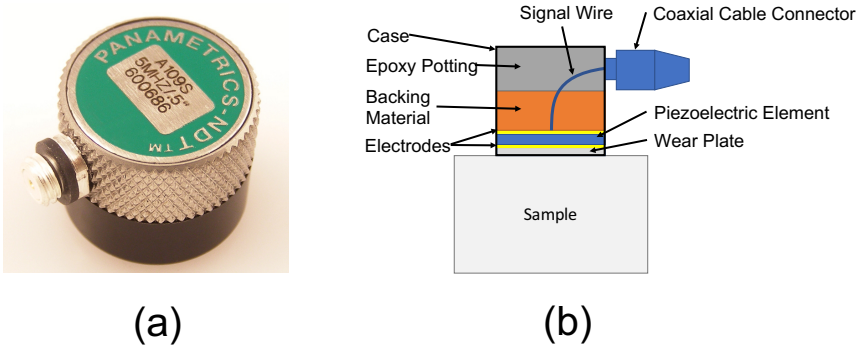

Figure 3.1: (a) Typical contact piezoelectric transducer used to generate acoustic waves in SHG experiments. (b) Cut away section of a contact transducer in contact with a sample. Note the material layers between the actual transducer element and the sample, as well as the backing material behind the transducer element, both of which change the transducer frequency response and insertion losses.

3.2.1 Source amplitude profiles

3.2.1.1 Longitudinal wave configuration

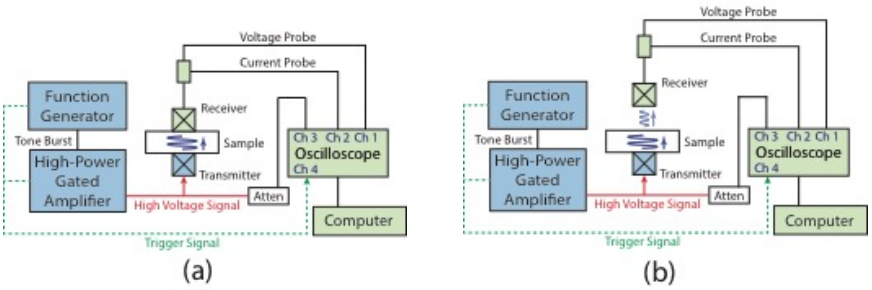

Figure 3.2: Typical longitudinal wave NLU setup for SHG measurements. The generating transducer, labeled as "transmitter" in (a) and (b), is a contact piezoelectric transducer that is held via a clamp to the sample. (a) shows a configuration in which the receiver is a contact transducer as well, while (b) shows an air-coupled receiver setup, which is similar except for the choice of receiver technology.

Longitudinal wave SHG experiments are generally conducted in the configuration shown in Fig. 3.2 (a) and (b), in which a contact piezoelectric transducer is clamped to the surface of a sample. The source is excited by a large pulse, which generates a pressure wave at the interface of the transducer and the sample through the piezoelectric effect. At this point it is important to identify exactly what the ideal acoustic source for SHG experiments would be. In the case of piezoelectric excitation, this reduces to two major requirements: the source should act as a uniform piston for the purpose of modeling (explored in the next chapter), and the source should be spectrally pure so that the generated second harmonic in the material is not affected by any nonlinearities from the transducer itself. We will now address the first of these requirements.

The ideal source for these experiments will have as close to piston operation as possible because of the ease with which a uniform piston source can be modeled and those models compared to solved, closed-form analytic solutions to on-axis pressure values as a function of propagation distance. In reality, the amplitude profile across the surface of the transducer can have any shape and still be modeled as we will see in the next chapter, but it will

be helpful if there is at least radial symmetry for the amplitude profile in order to simplify the modeling equations. In order to test for this symmetry and to determine the amplitude profile of the commercial piezoelectric source at the frequencies of interest, we use the experimental setup shown in Fig. 3.3. Ideally, we would be able to measure the transducer response in the blocked state, where it is held in contact with another material under similar conditions to those in which SHG testing is performed, but this is practically difficult and so we instead measure the open-air response directly with a laser interferometer with the understanding that the frequency response of the transducer under these boundary conditions will not be the same as in an actual SHG test. However, we can be fairly certain that the mode-shapes will remain the same, and thus this test will provide us the information we seek on the source profile.

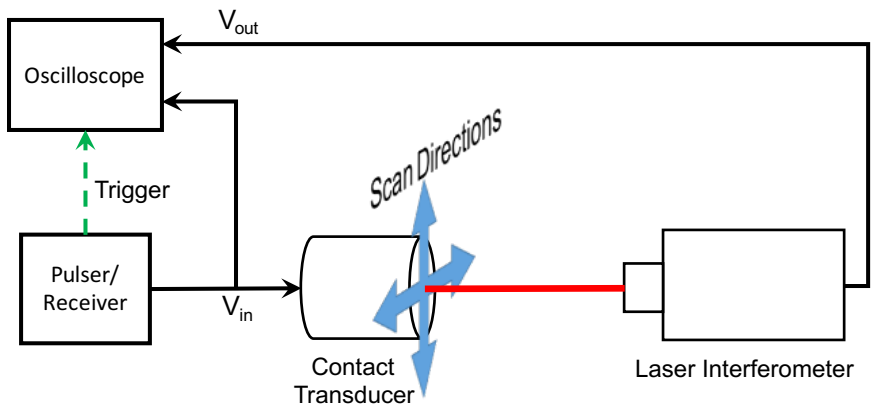

Figure 3.3: Experimental setup for source characterization using a laser interferometer to scan the transducer surface.

In these experiments, a Panametrics 5052PR generating a 400 Vpp broadband pulse with 50 Ohm damping electrically excites the contact transducer. The 50 Ohm damping setting is used to make sure that the transducer and the electrical source are impedance matched to reduce insertion losses. The laser interferometer is a Polytec OFV 534 laser head coupled with an OFV-5000 modular controller with a DD-300 high bandwidth digital decoder installed for high frequency measurement up to 20 MHz with a detection sensitivity of 50 nm/V. The contact transducer in this test and in all the longitudinal wave experiments

following in this work is a Panametric V109 contact transducer with a nominal frequency of 5 MHz. The result of the scanning measurement, which outputs a two dimensional map of surface amplitudes, is shown in Fig. 3.4. These results show that from a frequency range of 1 to 5 MHz, the behavior of the transducer is piston-like, with the noisiness of the higher frequency results more a function of the SNR of the measurement because of the surface quality of the transducer than actual amplitude differences in the surface displacement.

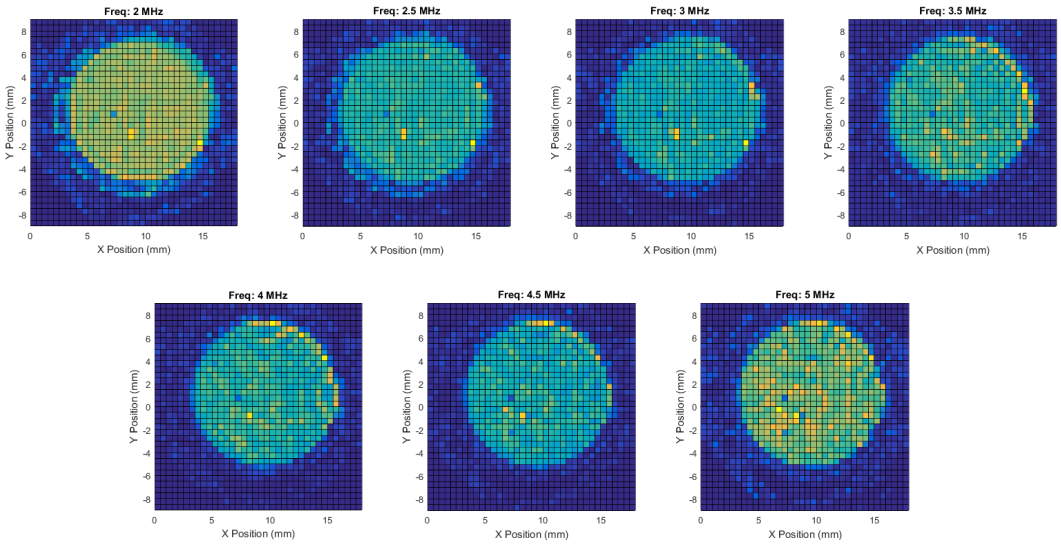

Figure 3.4: Results of laser interferometer scan of 5 MHz Panametrics V109 generating transducer. The transducer has a piston-like response from 1 MHz to 5 MHz.

The fact that the transducer amplitude profile is uniformly piston-like across all the frequencies of interest in this work is highly beneficial for the modeling outcomes discussed in sec. 4.2. This result, however, is not desirable in all measurement cases, such as in the Rayleigh wave measurement case when other source profiles would be ideal. Therefore we will now examine the transducer/wedge combination and the profile of the effective source for these experiments.

3.2.1.2 Rayleigh wave configuration

Whereas the source for the longitudinal wave SHG measurements is in direct contact with the sample, this is not the case for Rayleigh wave measurements because the acoustic wave

from the source must contact the sample at a specific angle required to generate Rayleigh waves for the same reason as discussed in sec. 2.3.2.3[1]. Therefore, the contact transducer is first clamped to a wedge that aligns the acoustic axis of the transducer to the sample surface at this Rayleigh generation angle, and this entire transducer/wedge assembly is then clamped to the sample as shown in Fig. 3.5. Direct measurement of the source in this configuration with a laser interferometer is very difficult, and the passage of the acoustic wave through the wedge would create an extremely complicated modeling picture ill-suited for optimization routines which are essential to the extraction of the nonlinearity parameter in this configuration. Therefore, instead of directly measuring the transducer surface, we will instead characterize the trailing edge of contact interface between the wedge and sample, which is the "effective source" described in Fig. 3.5.

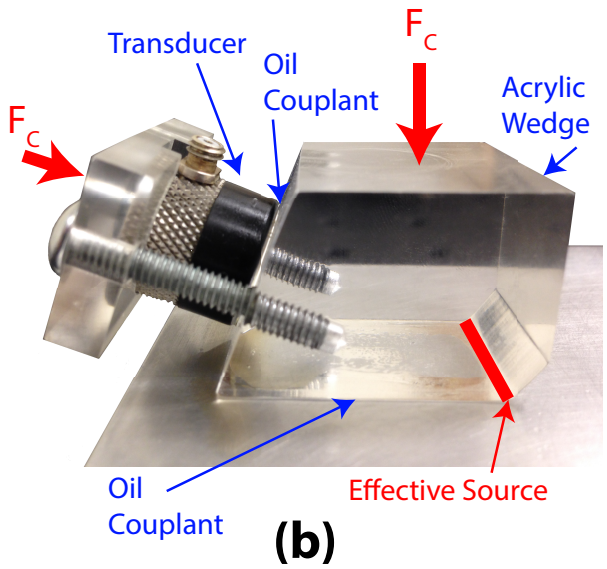

Figure 3.5: Picture of the transducer/wedge assembly used to generate Rayleigh waves on a sample surface. The transducer is held in place with a clamping force provided by the screws, and the entire assembly is held in place by another clamping force. The effective source is the leading edge where the wedge meets the sample.

In order to measure the effective source, which in this case is a line source, we will use a similar methodology to that used in characterizing the longitudinal wave configuration. Using a laser interferometer, we will scan the effective line source and determine the

amplitude profile from FFTs of the recorded signals. The test setup to capture this data is shown below in Fig. 3.6 and consists of the same generating electronics and generating transducer as in sec. 3.2.1.1. In this measurement, the laser is scanned along the y axis at the propagation distance $x = 0$ as opposed to a two dimensional scan as for the longitudinal configurations. Additionally, instead of exciting the source with a 900 Ypp pulse, we instead use a 900 Vpp, 20 cycle tone burst at 2 MHz. The results of this scan are shown in Fig. 3.7, with (a) showing the response at the fundamental frequency of 2 MHz and (b) showing the response at the second harmonic frequency of 4 MHz.

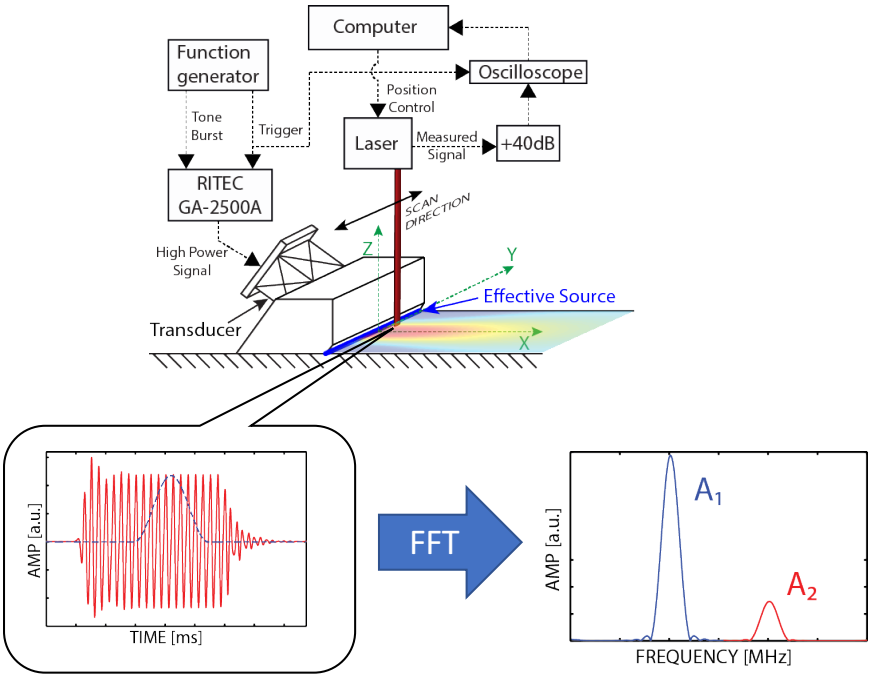

Figure 3.6: Experimental setup used to measure the transducer/wedge effective source profile with a laser interferometer. Each measurement point is signal processed in MATLAB by using a time domain Hanning window and taking an FFT to extract the fundamental and second harmonic signal content.

There are two immediate observations that can be made regarding the source profiles shown in the figure. The first is that both the fundamental and second harmonic responses shown in (a) and (b) respectively are Gaussian profiles, shown by the fit curves. The Guassian fit of the fundamental has an R-squared value of .904, and the second harmonic fit has an R-squared value of .703, both demonstrating excellent fit to the models. The Guassian

beam width is also smaller for the second harmonic than the fundamental, with the fundamental half-width value a equal to 6.53 mm whereas the second harmonic a is equal to 2.69 mm. This makes sense according to standard acoustic theory[73]. This is in stark contrast to the result of the longitudinal setup, in which the modeling source is best described as a piston. Gaussian profiles are actually easier to model, both in terms of source values and the Rayleigh wave propagation emanating from a Gaussian source[41]. The second observation has to do with the existence of a nonlinear term in the source as shown by the existence of a measured signal at 4 MHz shown in Fig. 3.7(b), which will be discussed in the next section.

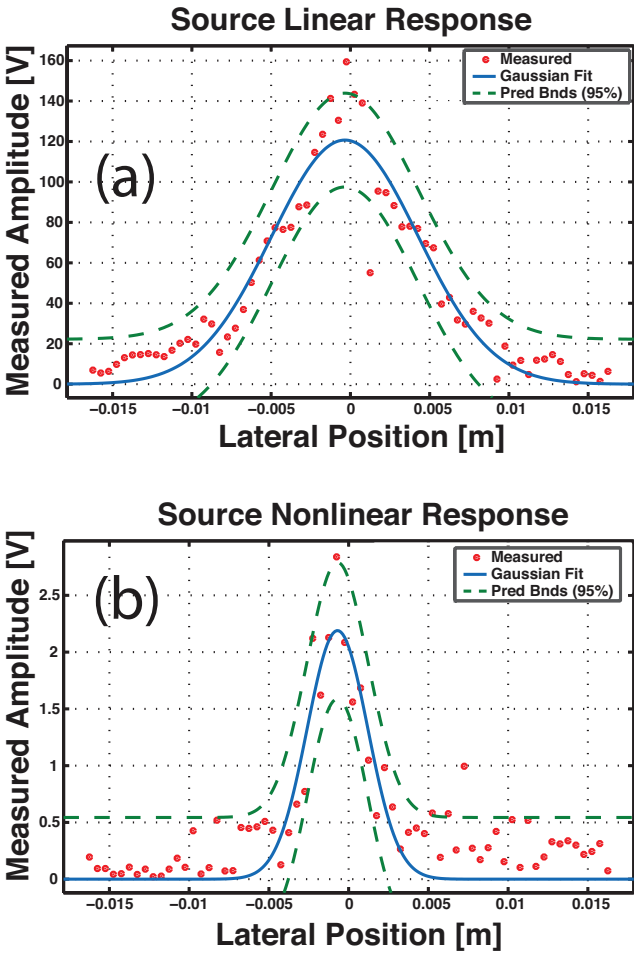

Figure 3.7: Results of Rayleigh source profile measurements for the (a) fundamental and (b) second harmonic source response. The measurement error bounds for a 95 percent confidence interval (green dotted line) of the Gaussian fit (blue line) of the measured data (red dots) is shown for both frequencies.

3.2.2 Source linearity

The result shown in Fig. 3.7(b) demonstrates there is a second harmonic component to the propagating waves from the source independent of the material generated second harmonic derived in ch. 2. The second harmonic component is 40 dB less than the fundamental, which puts it at a similar amplitude scale to the generated second harmonic nonlinearity in metallic materials [41]. The effect of this acoustic nonlinearity from the source on SHG measurements with Rayleigh waves can be seen in Fig. 3.8. The total measured signal including the acoustic nonlinearity from the source A_2^T is represented by the blue dotted line A_2. This A_2 is a combination of the source nonlinearity and the generated material nonlinearity A_2^M. If we are going to measure the absolute nonlinearity parameter β using the measured data, we need to remove the contribution from A_2^T to the measurement, and this process is discussed in detail in the next chapter.

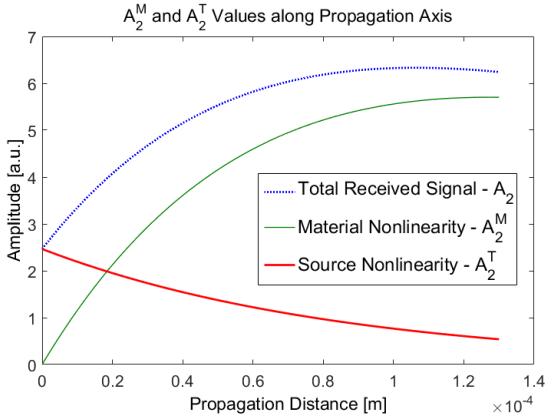

Figure 3.8: Effect of source nonlinearity on the total measured second harmonic signal.

The presence of the acoustic nonlinearity from the source can arise from many factors, a few of which are predominant in SHG measurements. These are contact acoustic nonlinearities caused by contact interfaces, the coupling conditions of the transducer to the sample or wedge, and the piezoelectric material used in the construction of the transducer.

3.2.2.1 Contact acoustic nonlinearities and coupling conditions

Contact acoustic nonlinearity (CAN) occurs at interfaces because of the nonlinear stress-strain relationship at the interface gap due to contact mechanics. This can be attributed in some cases to the idea of asperities compressing and interacting according to a contact law such as Hertzian contact mechanics[74, 75], or to interfacial cracks opening and closing, referred to as "clapping", causing a highly nonlinear stress-strain curve and hysteretic behavior[29, 76, 77]. These contact conditions can cause harmonic and subharmonic generation on a scale that is significant to SHG measurements, and thus it is important to reduce the number of instances in which these conditions can occur. In SHG measurements, the rule of thumb is to reduce the number of contact interfaces to a minimum for the best possible measurements, and where unavoidable, attempt to make the interface as repeatable, consistent, and linear as possible.

An explanation of a contact interface and the effect is has on harmonic generation can be seen in Fig. 3.9. The case of full closure shown in (a) has the obvious effect of perfect transmission according to linear theory such that $\sigma(\epsilon) = E\epsilon$, which is a statement of Hooke's law. The case of a fully open crack or disengaged interface shown in (b) has the similarly obvious stress-strain relationship of zero stress and thus zero wave propagation (discounting leaked pressure waves bridging the interfaces as negligible) such that $\sigma(\epsilon) = 0$. The case of partial closure shown in (c) is a much more difficult model to describe because of the complexity of the interface. Various factors will affect the stress-strain relationship, such as the roughness of the interfaces, the shape of the asperities, the material properties of the interfacial materials, the frequency of the excitation, etc. Summarizing these effects is accomplished by simply considering the stress-strain relationship as a nonlinear function $C(\epsilon)$ such that $\sigma(\epsilon) = C(\epsilon)\epsilon$. Biwa et al notes that the pressure dependence of the stress-strain relationship observes power law behavior with the exponent value depending on the roughness, size, and uniformity of the asperities[74], while Solodov et al have evaluate the case of diode like behavior of crack oscillation between open and closed states and have

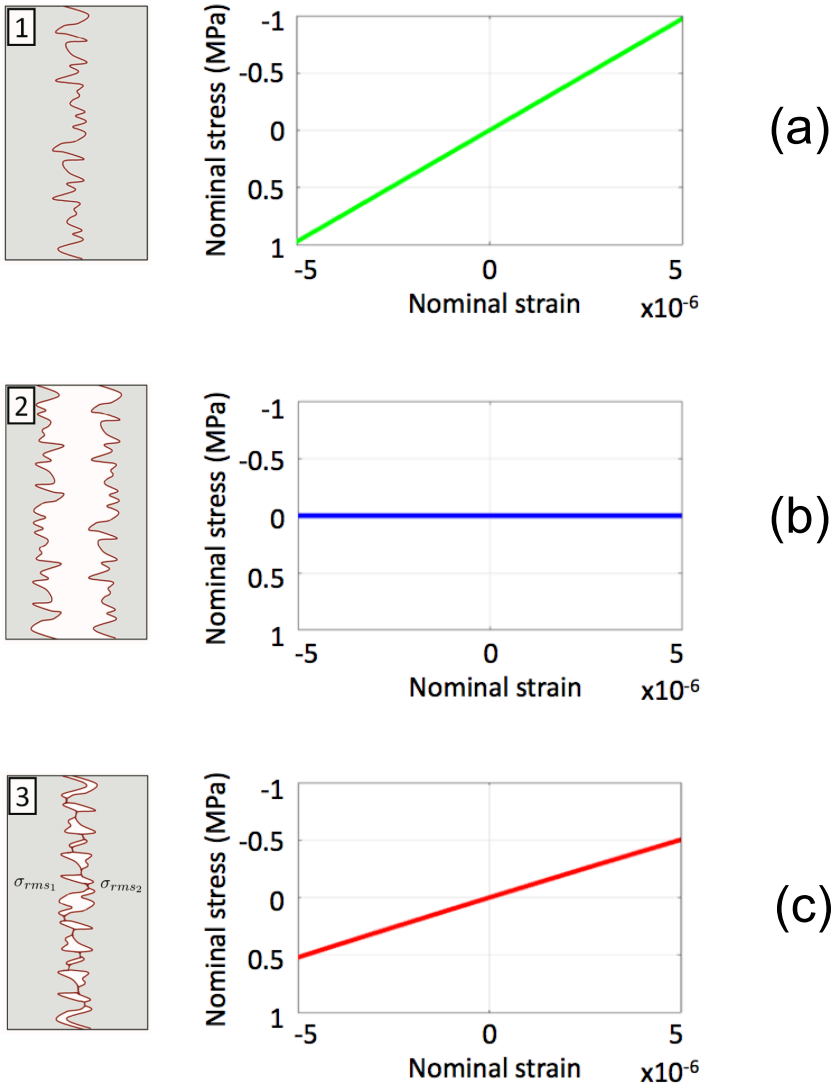

Figure 3.9: Schematic of CAN and the various states of closure of a crack or interface on the stress-strain relationship at that interface. (a) shows a crack or interface that is fully closed, (b) shows a crack or interface that is fully open, and (c) shows a crack or interface with partial closure[76]

observed subharmonic content from acoustic transmission across the interface[29]. This effect has even been taken advantage of to decoupled amplitude modulated signals into useful lower and higher frequency components for low frequency excitation from high frequency carrier waves[75]. All of these circumstances, however, prove to be bad for SHG experiments because, particularly on the generation side of the experiment, any spurious signal content can lead to a distortion of the obtained absolute acoustic nonlinearity parameter.

It has been noted by many sources that the best way to avoid CAN effects at interfaces is to keep the contact pressure as low as possible while still maintaining experimentally viable alignment and physical robustness of the setup[78]. This can have an effect as much as 16% in measured values of β between firm a high clamping force and no clamping force[78]. Additionally, it's common to introduce a coupling fluid to reduce CAN effects by providing an alternative acoustic path through the coupling fluid for a large portion of the acoustic energy to travel through[2, 27, 28, 78] in addition to reducing the reflection of acoustic energy at the interface by the high acoustic impedance mismatch between the metallic sample and air, which results in a very high reflection coefficient[73]. This latter effect reduces the overall fundamental amplitude wave transmission through the interface, thus reducing the generated second harmonic, which would therefore reduce the impact of material nonlinearity on the total nonlinearity measured by the receiving transducer in proportion to that caused by other effects.

3.2.2.2 Piezoelectric transducer material choices

Another consideration for reducing the nonlinearity of the source is choice of piezoelectric material and transducer construction. The two dominant materials used for piezoelectric excitation in SHG experiments are lead zirconate titanate (PZT) and lithium niobate (LiNbO3), and each has advantages and disadvantages. PZT transducers have very high electromechanical coupling coefficients (which is a metric that helps determine the conversion efficiency of the piezoelectric effect in a material) and are very easy to manufacture because they are solidified from powders, allowing for a wide variety of shapes, thicknesses, and polarities in production[23, 79]. LiNbO3 is a single crystal material and thus harder to manufacture into a variety of useful shapes and thicknesses, but it also has a high electromechanical coupling coefficient on the order of PZT, and has a much higher quality factor which means it has a sharper bandwidth, which is good for single frequency excitation such as is required in SHG measurements[23, 79]. Both of these transducer ma-

terials are well suited for large amplitude, high power excitation conditions such as those SHG demands, but when it comes to producing a pure toneburst excitation, there are other considerations to make involving the nonlinearity of the transducer material and the time domain characteristics of the transducer response.

Comparing the nonlinearity of the transducer materials will give an idea of how much of the fundamental signal is converted into the initial second harmonic excitation seen in Fig. 3.7. In general, LiNbO3 crystals have a smaller nonlinearity than PZT materials, with a summary of the nonlinearity parameters and sources listed in tab. 3.1. The nonlinearity parameter is calculated according to Eq. (3.1) below:

$$\beta = -\left(3 + \frac{C_{111}}{C_{11}}\right) \tag{3.1}$$

where C_{111} is the longitudinal third-order elastic constant and C_{11} is the second order longitudinal elastic constant. While the difference is not too large at first glance, it can lead to a significant impact in measured nonlinearity at the receiver, and thus is important to consider. This will become apparent when the results of the nonlinearity parameter measurements are discussed in a later chapter.

Table 3.1: Summary of nonlinearity parameters β of PZT and LiNbO3 crystals from literature.

Material	$C_{111} \times 10^{11}[N/m]$	$C_{11} \times 10^{11}[N/m]$	β
LiNbO3	21.2[80]	[81]	13.55
	5.12[81]	2	5.56
	16.1[82]		11.05
PZT-4 (K1)	29.7[83]	1.32[83]	25.5
	18.5[58]	1.65[58]	14.21
PZT-5H (S1)	24.1[83]	1.34[83]	20.98
	12.1[58]	1.64[58]	10.37

Another consideration in using LiNbO3 or PZT is the quality factor of the material. A high Q material like LiNbO3 is advantageous because it introduces a sharp notch-filter like transfer function into the frequency response of the generating system which will lead

to high spectral purity of the generated acoustic wave through the sample. However, this comes at the cost of a large ringing effect from the rectangularly gated signal coming from the amplifier due to the sudden steps at the beginning and end of the excitation. This manifests as a longer number of cycles to reach a steady state amplitude at the beginning of the tone burst and a longer tail at the end of the tone burst. When a thick sample is measured, this has less importance because a larger number of cycles can be used. This is the case in Rayleigh wave measurements when 20 plus cycles can be used in the tone burst before reflections interfere with the generated waveform. However, thin samples such as those typically used in longitudinal wave experiments can often support a much smaller number of cycles between 5 and 10. For these smaller cycle counts, great care must be used to make sure the ringing of the LiNbO3 piezoelectric element doesn't cause time-domain effects to corrupt the measured signal. That being said, in the experimental setups used in this work, the Lithium Niobate disc transients were not a significant factor in either experiment type because the number of cycles was 10 or greater in both cases, giving ample time for the transducer to reach steady state.

3.2.3 System nonlinearity and windowing distortion

One of the facts of experimental setups in which amplification of a signal is involved is that amplifiers are, in general, nonlinear devices. This can introduce a nonlinearity to the generating transducer, and if the transducer is broadband and doesn't filter this nonlinearity out due to it's own transfer function, then this amplifier nonlinearity could have an effect on the measured total nonlinearity from the receiver output. An example of the level of amplifier nonlinearity present over the full range of amplifier output value from zero (no output) to ten (maximum output) is shown in Fig. 3.10. Ideally, the left curve showing the increase of A_1 with output level should be linear, and indeed many amplifier designed for second harmonic generation experiments are quite linear in this sense. However, nearly all amplifier exhibit a response at A_2 as well, which can be mitigated by using a transducer element

that naturally filters out this component[5], or by introducing a filter element such as an LR impedance matching circuit into the generation path[84]. In this work, the compensation for transducer nonlinearity also compensates for the system nonlinearity introduced by the amplifier, and this problem is neatly sidestepped.

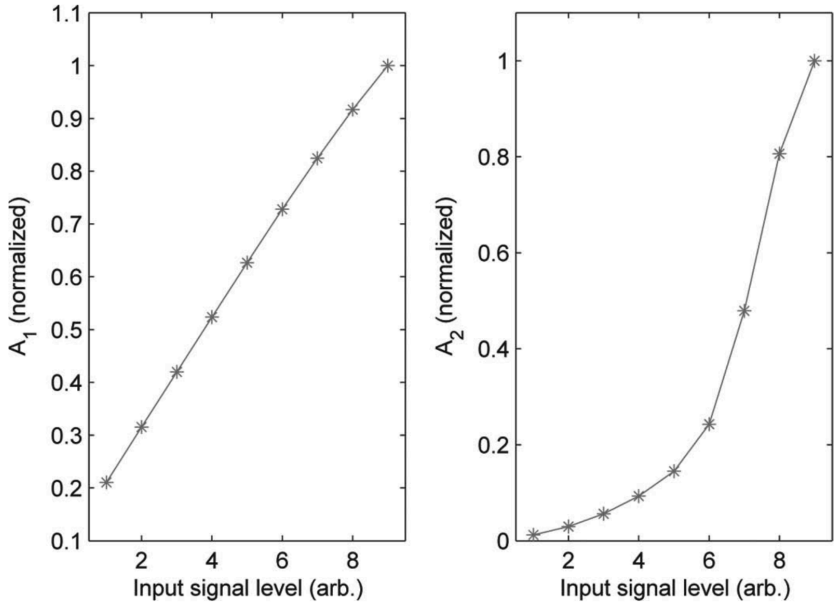

Figure 3.10: Example of the nonlinearity present in an amplifier with increasing gain. The fundamental response remains linear [left], where the second harmonic generated due to nonlinearity in the amplifier changes with input level [right][5].

Another important source of nonlinearity that must be accounted for is on the signal processing of the received waveform. Generally, a received waveform is windowed in the time domain and then analyzed via FFT to find the frequency components of the signal. As with all FFTs, the assumption is that the signal is time harmonic and infinite, which is clearly not true because the input signal itself is rectangularly gated. As a result, even using no window in the signal analysis of the output will in effect be rectangularly windowing the input to the FFT. This is not an ideal window to chose for signal analysis because the spectral leakage of the resulting FFT of the input signal can and will affect the measured harmonic, which will absorb some of this leakage and lead to an overestimation of β. Therefore we want to window the signal with a window that has as small of sidelobe am-

plitude as possible[2, 5]. A comparison of windowing functions via their FFTs is shown in Fig. 3.11, in which various windows (solid line) are compared to a hanning window baseline (dotted line)[5]. There are two factors to consider when comparing windows. The first is sidelobe amplitude, and by far the best perfomance is the Hanning window (dotted line) in which the second harmonic of the main lobe at 3.6 MHz in this case (with the harmonic at 7.2 MHz) has the smallest lobe amplitude, with the Tukey 0.75 response a close second. However, dropoff is also a consideration, where the decrease in sidelobe amplitude must happen fast enough that the reduction in amplitude actually occurs at the correct frequency. In this case, Hanning is still the best choice, although this will not always be the case. However, from these results, it is clear that the Hanning window is the optimal choice for SHG experiments.

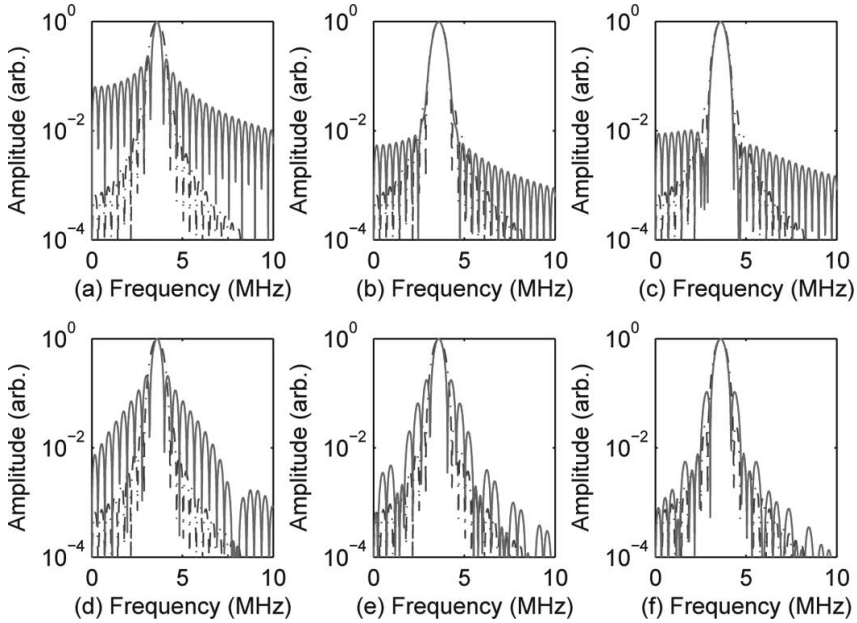

Figure 3.11: Signal processing window FFTs for comparison of sidelobe amplitude and dropoff. In order, the window types are (a) Rectangular, (b) Gaussian, (c) Hamming, (d) Tukey 0.25, (e) Tukey 0.5, and (f) Tukey 0.75. All window responses (solid line) are superimposed over the Hanning window response (dotted line) for comparison[5].

The consequence of windowing the signal is that the main lobe amplitude will under represent the energy at the fundamental frequency, and so amplitude correction is required

to report the correct fundamental and second harmonic wave amplitude values. Most modern FFT packages, such as that employed by MATLAB, can correct for this drop in amplitude, but it is important to note its possible contribution nonetheless.

3.2.3.1 Laser interferometry nonlinearity

One final note on sources of nonlinearity other than the harmonics generated in the material is the threshold value for which a laser interferometer can make nonlinear measurements. Because the laser interferometer used in this work is a heterodyne interferometer, it requires a stage in the analog or digital demodulation of the receiver signal from the acousto-optic element in order to extract the signal that contains the surface vibration amplitude[35]. Demodulation of a signal is performed in these cases by a mixer or some other nonlinear element, and while this nonlinearity is required for the signal demodulation, it also creates harmonic noise in the interferometer output. There is a fundamental threshold value of 35 dB from the Polytec literature for the amplitude reduction of the demodulation stage harmonic noise, but if the generated harmonic signal from the SHG physics does not create its own harmonic with an amplitude greater than this for whatever reason, it will be masked or completely altered by this mixer noise. As a result, there are certain SHG measurements which the Polytec system used in this work simply cannot make. An example of this is an SHG measurement made with the Polytec laser shown in Fig. 3.12. While the fundamental Rayleigh wave signals appear normal, the second harmonic signals in (c) and (d) do not show signs of harmonic generation and instead exactly mimic the characteristic of the fundamental signal with a reduced amplitude. This is because the demodulation noise of the Polytec is overshadowing the SHG signal, and for Rayleigh wave measurements this will almost always be the case unless the nonlinearity parameter β_{11} is sufficiently large to overcome this masking. This is an unfortunate instrumentation reality, and makes laser interferomtric verification of SHG measurements impossible with the current setup and materials.

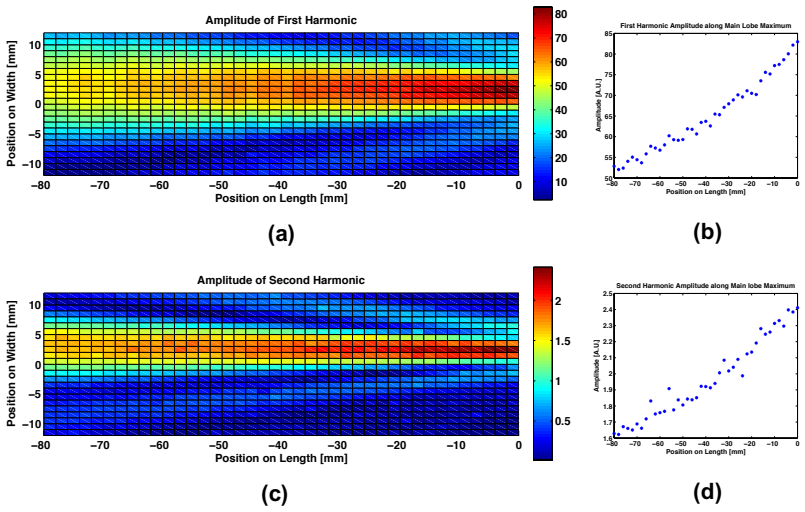

Figure 3.12: Two dimensional scans of Rayleigh wave propagation patern taken with Polytec laser interferometer used in this work. The source transducer is located to the right of the figures (a-d), and the Rayleigh wave propagates to the left. The fundamental (a and b) signals look as expected from the waveforms derived in ch. 2. However, the second harmonic (c and d) clearly doesn't increase with propagation distance, while we know this phenomenon to occur. In fact, its behavior clearly mimics the behavior of the fundamental, albeit at a reduced amplitude. The presence of this signal is masked from the demodulation noise in the Polytec interferometer.

3.3 Summary

This chapter discussed the characterization of the ultrasonic source and displayed the modeling assumptions that can be made about these sources for use in propagation modeling in later portions of this work. Additionally, a rigorous accounting of the sources of nonlinearity present from the generating transducer, electronics, signal processing, and other equipment was provided as well as the ramifications for SHG measurements. The major points of this chapter are listed as follows:

- The ultrasonic sources used in this work are contact piezoelectric transducers, and they behave differently depending on the experimental configuration chosen for longitudinal or Rayleigh wave excitation. In longitudinal experiments, the source acts as a uniform piston, but in Rayleigh wave experiments the source acts a a Gaussian line source.

- The choice of source type and material has a drastic impact on the performance of the source, particularly in analyzing the nonlinearity present in the measurement from contributions directly linked to the generating transducer. PZT and LiNbO3, two common transducer materials, show very different properties that make them suitable for different kinds of measurements. Generally, LiNbO3 is a more linear material, but PZT commercial transducers are more broadband, and thus have a more ideal time domain response characteristic.

- There are a lot of source of nonlinearity from the generation side of SH experiments, including contact acoustic nonlinearity at material interfaces, transducer nonlinearity, coupling conditions, electronics nonlinearity, and signal conditioning of the input and output signals.

- The Polytec laser interferometer used in this work is a powerful tool for making absolute measurements as a reference for air-coupled measurement results, but there are certain measurements that it simply cannot make because of demodulation noise from the internal electronics of the controller. As a result, Rayleigh wave measurements with the Polytec are more or less impossible with this setup, while longitudinal wave measurements have a high enough amplitude that they are not affected by this source of error.

CHAPTER 4

PROPAGATION MODELING AND NONLINEAR OPTIMIZATION

4.1 Motivation

Objective 2 of this research concerns the accurate prediction of the wavefield of a propagating acoustic wave through a sample under test. An accurate acoustic field model can be used in conjunction with an optimization algorithm to determine the values of the model parameters that best fit measured data, and from this fitting procedure we can determine the acoustic nonlinearity. This is because the models that are developed in this section are physics-based models that take into account the acoustic theory and material parameters relevant to the problem (as opposed to a polynomial series for instance where little physical interpretation exists while the fit to the measured data may be quite good).

In contrast to setups in which contact transducer are used for both transmitter and receiver, there is an air gap between the air-coupled receiver and the sample surface. This air-gap has a profound impact on how NLU measurements are performed on a specimen when trying to determine the absolute β of a material. In the case where β^* is sufficient for experimental purposes, an air-coupled transducer may be treated in the same way as for contact transducer measurements because the propagation across the air gap will be the same for all states of the material, and thus the results can be compared to a base state in the same methodology as used in most NLU applications[19]. Contact transducers used in absolute measurements merely need to be calibrated through a self-reciprocity framework in order to yield useful results[24, 25], although as was discussed before, interfaces cause significant experimental challenges that must be overcome and make the method unwieldy for field application[2]. Air-coupled transducers don't have these limitations, but modeling the propagation through the air gap becomes crucial because the air-coupled transducer,

even when calibrated, does not give direct information about the sample surface. Therefore, we need to use models to predict what the calibrated measurements from the air-coupled receiver can tell us about the conditions on the surface of the specimen. This is where the need for modeling and optimization arises, and we must spend a great amount of time and care to properly account for the primary components of a propagation model suitable for SHG measurements: harmonic generation, attenuation, and diffraction corrections.

In this section, we will first examine the appropriate modeling frameworks to predict the behavior of longitudinal wave and Rayleigh waves as they pass through or along a sample. Then we will examine how to use these models to extract material parameters, among them the nonlinearity parameter β.

4.2 Longitudinal wave propagation modeling

A typical longitudinal wave setup with an air-coupled receiver is shown in Fig. 4.1. In this configuration, there are three major modeling components that are accounted for in the propagation of an acoustic wave from a source (described in the previous section) to the surface of the receiver. The first is the propagation through the sample material, the second is the propagation across the interface between the sample and the air gap, referred to as ”leaking” of the acoustic wave, and the third is the propagation of the leaked acoustic wave through the air to the receiver surface. At each of these steps, both the effects on the fundamental and the second harmonic waves must be accounted for, which in many cases can prove to be analytically and computationally difficult.

If the acoustic source were infinite in size and radiating through a material with infinite lateral dimensions, the propagation modeling for the case of longitudinal wave propagation would be accounted for by the simple analysis provided in sec. 2.2.1. However, because the acoustic source, as discussed in the previous section, is finite and directive, the radiated ultrasonic beam experiences diffraction effects, and the materials through which the waves are propagating will lead to attenuation. Therefore the predicted linear increase in A_2

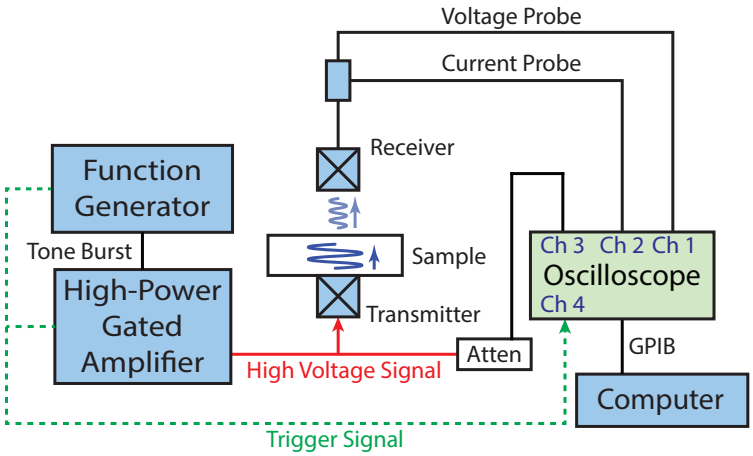

Figure 4.1: Typical longitudinal wave NLU setup for longitudinal SHG measurements. The generating transducer, labeled as "transmitter", is a contact piezoelectric transducer that is held via a clamp to the sample. The receiver is an air-coupled transducer with an air gap separation from the surface of the sample. The propagation field from source to receiver must include the wavefields through both the sample and this air gap in order to provide useful information from air-coupled measurements about the state of the sample surface.

arising from Eq. (2.6) and the constant value of A_1 with propagation distance will clearly not lead to correct modeling results that agree with physical data. The diffraction and attenuation effects arising from the transducers and the material properties will be discussed along with their implications for modeling in the following sections.

4.2.1 Field modeling versus correction factors

Before discussing the mechanics and derivations of the models themselves, it is important to discuss the paradigms that currently exist in predicting acoustic wave amplitude at the acoustic receiver. There are two useful methods by which wave amplitudes are calculated: field models that can be used to predict wave amplitude at any point in the sound field, including along the lateral x, y dimensions, and correction based methods in which all of the spatial effects causing diffraction are lumped into one parameter that is purely a function

of the propagation distance z over which the wave travels.

The linear sound field is well accounted for in either case, and exact solutions exist for the case where the source and the receiver are the same size[85, 86]. These exact solutions include the effects of diffraction, and can be easily modified to include attenuation effects, and offer the ability to either calculate the full acoustic field or to consider the average effects of plane wave propagation through a sample and reduce the solution to a function of propagation distance. For the linear field, there are numerous techniques and frameworks through which propagation can be modeled and they have been used to accurately measure the apparent ultrasonic wave speed and attenuation coefficient in a variety of materials[23, 85, 87].

The difficulty arises in accounting for the propagation of the generated second harmonic component as the linear, or fundamental, wave passes through the sample, and it is here that the modeling paradigm becomes important to consider. Approximate diffraction corrections to the second harmonic wave have been presented by a few sources[31, 88, 89], but all of them focus on distilling the diffraction effects down to a parameter that replaces the lateral amplitude changes to a function of the radii of the two circular transducer elements (source and receiver). This reduction of the parameter requires the two transducers to be aligned along their acoustic axes, a requirement which limits measurements of surfaces to simple points and can make validation of experimental data difficult because a two dimensional field of data is more reliable to optimize with than a single measurement point. Additionally, certain assumptions are immediately made about the acoustic sources and receivers in these cases, most egregious of them being they act like perfect planar pistons. While this is not a terrible assumption as has been shown in the previous chapter of this work, it severely limits the ability of these models for use in situations such as element array, focused transducers, or even modeling with slight irregularities to attempt to capture the complicated nature of actual transducer radiation patterns. Ideally we would be able to lift the planar transducer restriction, even if it useful, in order to have a more versatile

model.

This work will therefore explore models in which the full field is accounted for, in all propagation directions, with full flexibility in terms of source profiles and transducer alignments. The field models most effective in the type of optimization performed in this work are Rayleigh-Sommerfeld Integral (RSI) modeling and Multiple Gaussian Beam (MGB) modeling.

4.2.2 Field modeling frameworks

This section will explore the various models available for use in the optimization algorithm to extract the nonlinearity parameter from measured longitudinal wave propagation data.

4.2.2.1 Axial response from a circular piston

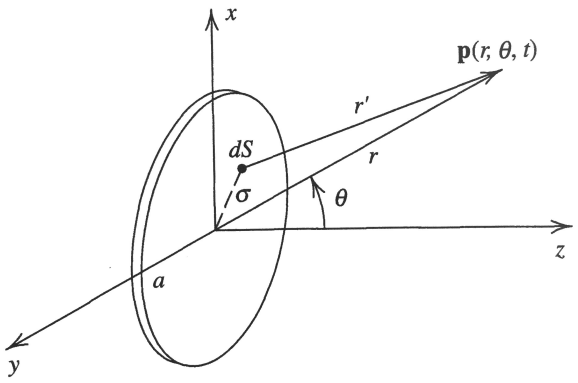

Figure 4.2: Geometry used in deriving the acoustic field of a baffled circular piston transducer[73].

Before discussing full field modeling, it will help to have an exact solution model as a reference. It is a well known result in many acoustic texts and references that the on axis pressure of a plane circular piston can be solved for by considering the transducer as a collection of simple baffled sources, as will be shown to be the case in RSI modeling as

well. The equation for the total complex pressure is:

$$\mathbf{p}(r,\theta,t) = j\rho_0 c\frac{U_0}{\lambda}\int_S \frac{1}{r'}e^{j(\omega t - kr')}\mathrm{d}S \tag{4.1}$$

where U_0 is the source velocity which is uniform over the piston, λ is the wavelength of the acoustic wave, ρ_0 is the density of the acoustic medium, c is the longitudinal wave speed in the medium, and the surface integral is taken over the region of the piston transducer surface. Solving this equation yields the following result:

$$\mathbf{p}(r,0,t) = \rho_0 c U_0 \left\{1 - \exp\left[-jk\left(\sqrt{r^2+a^2} - r\right)\right]\right\} e^{j(\omega t - kr)} \tag{4.2}$$

This complex pressure expression will give the exact solution for a piston transducer on the acoustic axis, and is a useful point of comparison for the models proposed later in this section. It's important to keep two things in mind when using this solution. The first is that it is only valid for axial values of the pressure, so it can only be used to verify the axial behavior of other modeling schemes. The second is that it only accounts for the linear portion of the acoustic wavefield, making it unsuitable in itself for calculations in SHG measurements and data processing. In order to account for higher harmonics and off-axis values of acoustic pressure, we must turn to more complicated modeling frameworks.

4.2.2.2 Rayleigh-Sommerfeld Integral (RSI) Methods

The RSI model stems from the concept that a radiating source of finite size can be represented by an infinite number of point sources of infinitesimal size and the sound fields of all these point sources can be added to create the field of the finite source. In the case of an ultrasonic transducer or a vibrating surface, we consider these point sources to be baffled. If we start with the Kirchhoff-Helmholtz integral formulated in the frequency domain[90]:

$$\hat{p}(\mathbf{x}) = \frac{1}{4\pi}\iint [\hat{p}(\mathbf{x}')\nabla' G_k(\mathbf{x}'|\mathbf{x}) - G_k(\mathbf{x}'|\mathbf{x})\nabla'\hat{p}(\mathbf{x}')]_{z_S=0}\cdot\mathbf{e}_z \mathrm{d}x'\mathrm{d}y' \tag{4.3}$$

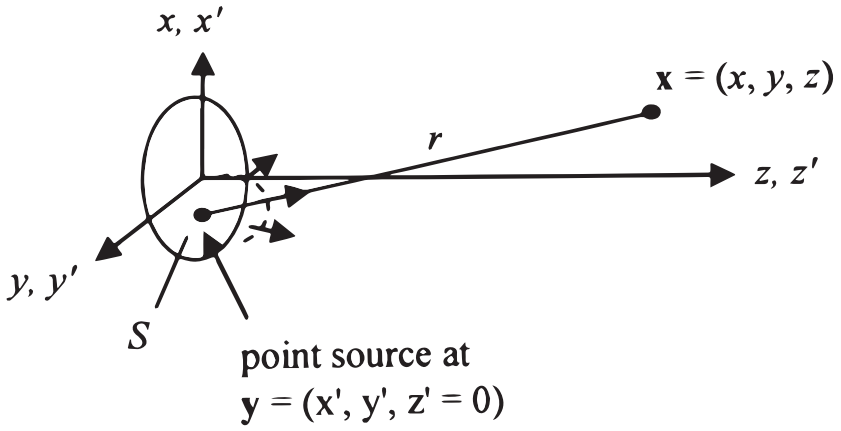

Figure 4.3: Transducer model as a superposition of an infinite number of radiating point sources. This diagram is the basis for the derivation of the RSI model[91].

where $\hat{p}$ is the pressure as a function of position **x**, the prime denotes source terms, and $G_k(x'|x)$ is the Green's function for a baffled piston point source which is derived via the method of images and is shown to be

$$G_k(\mathbf{x}'|\mathbf{x}) = \mathbf{R}_1^{-1} e^{ikR_1} + \mathbf{R}_2^{-1} e^{ikR_2} \tag{4.4}$$

where

$$\mathbf{R}_{1,2} = [(x' - x)^2 + (y' - y)^2 + (z' \mp z)^2]\frac{1}{2} \tag{4.5}$$

The Green's function of Eq. (4.4) satisfies the condition

$$\nabla' G_k(\mathbf{x}'|\mathbf{x}) \cdot \mathbf{e}_z|_{z'=0} = 0 \tag{4.6}$$

which means that the first term in Eq. (4.3) drops out of the equation. The second term simplifies as well because $G_k(\mathbf{x}'|\mathbf{x}) = 2\mathbf{R}^{-1}e^{ikR}$ and $\nabla'\hat{p}(\mathbf{x}')$ is $i\omega\rho\hat{v}(x', y')$ from Euler's equation of motion for an acoustic wave, so Eq. (4.3) simplifies to the following expression

for the pressure at a point in the field in the frequency domain:

$$\hat{p}(\mathbf{x}) = \frac{-i\omega\rho}{2\pi} \iint [\hat{v_n}(x', y')\mathbf{R}^{-1} e^{ikR} \mathrm{d}x' \mathrm{d}y' \tag{4.7}$$

The expression in Eq. (4.9) takes into account all the diffraction effects from the finite source in the near and far fields, but it does not take into account the attenuation. In order to account for attenuation, we consider that the pressure field decays as a function of the distance **R** from the source according to the relationship:

$$\hat{p}(\mathbf{x}) = \hat{p}_0 e^{-\alpha \mathbf{R}} \tag{4.8}$$

After converting Eq. (4.8) to velocity via the acoustic impedance ρc, we arrive at the following expression for the pressure field which includes the attenuation term:

$$\hat{p}(\mathbf{x}) = \frac{-i\omega\rho}{2\pi} \iint [\hat{v_n}(x', y')\mathbf{R}^{-1} e^{ik\mathbf{R}} e^{-\alpha \mathbf{R}} \mathrm{d}x' \mathrm{d}y' \tag{4.9}$$

This expression takes into account the discretization of the transmitting source, but if the goal of the model is to predict the pressure impinging on the surface of the air-coupled transducer, then the pressure field must be calculated at each specific location on the transducer surface from every point source. This means that to get the total pressure on the transducer surface, we must actually solve a quadruple integral with the following form:

$$\hat{p}(\mathbf{x}) = \frac{-i\omega\rho}{\pi} \iiiint [\hat{v_n}(x', y')\mathbf{R}^{-1} e^{ik\mathbf{R}} e^{-\alpha \mathbf{R}} \mathrm{d}x' \mathrm{d}y' \mathrm{d}x \mathrm{d}y \tag{4.10}$$

Eq. (4.10) is relatively straight forward to discretize and solve from a numerical computation perspective, but it is a quadruple integral which makes it extremely costly in terms of computing power. In MATLAB, this represents a quadruple nested 'for' loop, and the number of calculations required for domains on the order of actual transducer length scales

quickly grows to the hundreds of thousands per optimization iteration, and this can take hours, if not days, to solve. Given that this model is part of an iterative scheme for use in said optimization routines, this meas that the combined computing time of all iterations of the model takes many orders of magnitude more time than just the single run. The tradeoff however is that there are no sacrifices made between accuracy and computational time; the discretized form of Eq. (4.10) is equal exact solution along the acoustic axis for infinitesimally small elements and takes into account all relevant attenuation and diffraction effects with little to no assumptions or simplifications necessary. Essentially, the wave profile that it will predict for a piston transducer is that shown in Fig. 4.4, which differs from the exact on-axis solution in that edge wave behavior is modeled in addition to the direct wave component. It also accepts completely arbitrary sources with no restrictions on phase relationships or amplitude symmetry between the discretized source elements. Again, the cost of this flexibility and accuracy is computational efficiency.

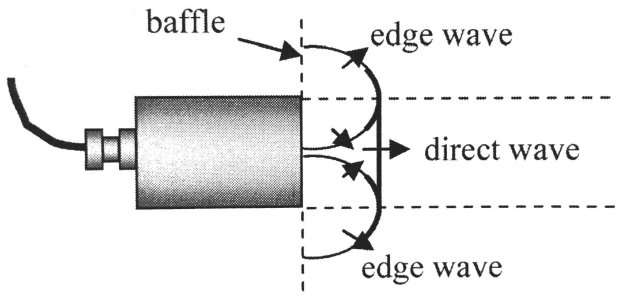

Figure 4.4: Direct and edge waves generated by an impulsively excited circular piston transducer predicted by the RSI integral, as contrasted to models that only predict the direct wave components[91].

The RSI model is a powerful model and there are many frameworks in place for solving it as quickly as possible, such as Fast Multipole Methods[92, 93]. However, there is a flaw in the RSI model as presented above; it does not cover the generation of second harmonic waves. This is because the wave equation that it solves is the linear wave equation. In order to solve the nonlinear wave equation with a Green's function approach similar to that used to derive the RSI model, we must examine the quasilinear solution to the Khokhlov-

Zabolotskaya-Kuznetsov (KZK) equation[94, 95].

4.2.2.3 Quasilinear solution to the KZK Equation

The Khokhlov-Zabolotskaya-Kuznetsov (KZK) equation was developed to model the attenuation and diffraction effects while accounting for a nonlinear stress-strain relationship which produces higher harmonic response. The KZK equation takes the form[94]:

$$\frac{\partial^2 p}{\partial z \partial \tau} = \frac{c}{2}\nabla_{\perp}^2 p + \frac{\delta}{2c^3}\frac{\partial^3 p}{\partial \tau^3} + \frac{\beta}{2\rho c^3}\frac{\partial^2 p^2}{\partial \tau^2} \tag{4.11}$$

where p is the acoustic pressure, τ is the retarded time $\tau = t - (z/c)$, δ is the sound diffusivity dependent on viscosity, thermal conductivity, and specific heat terms, $\nabla_{\perp}^2$ is the transverse Laplacian in x, y coordinates, and z is the beam propagation direction. The first term on the right-hand side of Eq. (4.11) models the diffraction of the propagating wave, the second term models the dissipation, and the third term models the generation of harmonic wave components due to material nonlinearity. Central to the formulation of Eq. (4.11) is the use of paraxial approximation, which necessarily breaks down in regions close to the source. However, the validity of this approximation has been tested in transducer beam field modeling and for regions half of a source diameter from the source itself, the approximation is acceptably close to the actual solution[96].

The quasilinear solution is assumed to have the form:

$$p = p_1 + p_2 = |p_1(r,z)|\exp(-i\omega\tau) + |p_2(r,z)|\exp(-2i\omega\tau) \tag{4.12}$$

where p_1 is the linear solution of Eq. (4.11) and p_2 is the correction term that accounts for the second harmonic frequency perturbations at 2ω. Substituting Eq. (4.12) into Eq. (4.11) yields the following equations of motion for the fundamental and second harmonic wave

fields:

$$\frac{\partial p_1}{\partial z} + \frac{i}{2k}\nabla_\perp^2 p_1 + \alpha_1 p_1 = 0 \tag{4.13}$$

$$\frac{\partial p_2}{\partial z} + \frac{i}{2k}\nabla_\perp^2 p_2 + \alpha_2 p_2 = \frac{\beta k}{2\rho c^2} p_1^2 \tag{4.14}$$

where α_n is the attenuation of an acoustic wave propagating linearly through a material at the n^{th} harmonic, with $n = 1$ corresponding to the fundamental wave form and $n = 2$ corresponding to the second harmonic waveform. This distinction is important because the actual attenuation of the second harmonic waveform is more complicated than the attenuation of a linearly propagating wave at a frequency 2ω which will be shown in the next section.

Solving eqs. (4.13) and (4.14) can be accomplished using the same Green's function approach as with the RSI model, except the Green's function takes a very different form as follows:

$$G_n(r, z|r', z') = \frac{ink}{2\pi(z - z')} J_0\left(\frac{nkrr'}{z - z'}\right) \exp\left[-\alpha_n(z - z') - \frac{ink\,(r^2 + r'^2)}{2(z - z')}\right] \tag{4.15}$$

where J_0 is the zeroth-order Bessel function and $n = 1, 2$ denotes the fundamental and second harmonic respectively.

The use of this Green's function can be then applied to the fundamental and second harmonic pressure field solutions so that the final results of these pressure fields are:

$$p_1(r, z) = 2\pi \int_0^{\inf} p_1(r', 0) G_1(r, z|r', 0) r' \mathrm{d}r' \tag{4.16}$$

$$p_2(r, z) = \frac{\pi\beta k}{\rho c^2} \int_0^z \int_0^{\inf} p_1^2(r', z') G_2(r, z|r', z') r' \mathrm{d}r' \mathrm{d}z' \tag{4.17}$$

In order to use these equations, the pressure or amplitude distribution of the source must be first obtained, which we have shown in the previous chapter of this work. After determining the source function that is most appropriate to match the experiment, it can be used to solve Eq. (4.16). This solution can then be used to solve the second harmonic pressure field equation given in Eq. (4.17), which depends on p_1^2

The pressure field model offered by eqs. (4.16) and (4.17) suffer from all the same advantages and limitations of the RSI model because in essence they are the same formulation. In the case of the second harmonic wave field, the computational cost is even higher than before. It is therefore important for the use of an optimization algorithm to find a model that can give comparably accurate answers to eqs. (4.16) and (4.17) while greatly increasing computational resource efficiency. The model that meets these requirements is the Multiple Gaussian Beam (MGB) equations.

4.2.2.4 Multiple Gaussian Beam (MGB) Methods

The MGB model was first developed for acoustic transducers by Wen and Breazeale[97] in order to predict the acoustic beam field from a uniform piston transducer by decomposing a source geometry into a linear combination of Gaussian functions. Because Gaussian source functions propagate as Gaussian functions through an acoustic media with a known, closed-form analytic solution, the beam field solutions can be solved quickly and accuractly in a numerical setting as contrasted to the RSI model, where the same equation must be solved for the large number of distretized elements in the domain. The key to the MGB model is to correctly decompose the source into its constiutent Gaussian components, which was originally solved for with a ten term series of Guassian coefficients according to the formula[97]:

$$\mathbf{V}_0(\xi) = \sum_{n=0}^{N} \mathbf{A}_n \exp(-\mathbf{B}_n \xi^2) \tag{4.18}$$

where $\mathbf{V}_0(\xi)$ is the velocity of the source as a function of the geometric variable ξ. and $\mathbf{A}_n$ and $\mathbf{B}_n$ are complex valued coefficients that determine the magnitude, witdh, and phase of the Gaussian profile. The ten term series was later revised to a fifteen term series[98] increased the accuracy of the solution to distances from the source as close as one half diameter of the piston from the plane of the source[96]. These fifteen terms are shown in tab. 4.1, and the accuracy of the combination of Gaussian terms given by the Eq. (4.18) from these coefficients is shown in Fig. 4.5.

Table 4.1: Gaussian coefficients for a piston source as calculated by Wen and Breazeale for use in Eq. (4.18)[98]

n	$\mathbf{A}_n$	$\mathbf{B}_n$
1	-2.9716 + i8.6187	4.1869 - i5.1560
2	-3.4811 + i0.9687	3.8398 - i10.8004
3	-1.3982 - i0.8128	3.4355 - i16.3582
4	0.0773 - i0.3303	2.4618 - i27.7134
5	2.8798 + i1.6109	5.4699 + i28.6319
6	0.1259 - i0.0957	1.9833 - i33.2885
7	-0.2641 - i0.6723	2.9335 - i22.0151
8	18.019 + i7.8291	6.3036 + i36.7772
9	0.0518 + i0.0182	1.3046 - i38.4650
10	-16.9438 - i9.9384	6.5889 + i37.0680
11	0.3708 + i5.4522	5.5518 + i22.4255
12	-6.6929 + i4.0722	5.4013 + i16.7326
13	-9.3638 - i4.9998	5.1498 + i11.1249
14	1.5872 - i15.4212	4.9665 + i5.6855
15	19.0024 + i3.6850	4.6296 + i0.3055

The propagation model for the Guassian source functions was adapted by Jeong et al[40] and Zhang et al[99] to account for both the linear and the second harmonic wavefields by taking the source equation in Eq. (4.18) and plugging it into Eq. (4.16). The solution to this equation was then combined with Eq. (4.17) to obtain the full wavefield expressions of the fundamental propagating wave and the generated second harmonic wave through the acoustic media. The linear and nonlinear wavefields respectively are provided in the

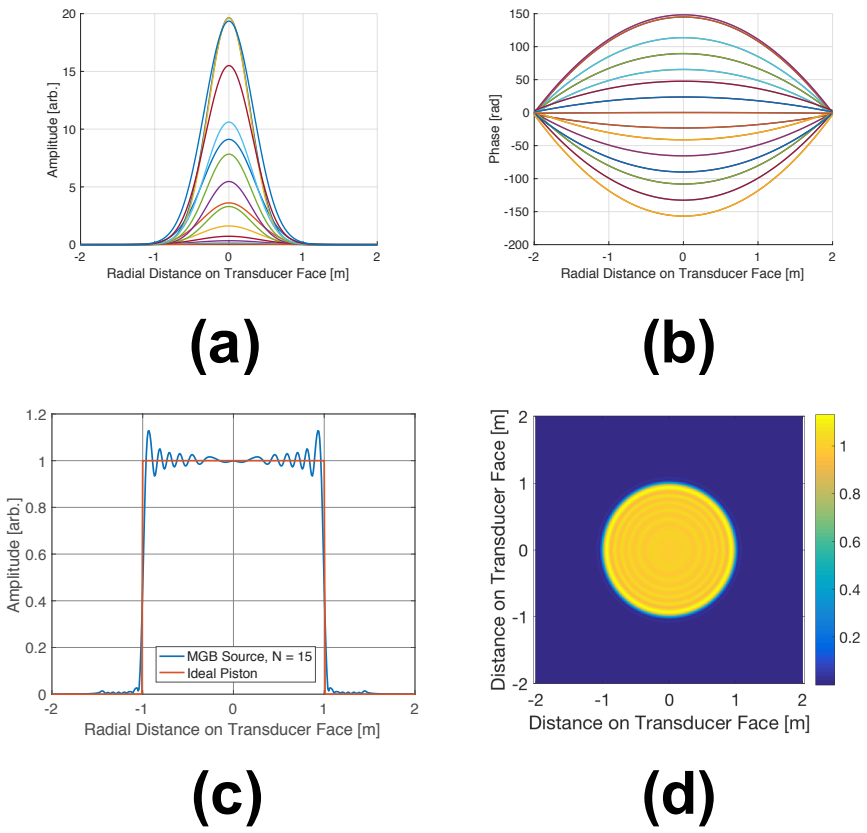

Figure 4.5: (a) and (b) show the individual contributions from the individual coefficients from tab. 4.1. (c) shows a comparison of and ideal piston source in red to a 15 term MGB approximation using Eq. (4.18) in blue. (d) shows the plan view of the piston approximation.

following expressions:

$$p_1(z) = [p_0 \exp(ikz)][M_1(\alpha_1, z)][D_1(a, f, z)] \tag{4.19}$$

$$p_2(z) = \left[\frac{\beta kz}{2\rho_0 c_0^2} \exp(2ikz)\right][M_2(\alpha_1, \alpha_2, z)][D_2(a, 2f, z)] \tag{4.20}$$

where p_0 is the source pressure, $\alpha_{1,2}$ are the attenuation coefficients of the fundamental and second harmonic waves in [Np/m], z is the propagation distance, a is the source radius, and f is the frequency of the fundamental excitation. The functions $M_{1,2}$ and $D_{1,2}$ are the attenuation correction and the diffraction correction for the fundamental and second

harmonic waves and are given as follows:

$$M_1(\alpha_1, z) = e^{-alpha_1 z} \tag{4.21}$$

$$M_2(\alpha_1, \alpha_2, z) = \frac{e^{-2alpha_1 z} - e^{-alpha_2 z}}{(\alpha_2 - 2\alpha_1)z} \tag{4.22}$$

$$D_1(a, f, z) = \sum_{n=1}^{N} \frac{A_n}{1 - iB_n z/D_R} \exp\left(\frac{B_n (r/a)^2}{1 - iB_n z/D_R}\right) \tag{4.23}$$

$$\begin{aligned} D_2(a, 2f, z) =& \frac{1}{z} \int_0^z \sum_{m=1}^{N} \sum_{n=1}^{N} \frac{-2A_m A_n B_b}{(2z + B_a)z' + B_a z - 2B_b} \\ & \times \exp\left\{-2ikr^2 \left(\frac{(z'^2 + B_a z' - B_b)/(z - z')}{(2z + B_a)z' + B_a z - 2B_b}\right)\right\} \mathrm{d}z' \end{aligned} \tag{4.24}$$

where $D_R = ka^2/2$ is the Rayleigh distance that marks the transition from the near field tot he far field, $B_a = i(B_m + B_n)/D_R$, $B_b = B_m B_n / D_R^2$, and $A_{m,n}$ are the set of complex valued coefficients that are determined the Gaussian source decomposition shown in Eq. (4.18). Because the diffraction correction in Eq. (4.24) has two nested summations, the 15 source terms will expand to 225 total terms of the subscripts a and b. One these terms have ben summed, an integration of the propagation distance domain takes place which accounts for the cumulative generation from SHG phenomena.

There are a few major assumptions made in the derivations of eqs (4.19 - 4.24). One of the biggest of these assumptions is the paraxial approximation, which is also apparent in the RSI model because of its use in formulating the KZK equation. The practical consequence of this assumption is that the diffraction and attenuation corrections are merely functions of z instead of the position vector $\mathbf{r}$. Additional assumptions include the system being weakly nonlinear which is true for most metallic and fluid specimens, axisymmetric geometry, and

that the quasilinear solution to the KZK equation is valid over the domain of interest, which is a reasonable assumption for the length scales and materials used in this work[94].

A comparison between the MGB model pressure field in Eq. (4.19) and the exact solution represented by eqs. (4.2) and (4.16) is shown in Fig. 4.6. It is clear from this figure that the near field values for the MGB model do not match the exact solution, but after a distance of roughly one transducer length, the model matches the exact solution almost precisely.

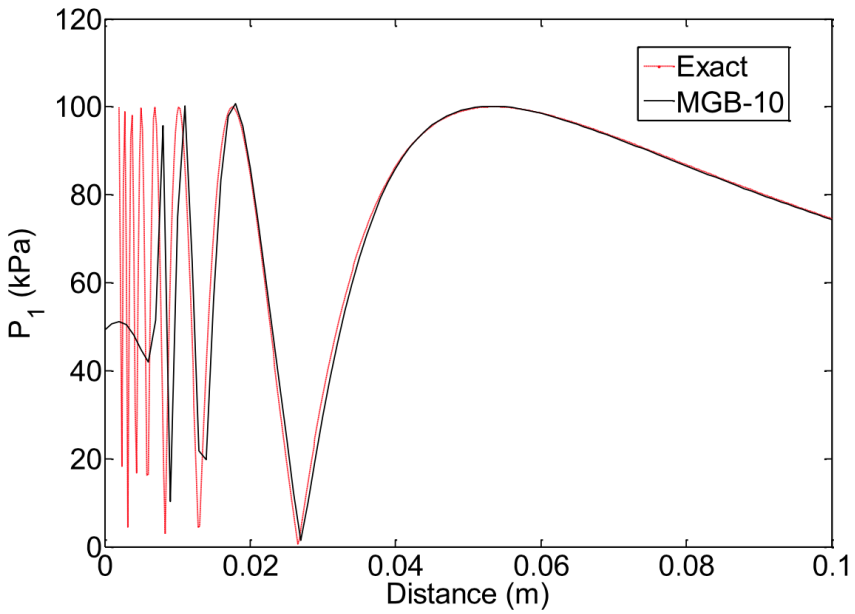

Figure 4.6: Comparison of on-axis pressure fields for fundamental wave from a 15 term MGB model compared to the exact solution from the RSI model.

The primary reason for using the MGB model is the ease with which the wavefields can be calculated numerically and further propagated across multiple interfaces. In the purely linear case, this can easily be done using a system of propagation matrices, which is numerically compact and can be constructed very easily in the common $ABCD$ matrix approach in a software package like MATLAB[91, 100, 101]. In the case of nonlinear propagation, this gets much more difficult to accomplish with a matrix approach and each interface must be considered seperately instead of in a compact mathematical form. Because our modeling requirements include the transmission of acoustic waves across a metal/air boundary, this

is a crucial problem in the modeling framework that will be addressed in the next section.

4.2.3 Transmission of longitudinal wavefields across material interfaces

As is shown in Fig. 4.1, a second material, in this case air, must be accounted for in the propagation path between the transmitting source and the receiving air-coupled transducer. To account for the transmission of the acoustic wave to the air gap, we must extend the nonlinear formulation of this MGB model to propagate through multiple layers, shown in figures 4.7(a) and (c). An optimization algorithm is used to re-derive the source function for the linear and nonlinear fields at the interface between material 1 and material 2, depicted in figures 4.7(b) and (d) respectively. These new coefficients are then used as the inputs to equations 4.19 and 4.20 above, which provides the total pressure field model for propagation in air.

One of the consequences of this formulation is that for both the fundamental and second harmonic waves, a linearly and nonlinearly propagating wave component is produced in the next material as shown in Fig. 4.8; of particular interest is how the second harmonic wave propagates through the second material in this schematic. In previous works[20], it was shown that for sources where there is an initial nonlinear component, the initial second harmonic component of the signal propagates as if it were a fundamental frequency wave at a frequency of 2ω. The interface between materials 1 and 2 in this problem can be thought of as a new "effective source" with coefficients $A_{\mathrm{int},2,N}$ and $B_{\mathrm{int},2,N}$ as shown in figures 4.7(a) and (c), where the subscript "int" represents their location at the interface, the numbers 1 and 2 represent the fundamental and second harmonic respectively, and N is the number of the coefficient in the set of newly derived coefficients. Again, an N of 15 shows excellent agreement with the wave fields at the interface as can be seen in figures 4.7(b) and (d). This is a very flexible approach to solving this problem because it works irrespective of the source profile (piston, Gaussian, etc.).

Additionally, one of the consequences of Eq. (4.20) is that the number of terms result-

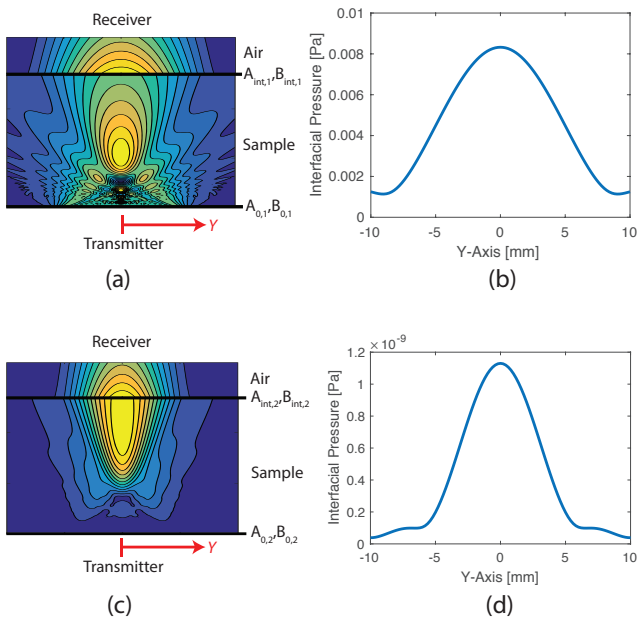

Figure 4.7: Schematic of the pressure fields for fundamental and second harmonic waves propagating through a sample. Parts and (a) and (c) show the wave fields for propagation starting at the transmitter at the bottom, traveling to the air/sample interface $(A_{\text{int},n}, B_{\text{int},n})$, transmitting into air, and impinging on the receiver surface at the top. Parts (b) and (d) show the pressure magnitude of the waves in air just after transmission across the interface calculated by Eq. (4.18) using the coefficients $(A_{\text{int},n}, B_{\text{int},n})$. Note that A_2 propagates as a second harmonic wave (Eq. (4.20)) with generation in the sample, but after transmission into the air, propagates as a fundamental wave (Eq. (4.19)).

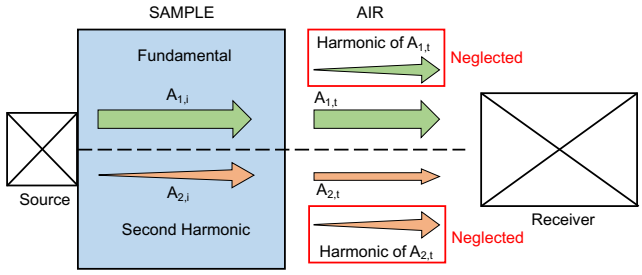

Figure 4.8: Schematic of the interface between solid and air diagramming the relevant incident and transmitted waves. Note that A_2 propagates as a second harmonic wave with generation in the solid, but after transmission into the air, acts as a fundamental wave. Once the waves reach the receiver, they are integrated across the face of the transducer to obtain the force on the transducer face.

ing from the summations squares each time the calculation is performed because of the double summation in the diffraction correction. For example, a discrete source of 15 terms

necessitates a second harmonic diffraction correction of 225 terms. When the fundamental and second harmonic wave-fields transmit across a material boundary, the number of total coefficients would square again because of the generation of higher harmonics from both the fundamental and second harmonic waves in the first material. A large stack of materials would quickly overwhelm most computations resources. By collapsing the wave field components, particularly of the second harmonic, to a new set of 15 coefficients down from 225, this problem is neatly side-stepped.

To select which field components dominate the fundamental and second harmonic fields of $p_{1,\text{air}}$ and $p_{2,\text{air}}$, we acknowledge that the transmission coefficient T at the interface between a metallic or silica specimen and air is very small. For an aluminum 2024/air interface, T is equal to 0.985e-4, and for a fused silica/air interface, T is equal to 1.28e-4. This can be interpreted as a representation of the insertion loss of the air gap between the receiver and the sample surface as it directly relates the pressure of the propagating waves in the sample material to the pressure of the wave propagating through the air. Because of these high insertion losses caused by the low values of T, the second harmonic generated by the transmitted fundamental wave component and especially the higher harmonics generated by the transmitted second harmonic wave are neglected due to their very small magnitude. This is shown pictorially in Fig. 4.8 where the red-boxed components are neglected because of their low magnitude relative to the other transmitted wave components. This leaves the transmitted fundamental wave accounting for $p_{1,\text{air}}$ and the linearly propagating transmitted second harmonic wave accounting for $p_{2,\text{air}}$, summarized in the equations below:

$$p_{1,\text{air}} = T\left[p_{1,\text{metal}}\big|_{z=L}\right] M_1\left(\alpha_{1,\text{air}}, z_{\text{air}}\right) D_1\left(a, f, z_{\text{air}}\right) \tag{4.25}$$

$$p_{2,\text{air}} = T\left[p_{2,\text{metal}}\big|_{z=L}\right] M_1\left(\alpha_{2,\text{air}}, z_{\text{air}}\right) D_1\left(a, 2f, z_{\text{air}}\right) \tag{4.26}$$

where L is the length of propagation through the sample.

Another important consideration is the effect of the boundary between metallic specimen and air on the phase of the transmitted pressure waves. For normal incidence of a plane wave on an interface between a material with a high acoustic impedance (metal) to a material with much lower acoustic impedance (air), a reflected wave will incur a 180 degree phase shift because the reflection coefficient will have a negative value approaching $R = -1$. However, the transmission coefficient will have a positive sign regardless of its magnitude, and thus transmitted waves across the boundary will transmit in-phase and will not need a sign adjustment[73]. While the incidence of the propagating waves near the edges of the propagating beam may not exhibit plane wave behavior precisely as shown in Fig. 4.4, the diffraction correction takes into account the spatial distortions that these edge waves experience and allows us to assume normal incidence for the entire wave front.

An example of the full modeling picture is given in Fig. 4.9 which shows a cross-section of an aluminum sample of 27 mm thickness and an adjoining air-column of 5 mm thickness through which the acoustic pressure wavefield propagates for both the fundamental (a,c) and second harmonic (c,d) frequencies. The second harmonic generation effect is clearly demonstrated in Fig. 4.9(c), which is the representation of Eq. (4.20). Additionally, the linear propagation of the transmitted pressure waves as denoted by Eqs. (4.25) and (4.26) are shown clearly in Fig. 4.9(b) and (d), with the signal attenuating and diffracting leading a monotonic amplitude decrease with propagation distance.

4.2.4 Received pressure at surface of the air-coupled transducer

When the air-coupled transducer of Fig. 4.1 receives the pressure wave propagating through the air column as in Fig. 4.9(b) and (d), it is responding to the total received force from the pressure field distribution across the surface of the transducer, which causes a strain through the piezoelectric element and thus a voltage from the piezoelectric effect. This is represented in modeling terms by examining the two port Sittig model of the receiver shown in Fig. 4.10, in which the mechanical port takes the receiver force and the trans-

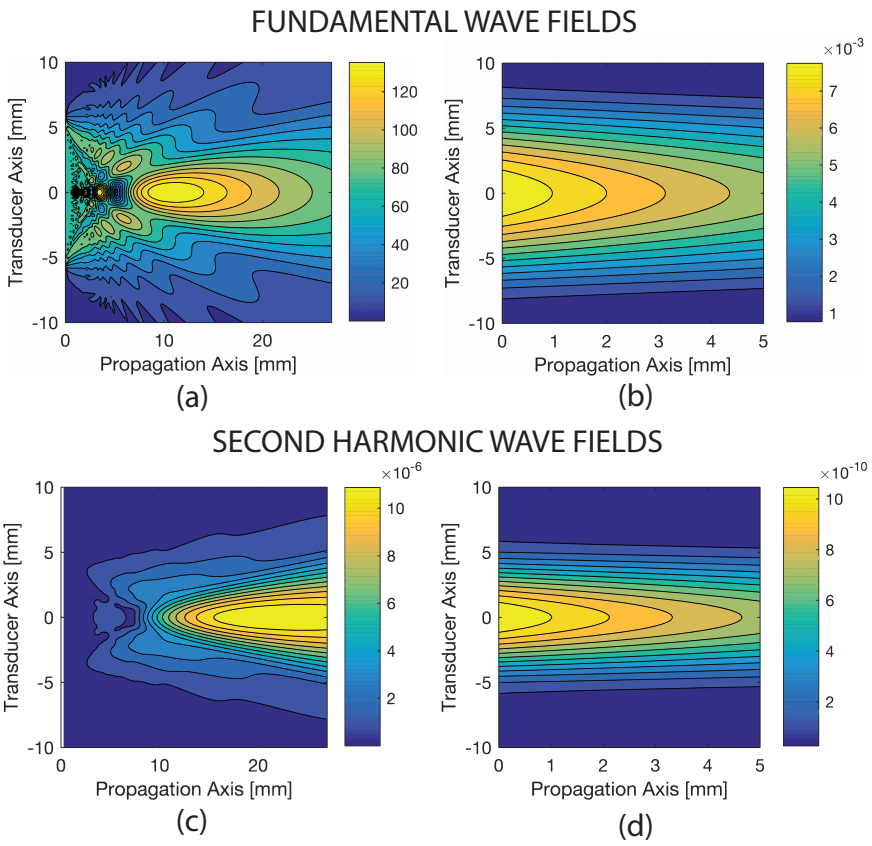

Figure 4.9: Contour map representation of the calculated wave fields in aluminum and air for the fundamental and second harmonic fields. The fundamental wave field for aluminum is shown in (a) and the fundamental wave field of the transmitted wave through air is shown in (b). Similarly, the second harmonic wave field in aluminum is shown in (c) and the second harmonic wave field of the transmitted wave through air is shown in (d). The contour lines are meant to highlight the diffraction and attenuation effects of the field components.

ducer sensitivity as a function of frequency and the transducer transfer matrix $[\mathbf{T}]$ converts that force into the voltage and current readings required to take electrical measurements. Therefore all that remains is to take the RSI or MGB model output and turn that into a value of received force, which is accomplished by simply integrating the pressure field across the surface of the transducer:

$$F_n(x', y') = 2 \int_A p_n(x, y) \mathrm{d}A \tag{4.27}$$

where A is the surface area of the receiving transducer element. The coordinate pair (x', y') is used to denote the center of the air-coupled transducer, which when scanned in the $x - y$

plane averages the pressure field across the transducer surface area centered at that location. The multiplication by 2 accounts for the fact that the transducer face is essentially a rigid boundary due to the high impedance mismatch between the transducer and the surrounding air.

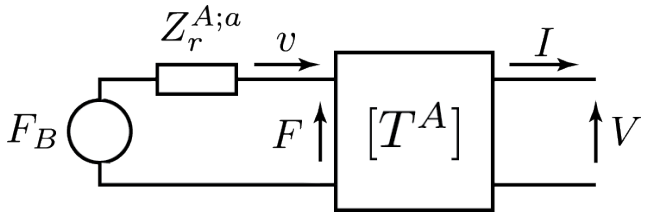

Figure 4.10: Model of a piezoelectric receiver for the measurement of the voltage and current when the receiver receives longitudinal acoustic waves[91].

A plot demonstrating the difference in the received force from the air-coupled transducer versus the actual pressure distribution across the transducer face is given in Fig. 4.11. Notably, the received force as a function of position has a much broader/flatter shape than the pressure distribution. This is due to the finite size of the receiver which essentially creates a moving average weighted by the modal response of the transducer element as contrasted to a point-like receiver such as a laser interferometer. For the frequencies of interest, the modal response of the transducer is assumed to be piston-like because the frequencies of interest are below or near the transducer fundamental resonance. This step completes the forward model from source transducer to receiving transducer for propagating longitudinal waves.

4.3 Rayleigh wave propagation modeling

A full model of a propagating Rayleigh wave for air-coupled measurement purposes consists of many of the same components as the longitudinal wave model. The propagation of the Rayleigh wave along the surface of the material leads to a leaked pressure wave from the sample into the surrounding air, which is then received at the surface of the air-coupled transducer. The following sections will detail each of these model components for use in

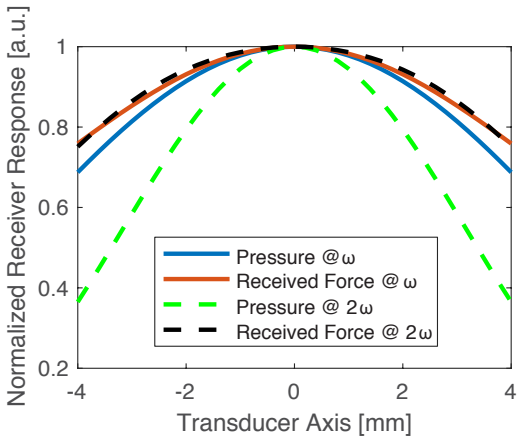

Figure 4.11: Plot demonstrating the differences in the apparent shapes of the pressure waves in the air column and the received force value when the center of the transducer is located at the same position. Both the fundamental (solid) and second harmonic (dashed) quantities are displayed.

optimization algorithms and the extraction of the nonlinearity parameter β_{11} from measured data.

4.3.1 Modeling of sample surface displacements

The modeling of a propagating Rayleigh wave is very similar to the quasilinear solution to the KZK equation for longitudinally propagating waves presented in sec. 4.2.2.3, and the results obtained by Shull et al[41] are detailed in sec. 2.2.2 for both the fundamental and second harmonic wave components. For easy reference, the solutions for the wavefields in terms of velocities are provided below:

$$v_1(x,y) = \frac{v_0 e^{-\alpha_1 x}}{\sqrt{1+ix/x_0}} \exp\left(\frac{-(y/a_1)^2}{1+ix/x_0}\right) \tag{4.28}$$

$$v_2(x,y) = \frac{i\sqrt{\pi}\beta_{11}v_{0,1}^2 k_0^2 a_1^2}{4c_{\mathrm{R}}\sqrt{i(\alpha_2-2\alpha_1)(x_0+ix)}} \times \exp\left(-\alpha_2 x - \frac{2(y/a_1)^2}{1+ix/x_0} + i(\alpha_2-2\alpha_1)x_0\right) \times \{\mathrm{erf}[\sqrt{i(\alpha_2-2\alpha_1)(x_0+ix)}] - \mathrm{erf}[\sqrt{i(\alpha_2-2\alpha_1)x_0}]\} \tag{4.29}$$

These equations provide the complete picture of the wavefield on the surface of a specimen in the x, y plane. An example of the wavefields modeled in eqs. (4.28) and (4.29) are shown in Fig. 4.12, from which the major properties of the fundamental and second harmonic field models can clearly be seen. The source term in this case is assumed to be Gaussian, which as discussed in the previous chapter is an accurate approximation of the wedge/transducer source. The effects of attenuation and diffraction can clearly be seen in the fundamental wavefield, and these effects coupled with second harmonic generation can be seen competing with each other in the second harmonic wavefield. This is evident from the fact that the wave amplitude increases due to generation as expected, but then decreases after reaching a maximum level because of the dissipation of energy from attenuation and diffraction effects.

The modeling picture provided in Fig. 4.12 is accurate for a perfectly linear source in which the only source components exist at the fundamental frequency, such that:

$$f(y,t) = v_{0,1}e^{-(y/a_1)^2}e^{-i\omega t} \tag{4.30}$$

where $v_{0,1}$ is the source strength at the fundamental frequency and a_1 is the effective source radius. As discussed in earlier sections, the source is not perfectly linear because of various factors including the multiple contact interfaces in the wedge/transducer assembly and the generation that occurs in the wedge material. In order to account for the effect of these nonlinearities in the model, we start by including a correction term in the source equation,

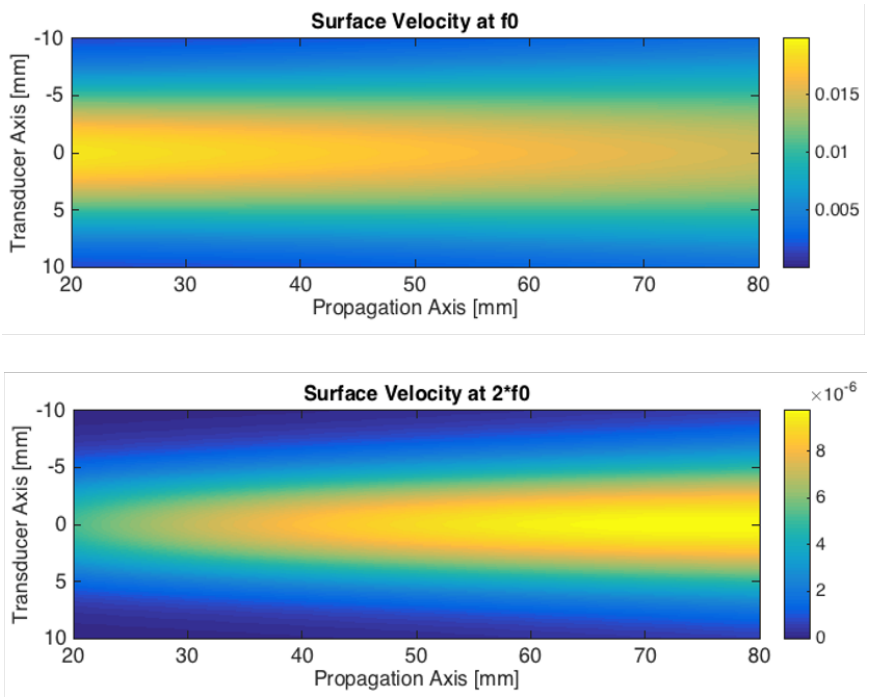

Figure 4.12: Velocity distributions of the fundamental (top) and second harmonic (bottom) waves on the surface a sample modeled by eqs. (4.28) and (4.29).

v_2^{T}, referred to as the source nonlinearity. This is shown in Eq. (4.31).

$$f(y,t) = v_{0,1}e^{-(y/a_1)^2}e^{-i\omega t} + v_{0,2}e^{-(y/a_2)^2}e^{-2i\omega t} \tag{4.31}$$

where $v_{0,2}$ is the source strength of the nonlinear correction term, a_2 is the effective radius of the correction term, and the propagation function contains 2ω in the exponent, signifying it contains information at the second harmonic frequency. Taking this revised source equation for $f(y,t)$ and plugging it into eqs. (4.13) and (4.14) we find that the second harmonic wave field solution becomes

$$v_2^{\mathrm{TOT}} = v_2^{\mathrm{M}} + v_2^{\mathrm{T}} \tag{4.32}$$

where v_2^{M} corresponds to the nonlinearity generated in the material as the fundamental wave propagates along x as described in Eq. (4.29), and v_2^{T} corresponds to the nonlinearity of the source, which takes the same form as a fundamental wave propagating through the

material at frequency 2ω and with properties corresponding to the material and source at this frequency. Together, the sum of these terms is equal to the total v_2, signified as v_2^{TOT}. Mathematically, the source nonlinearity is expressed in the following form:

$$v_2^{\mathrm{T}}(x,y) = \frac{v_{0,2}e^{-\alpha_2 x}}{\sqrt{1+ix/2x_0}}\exp\left(-\frac{(y/a_2)^2}{1+ix/2x_0}\right) \tag{4.33}$$

Eq. (4.33) differs from Eq. (4.28) in many ways. The attenuation of Eq. (4.28), α_1, is replaced in Eq. (4.33) by α_2 because the source nonlinearity occurs at 2ω. Similarly, the x_0 terms in Eq. (4.28) are replaced with $2x_0$ for the same reason. The final difference is the replacement of a_1 with a_2, which follows from the fact that the source has different apparent half-widths at every frequency.

The result of decomposing the measured second harmonic signal into the framework of equation (4.32) is shown graphically in Fig. 3.8 for values along the propagation axis $y = 0$, after converting the Rayleigh velocities v_2^{TOT}, v_2^{M}, and v_2^{T} into displacement amplitudes A_2^{TOT}, A_2^{M}, and A_2^{T} respectively. Note that because the Rayleigh velocities and the corresponding displacement amplitudes are directly related, they are referred to interchangeably in the context of this work.

Once the values of the surface displacements, velocities, and pressures are found, the next step in the modeling process is to predict the leaked wave amplitudes through the air across the metal/air interface and to the surface of the air-coupled transducer. This is the focus of the next section.

4.3.2 Modeling of leaked pressure wave from sample surface

4.3.2.1 2-Dimensional mode conversion analysis

The leaking of pressure waves off the surface of the metallic sample into a liquid acoustic medium (air is considered a liquid in this analysis) was first rigorously explored by Deighton et al[71]. In this analysis, the Rayleigh waves propagating along the sample

surface are considered to extend infinitely along the width of an infinite half-space shown in Fig. 4.13. If we discretize the sample surface into an infinite number of baffled point sources, each radiating a spherical wave due to the oscillatory particle motion from the propagating Rayleigh wave, then the combined effect of all these sources acting in unison with a coherent phase relationship results in a propagating longitudinal wave front at an angle from the surface equal to that in Eq. (2.18), as is shown in Fig.4.13(b).

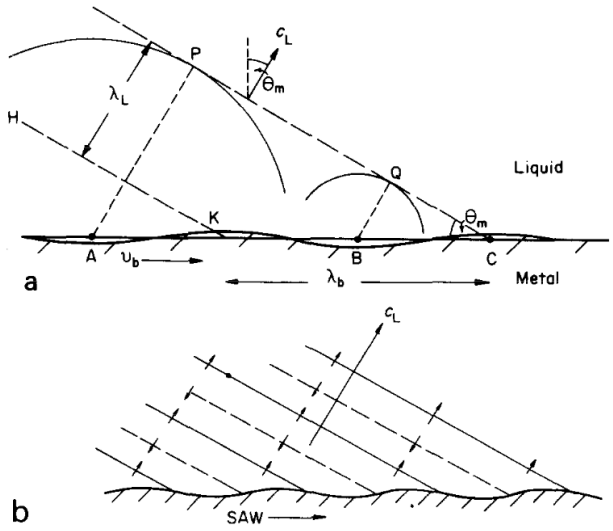

Figure 4.13: Demonstration of the physics behind leaked pressure waves from the surface of a sample as a Rayleigh wave propagates. (a) demonstrates the idea of the effects of infinite point sources acting as baffled simple sources radiating spherically into the air, forming a coherent wave front at an angle Θ_R from the vertical, and (b) shows how this sets up a propagating longitudinal wave at that same angle as the sources continue to oscillate[71].

The pressure wave amplitudes in the air can be calculated by considering the surface as divided into a large number of line sources extending into the median plane (into the page in Fig. 4.13) or length b and width $\mathrm{d}x$. We then integrate the contributions from each of these line sources to obtain the pressure at the point P in the air. This setup is shown in Fig. 4.14, which also takes into account the attenuation (but not the diffraction) of the Rayleigh wave as it propagates along the surface. For this derivation, the equivalent of the paraxial approximation is assumed, such that all points along the length b of the line sources is equidistant from P, and that along the length of propagation, all the distances from the

line sources to P are also approximately equal. This is in effect a far-field approximation.

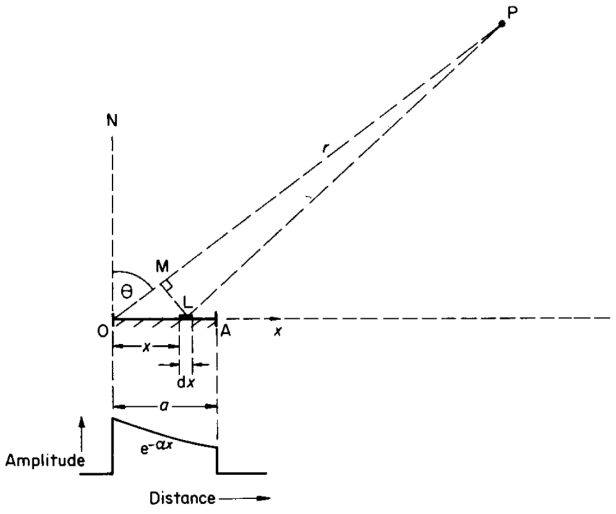

Figure 4.14: Diagramatic representation of the geometry in deriving the pressure at a point in the fluid from the combined contributions of a large number of line sources extending into the median plane[71].

If we assume that the acoustic pressure distribution immediately adjacent to the radiator surface is:

$$p_0 = \hat{p}_0 e^{-\alpha x} \cos(k_b x - \omega t) \tag{4.34}$$

where $\hat{p}_0$ is the amplitude at the source, α is the attenuation coefficient of the surface acoustic wave, k_b is its wave number, and ω is the angular frequency of the wave, then the contribution $\mathrm{d}p$ to the acoustic pressure P from the element L distance away from the source has an amplitude:

$$\mathrm{d}p = \frac{Abdx}{r} p_0 \left(x, t - \frac{LP}{c_L} \right) \tag{4.35}$$

In this equation A is a constant and r in the denominator is the physical manifestation of spherical spreading as in the RSI modeling described earlier in this chapter. The resulting

pressure at P is thus the integral of this expression, which equals:

$$p(r,\theta,t) = \frac{Ab\hat{p}_0}{r}\int_0^a e^{-\alpha x}\cos\left[k_b x - \omega\left(t_0 + \frac{x\sin\theta}{c_L}\right)\right]\mathrm{d}x \tag{4.36}$$

This is a useful approximation of the pressure in the air, but the far-field approximation is difficult to achieve experimentally because the leaked longitudinal wave attenuates rapidly as it propagates through air, quickly becoming extremely difficult to measure even with the most sensitive piezoelectric transducers[19]. A more accurate, but again more computationally expensive, model for calculating effects nearer to the field of the radiating surface is to adapt RSI modeling to this framework by adding a phase term to the complex pressure that accounts for the coherent phase difference of the discrete sources along the surface of the sample from the propagating Rayleigh wave. Additionally, the assumption that the amplitude along each individual line source is constant does not match the modeling picture described by Fig. 4.12 in which each line source would really have a Gaussian profile. For these reasons, we turn to an RSI model for the propagation of the leaked pressure wave to the surface of the receiver, and this is described in the next section.

4.3.2.2 RSI modeling of leaked pressure wave

In order to adapt the RSI model proposed in sec. 4.2.2.2 to the case of the leaked pressure waves from the surface of the sample for Rayleigh wave propagation, we must add a phase term to the integral of Eq. (4.28) and (4.29). This phase term is the delay shown in Fig. 4.13(a) between the sources "firing" as the Rayleigh wave front passes through each point, which is currently not a part of the surface amplitude modeling which only accounts for the steady state wave amplitudes with position. This phase delay is introduces as follows:

$$v_1(x,y) = \frac{v_0 exp{-\alpha_1 x}}{sqrt1 + ix/x_0}\exp\left(\frac{-(y/a_1)^2}{1+ix/x_0}\right)\exp(ik_1 x) \tag{4.37}$$

$$
\begin{aligned}
v_2(x,y) =& \frac{i\sqrt{\pi}\beta_{11}v_{0,1}^2 k_0^2 a_1^2}{4c_{\mathrm{R}}\sqrt{i(\alpha_2-2\alpha_1)(x_0+ix)}} \\
&\times \exp\left(-\alpha_2 x - \frac{2(y/a_1)^2}{1+ix/x_0} + i(\alpha_2-2\alpha_1)x_0\right) \\
&\times \{\mathrm{erf}[\sqrt{i(\alpha_2-2\alpha_1)(x_0+ix)}] - \mathrm{erf}[\sqrt{i(\alpha_2-2\alpha_1)x_0}]\} \\
&\times \exp(ik_2 x) \qquad (4.38)
\end{aligned}
$$

where $k_{1,2}$ are the wave numbers for the fundamental and second harmonic frequencies. The only real additions to the field equations listed above are the additions of the exponential terms at the end that account for the phase discrepancy at each point. This changes the sources from all firing in phase (as in the longitudinal case which is where the RSI model was derived previously) to firing as the Rayleigh wave front passes through the point. The consequence of this is the angled wave fronts depicted in Fig. 4.13(b) and described in the Deighton et al results[71]. With the RSI modeling Eq. (4.9) applied to each discrete source on the surface with amplitude and phase described by eqs. (4.37) and (4.38), the modeling of the leaked pressure wave from a propagating Rayleigh wave is complete, and all that remains in the modeling is to account for the pressure at the surface of the air-coupled transducer.

4.3.3 Received pressure at surface of the air-coupled transducer

Because both the longitudinal and Rayleigh wave modeling cases result in longitudinal waves propagating through the air to the surface of the air-coupled transducer, they are both handled from a modeling perspective in the same way at the last modeling step. We therefore apply Eq. (4.27) to the wavefield where the receiver is located and determine the overall force on the transducer face. For the Rayleigh wave case, the contrast between the apparent projection of the air-coupled transducer area to the sample surface is stark when compared to the pressure distribution across the receiver face, as is shown in Fig. 4.15.

Looking the the received pressure field at the surface of the transducer, it is obvious that the profile is drastically different from that of the projected field of view of the receiver viewing the surface pressure profile. This discrepancy comes from the geometry of the problem and attenuation through the air of the longitudinal waves because the trailing edge of the receiver has a longer distance from the receiver to the sample surface than the leading edge, which means more attenuation through air of the longitudinal wave front takes place and thus the amplitude is reduced. This effect is a prime example of why the modeling of the leaked wave is so important to the optimization results, and why the indirect nature of the air-coupled transducer measurement can be such a tricky concept to understand and model.

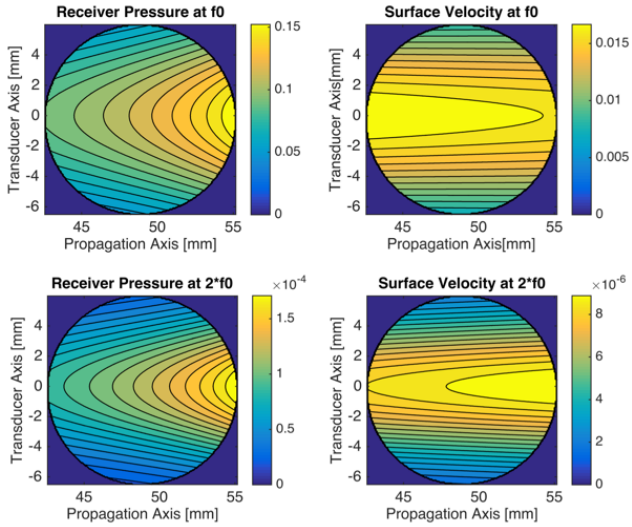

Figure 4.15: Comparison of the pressure field across the circular face of the receiver (left column for fundamental [top] and second harmonic [bottom]) and the projected field of view on the sample surface (right column for fundamental [top] and second harmonic [bottom].

Once the integrated force value is obtained, we have the full modeling procedure for both the longitudinal and Rayleigh wave measurement cases completed, and it is time to use a nonlinear optimization algorithm to match the models to the measured data and extract the nonlinearity parameters, β and β_{11}.

4.4 Inverse problem solution using nonlinear least-squares optimization

4.4.1 Optimization equations

Ultimately, we need to take measured voltages from the air-coupled transducer and use these voltages to infer the surface wave amplitudes on the sample. This type of measurement fits neatly into an inverse problem formulation that can be solved numerically using nonlinear least-squares optimization[20, 31]. The cost function for this optimization is the calculated force on the surface of the air-coupled receiver due to the radiation of the pressure waves from the surface of the metallic sample derived in the previous section. The process of nonlinear least squares optimization solves the cost function given input values of the problem variables $F_n(p_0, \alpha_1, \alpha_2, a, f, \beta)$ and iterates those values in a methodical manner until the calculated force on the air-coupled transducer surface matches experimentally determined values. This is stated mathematically in Eq. (4.39).

$$\min_{\{p_{0,n},\alpha_n,\beta\}\in\Re} \|F_n(\{p_{0,n},\alpha_n,\beta\},x,y) - F_n^{\mathrm{MEAS}}\|_2^2 = \min_{\{p_{0,n},\alpha_n,\beta\}\in\Re} \sum_i [F_n(\{p_{0,n},\alpha_n,\beta\},x_i,y_i) - F_{n,i}^{\mathrm{MEAS}}]^2 \tag{4.39}$$

where F_n represents the force calculated through integration of eqs. (4.19) and (4.20) for the longitudinal wave case and Eq. 4.9 applied to eqs. (4.37) and (4.38) for the Rayleigh wave case over the receiver surface for the n^{th} harmonic and F_n^{MEAS} represents the measured forces at these harmonics.

An important facet of this optimization is that instead of using data from one measurement along the acoustic axis of the generated and receiving transducers as in a typical contact measurement, the entire measurement field consisting of discrete scan points is used. This field measurement based reconstruction is advantageous over a single measurement reconstruction because the redundancy provided by multiple measurements helps to

avoid convergence on local minima and provides a more stable result representative of the correct values. When using a single measurement point, there is a possibility of multiple solutions to the set of minimization variables that may provide similar values of the cost function, which is avoided in the field measurement based reconstruction approach.

4.4.2 Longitudinal waves

In the case of longitudinal waves, the optimization process is broken up into two steps, solving Eq. (4.39) for n = 1 (the fundamental) first, which only relies on the variables $\{p_0, \alpha_1\}$, and then solving using the curve-fit solutions for those variables as inputs for solving the optimization equation for n = 2 (the second harmonic). The second harmonic depends on the variables $\{p_0, \alpha_1, \alpha_2, \beta\}$, only two of which are still unknown. By completing the optimization in two steps, we reduce the number of optimization variables for each part of the problem, increasing the likelihood of convergence. By choosing appropriate guess values based on knowledge of the materials involved, the convergence speed of the nonlinear least-squares algorithm is greatly increased, and convergence on local minima can be avoided.

After the optimization of the second harmonic information is completed, the output of the algorithm includes the sought-after parameter β. If the experimental force values F_n^{MEAS} are properly calibrated values based on the transfer function of the receiving transducer, then the value of β that results from the algorithm of Eq. (4.39) will be the absolute β of the material.

4.4.3 Rayleigh waves

For the Rayleigh wave case, many of the pieces of information required for calculation of this fit, especially the source terms, are difficult to observe and quantify with the experimental setup and available equipment. These parameters become curve-fitting parameters themselves in order to guarantee that they are correctly accounted for in the fitting pro-

cess, however adding additional parameters can increase the likelihood of a false fit due to the introduction of local minima in the optimization space. Because blind fitting to these parameters amplifies the risk of solutions at local minima, the optimizer is seeded with guesses for the input parameters that are based on theoretical and experimental insight. The effect is two-fold: the optimizer converges to a solution closest to values that make physical sense, and the optimization time is reduced. The correct starting guesses for the optimization parameters are either obtained from theory, comparable literature values, or experiments. The complete data-processing and curve-fitting procedures used in the experiments performed in this paper are detailed in Fig. 4.16, but germane to this discussion are the steps in Fig. 4.16(c) and (d). In Fig. 4.16(c), the fundamental amplitude is used to find values of $p_{0,1}$ and α_1, which is a well-defined optimization because the amplitude is almost entirely defined by $p_{0,1}$ and the shape of the data is defined by α_1. These values are used later in the fitting process for the second harmonic data, which is first fit using a linear approximation over the first n data points depending on the qualitative size of the "linear region" to get an initial value for $p_{0,2}$ in (d). By providing physically grounded and internally consistent values for these optimization steps, the final fitting in step (e), where the second harmonic information is fit using Eq. (4.32), can be assured to conform to the physics of the problem.

The process until the step shown in Fig. 4.16(c) is nearly identical to the results published on this topic in Thiele et al[102] on measurements taken with air-coupled transducer setups. However, that work measures the parameter $\beta' \propto A_2/A_1^2$ instead of calculating β_{11} as described in Shull et al[43].

The step shown in Fig. 4.16(c) provides the basic source strength and attenuation information from the fundamental frequency component of the filtered response, but it's important to remember that these values are affected by the transfer functions of all of the components in the system (two transducers, electrical equipment, etc.). Therefore these parameters are all relative until these transfer functions are identified.

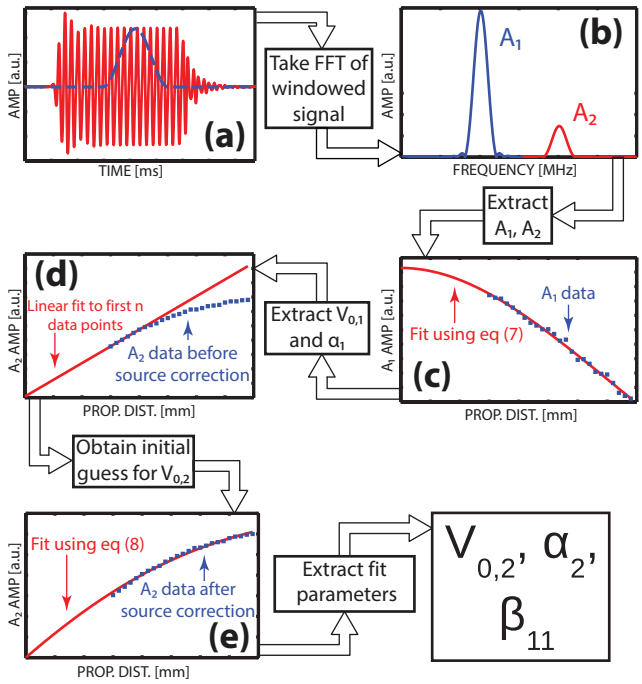

Figure 4.16: Diagrammatic representation of the curve-fitting procedure used to calculate the nonlinearity parameter of the measured specimen. (a) shows the signal from the receiving transducer (red) and the Hann window (dashed blue) used to filter it. This is processed with an FFT and (b) shows the frequency content at the fundamental (blue) and the second harmonic (red). The fundamental amplitude is then fit using Eq. (4.37) in (c), and the fit parameters $v_{0,1}$ and α_1 are extracted and used later to fit the second harmonic data. The second harmonic data without source correction is linearly fit using the first n data points (between 5 and 10) in order to get an initial value of $v_{0,2}$ to which the curve-fitting process is sensitive. This is then used in (e) to fit the A_2 data while correcting for the source nonlinearity. The resulting values of the fitting parameters are the desired results.

Fig. 4.16(d) is important because it provides an initial guess for the curve-fitting parameters in the step shown in part (e) and is essential for ensuring convergence and solution accuracy. The result of the nonlinear curve-fitting operation in Fig. 4.16(e) is the final value of the nonlinear source strength, the second harmonic attenuation, and ultimately β_{11}. The only thing that remains before the extracted nonlinearity parameters are absolute measures is the characterization of the air-coupled receiver, which is covered in the next chapter.

4.5 Summary

This chapter discussed the underpinnings of propagation modeling of longitudinal and Rayleigh wave transmission from source to receiver and provided a framework for using these models in an optimization algorithm to measure the acoustic nonlinearity parameter. The major points of this chapter are listed as follows:

- Modeling the full propagation of acoustic waves from source to receiver when measuring with air-coupled transducers requires three discrete steps: modeling of the acoustic wave propagating through the sample, the transmission or leakage of the acoustic wave into the air, and propagation through the air to the surface of the air-coupled transducer

- For the longitudinal wave measurement, there are three distinct modeling frameworks to take advantage of: RSI modeling, Quasilinear Solutions to the KZK equation, and MGB modeling. Of these three modeling paradigms, MGB modeling is the most attractive because of the accuracy and flexibility of the solution coupled with its computational efficiency.

- Propagation across the metal/air interface is handled by creating a new set of source coefficients at the surface of the sample, which allows for propagation of the nonlinear wave information in addition to the linear wave components. This solutions also reduces the computational load of the increasing number of terms in the nonlinear wave with each interface.

- For Rayleigh wave modeling, Shull et al derived a set of useful equations to predict the wave amplitudes on the surface of the sample which were modified to include phase differences across the sample surface with propagation distance. This was then combined with RSI modeling to predicted the wavefield at the surface of the air-coupled transducer.

- Nonlinear least-squares optimization is a useful tool for solving the inverse problem that is posed by air-coupled measurements in predicting surface displacements. If the measurements taken by the receiver are calibrated measurements, this optimization will yield absolute nonlinearity parameters. Otherwise, results are relative nonlinearity parameters.

CHAPTER 5
RECEIVER CHARACTERIZATION

5.1 Motivation

Before we can make absolute measures of β and β_{11}, we need to characterize the air-coupled transducer to provide absolute displacement information of the received waveform in air. As was stated in sec. 4.4.2 and 4.4.3, once we get calibrated data from the air-coupled receiver, the optimization results will provide absolute values of the optimization parameters which includes the nonlinearity parameter. Therefore we need to establish a way to calibrate the transducer.

In this work, a hybrid experimental/model-based based approach was employed to provide a transfer function between the received force on the surface of the air-coupled transducer and the output voltage from the transducer electrical port. A transducer calibration, in broad terms, is comparing a known displacement to the measured response at the transducer output. Therefore, we need to create a known input to the system in the form of a reference, and then compare that to measurements. This is done through a similar nonlinear optimization routine to that described before because of the indirect nature of the air-coupled measurement and the fact that we cannot vibrate the surface of the air-coupled transducer directly. The experimental portion of the calibration, which is establishing the reference, is confirmed with laser interferometric measurements of the reference surface displacement. These measured displacements are then used as inputs to a longitudinal wavefield model using the MGB framework as before, which in conjunction with a nonlinear optimization algorithm is compared to measured data. From this, we can establish the relationship between the displacement at the receiver surface to the measured voltage, completing the calibration routine and allowing us to measure absolute nonlinearity parameter

values.

5.2 Self-reciprocity calibrations

One of the primary methods of transducer calibration in the past has been through self-reciprocity calibrations, in which the transducer being characterized is used as both a transmitter and receiver to determine its transfer function. There are many ways to perform a self-reciprocity calibration[24–26], but the most commonly used method involves using the transducer in pulse echo mode and measuring the input current and voltage while transmitting and the received current and voltage while receiving, then using this information to formulate the frequency response. This method of calibration is based on the face that the transducer is a reciprocal device, or rather it has the same properties in transmission as in reception. A description of the theory behind self-reciprocity calibration is provided in the next section.

5.2.1 Self-reciprocity calibration theory

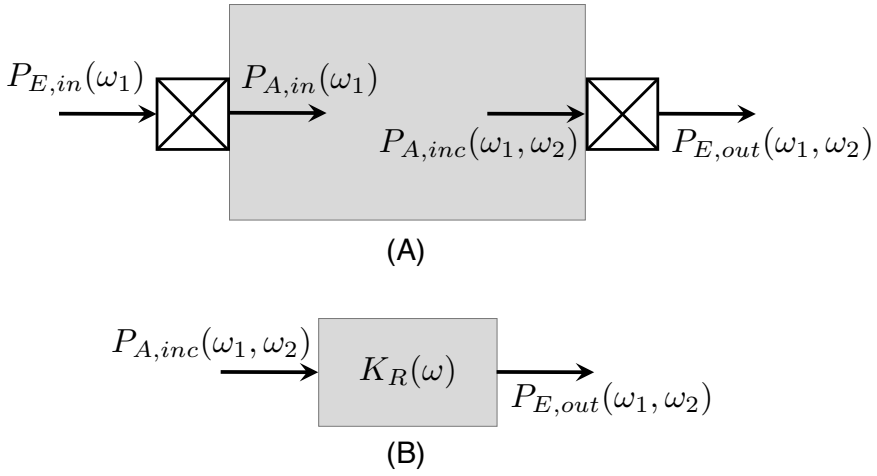

Figure 5.1: (A) Contact-transducer pitch catch operation schematic for SHG experiments. (B) Block diagram representation with the transducer conversion function between acoustic and electric energy domains[24].

For a standard SHG experiment with contact transducers as the source and receiver, a

diagrammatic representation is provided in Fig. 5.1 where $P_{E,in}(\omega_1)$ is the monochromatic electric power at the transducer input, $P_{A,in}(\omega_1)$ is the converted acoustic power at the fundamental frequency generated in the sample from the source transducer, $P_{A,inc}(\omega_1, \omega_2)$ is the incident acoustic power on the receiver surface containing the fundamental and second harmonic frequencies from the SHG phenomenon, and $P_{E,out}(\omega_1, \omega_2)$ is the electric power measured at the receiver from the converted incident acoustic wave. Because the source transducer has a resonant frequency near the fundamental of the generated wave by experimental design (and thus the generated wave is monochromatic in frequency content), the only important conversion from acoustic to electrical energy is the conversion efficiency of the receiving transducer, $K_R(\omega)$. Therefore a block diagram of the receiver can be summarized as shown in Fig. 5.1(b), and the incident acoustic power on the surface of the transducer can be represented according to the measured electrical power as:

$$|P_{A,inc}(\omega_1, \omega_2)| = \frac{|P_{E,out}(\omega_1, \omega_2)|}{K_R(\omega)} \tag{5.1}$$

and one can make the appropriate substitutions for electrical and acoustic power to come up with the more detailed representation of Eq. (5.1) as follows:

$$\frac{1}{2}|\omega A_{inc}(\omega)|^2 \rho v a = \frac{\frac{1}{2}|I_{out}(\omega)|^2 \mathrm{Re}(Z_s)}{K_R(\omega)} \tag{5.2}$$

where $A_{inc}(\omega)$ is the peak displacement amplitude as a function of frequency, ρ is the material density, v is the longitudinal ultrasonic velocity in the material, a is the area of the receiving transducer, $I_{out}(\omega)$ is the measured output current from the receiver, and Z_s is the passive output impedance of the receiving transducer. A transducer transfer function relates the mechanical disturbance at the transducer face to the measured electrical output, so we need to find the relationship between $A_{ince}(\omega)$ and $I_{out}(\omega)$ in Eq. (5.2). Rearranging,

we find the following relationship:

$$|A_{inc}(\omega)| = H(\omega)|I_{out}(\omega)| \tag{5.3}$$

where

$$H(\omega) = \sqrt{\frac{\mathrm{Re}(Z_s)}{\omega^2 \rho v a K_R(\omega)}} \tag{5.4}$$

Therefore we need to find the transfer function $H(\omega)$ in order to determine the absolute received wave amplitudes from the measured electric output of the receiver, which is precisely the last step we required from the results of the last chapter in order to find absolute measurements of β and β_{11}. In order to find this transfer function, we can rearrange the diagrammatic representation of the transducer and material system in Fig. 5.1 into a configuration only involving the receiver, as shown in Fig. 5.2(a). In this figure, we have the power input $P_{E,avail}(\omega)$ in the form of a broadband pulse from a pulser-receiver and the measured power at the receiver output $P_{E,out}(\omega)$ from the first back wall echo (this is commonly referred to as a pulse-echo configuration).

From the block diagram shown in Fig. 5.2(b), we can see that the relationship between the input and output electrical powers is defined as:

$$|P_{E,out}(\omega)| = K_R^2(\omega)|P_{E,avail}(\omega)| \tag{5.5}$$

The relationship described in Eq. (5.5) is very useful because it demonstrates the relationship between the measured input power, which can be converted into current I_{in} and voltage V_{in} to the transducer output from the reflected acoustic wave in terms of output current I_{out} and output voltage V_{out}. If we make the appropriate substitutions for the electric

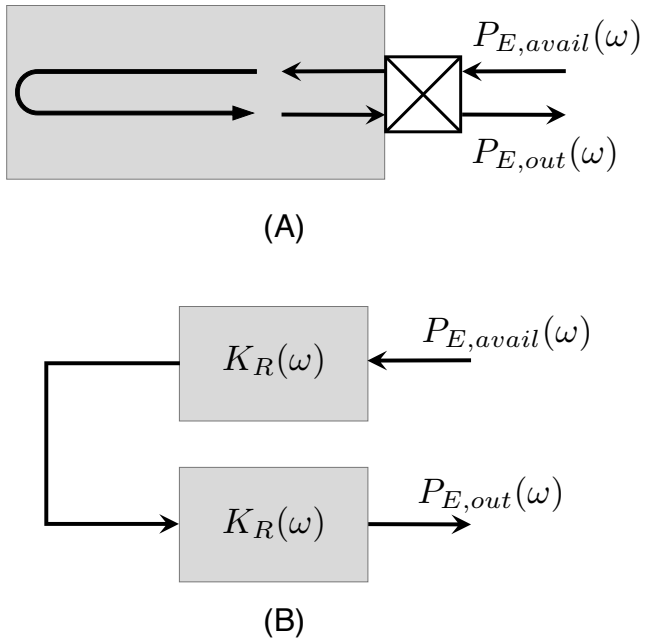

Figure 5.2: (A) Diagram of the receiving transducer calibration in self-reciprocity (pulse-echo) calibration. (B) Block diagram representation with the transducer conversion function for self-reciprocity calibration measurement[24].

powers in terms of voltages and currents, we arrive at an expression for $K_R(\omega)$ as follows:

$$K_R(\omega) = \frac{2|I_{out}(\omega)|\mathrm{Re}\left(\frac{V_{out}(\omega)}{I_{out}(\omega)}\right)}{\left|I_{in}(\omega)\left(\frac{V_{out}(\omega)}{I_{out}(\omega)}\right) + V_{in}(\omega)\right|} \tag{5.6}$$

which when we substitute Eq. (5.6) into Eq. (5.4), we find the transfer function $H(\omega)$ expressed in terms of measurable electrical quantities:

$$|H(\omega)| = \sqrt{\frac{\left|I_{in}(\omega)\left(\frac{V_{out}(\omega)}{I_{out}(\omega)}\right) + V_{in}(\omega)\right|}{2\omega^2\rho v a|I_{out}(\omega)|}} \tag{5.7}$$

5.2.2 Self-reciprocity calibration experimental setup

A standard pulse-echo configuration for the self-reciprocity calibration procedure detailed in sec. 5.2 is shown in Fig. 5.3, which allows for the measurement of the input and output current and voltages to and from the air-coupled transducer through the use of current and

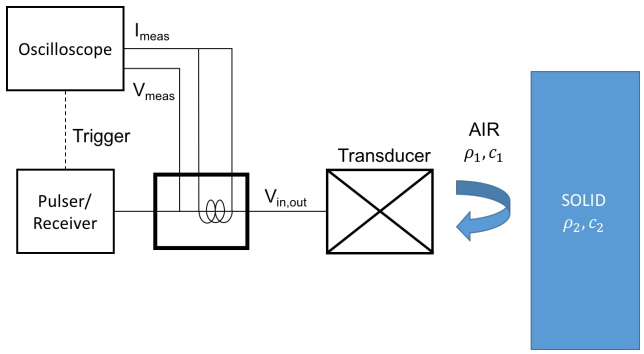

Figure 5.3: Pulse echo experimental setup for self-reciprocity calibration of the air-coupled transducer. Note that the acoustic medium in this configuration is air, and the back wall echo is off the air-metal interface.

voltage probes respectively. The setup used to conduct the calibration of the Ultran NCT4-D13 air-coupled transducer consisted of a Panametrics 5052PR pulser-receiver broadcasting a 400 Vpp broadband pulse at a repetition rate of 500 Hz and a damping of 50 Ohms to impedance match the receiver. The current probe was a Tektronix P6021 probe with a sensitivity of 2 mA/mV, and the voltage probe was a Tektronix P6138 probe witha range up to 350 MHz. The received signal was heavily filtered using the analog filters in the 5052 PR at settings of 1 MHz high pass and 5 MHz low pass at an amplification of 60 dB, without which the signal quality and strength was unsuitable for digitization by the oscilloscope, which was a Tektronix 5034B DSO. The nominal center frequency of the air-coupled transducer is 4 MHz (3.9 MHz actual center frequency) with a 12.5 mm diameter. The measured input and output waveforms were processed in MATLAB using the built-in FFT function. The results of the self-reciprocity calibration are shown in the next section.

5.2.3 Results of self-reciprocity calibration

The FFTs of the measured input and output currents and voltages are shown in Fig. 5.4, and it is immediately obvious how messy the measured results are when using the standard pulse-echo configuration with the air-coupled transducer. The noise level in the measurements is quite high, and the there are features such as the noise peak at 8 MHz and the erroneous dual peaks near 4 MHz that cannot be accounted for by the transducer or the

electrical response. These erroneous characteristics arise from various experimental factors, notable the necessity to analog filter the data to remove the significant noise present in the measurement and amplification stages. Correcting for the transfer functions of these analog components is extremely difficult without access to the internal electronics of the devices and was therefore not possible for this experiment. The transfer function resulting from the measurements shown in Fig. 5.4 and applied to Eq. (5.4) is shown in Fig. 5.5.

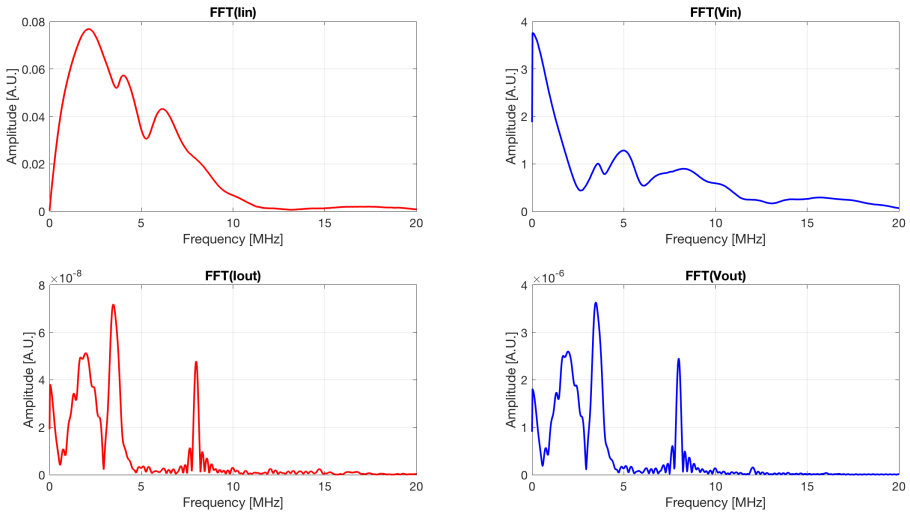

Figure 5.4: FFTs of, starting from the top left and moving clockwise, the input current, the input voltage, the output voltage, and the output current read from the voltage and current probes in the experimental setup shown in Fig. 5.3. Note the irregularities of the output signals, particularly the high frequency noise and and the dual peaks near 4 MHz which are not characteristic of the NCT4-D13 transducer.

It is clear from the transfer function obtained from Eq. (5.4) that this method does not provide clean calibration results for the frequency range of interest and for the technologies of interest in this work, namely the megahertz range air-coupled ultrasonic transducer. There are many reason for the inadequacy of self-reciprocity calibrations for air-coupled transducers, primary among them that air-coupled transducers cannot transmit a high enough power signal to obtain a clean calibration curve. The low SNR obtained from these measurements testifies to this reality, and the only way to overcome this shortcoming would be to put more voltage through the transducer, which runs the risk of depolling the

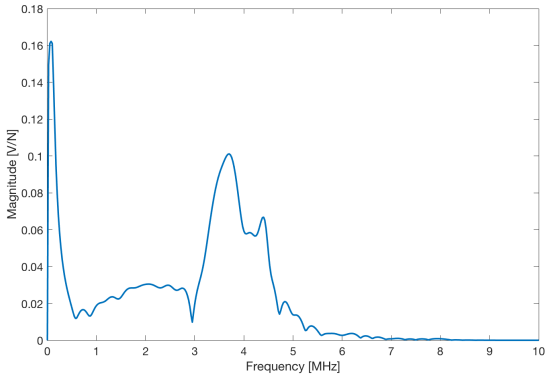

Figure 5.5: Result of self-reciprocity calibration from the pulse-echo experimental setup shown in Fig. 5.3 of the air-coupled transducer. Of note are the erroneous peaks around 4.2 MHz and the anti-resonance near 3 MHz, neither of which are characteristics of the NCT4-D13 transducers.

piezoelectric element[22]. The low pressure amplitude signal is also difficult to measure because of the high insertion loss of the transducer in air; even though the air-coupled transducer is optimized to receive acoustic wave traveling through air as an acoustic medium, there is still a significant acoustic impedance mismatch between the transducer wear plate and the surrounding environment. This is an unavoidable reality of nearly all piezoelectric devices. Finally, the high attenuation and diffraction of longitudinal acoustic waves as they propagate through air means that even a high power signal will experience significant losses over short propagation distances, and certainly the distance required to measure in the far field of the air-coupled transducer would not sustain the pulse-echo measurements required for self-reciprocity calibrations. For this collection of reasons, we must look to alternate methods for air-coupled transducer characterization.

5.3 Model-based experimental calibration

In order to circumvent the issues discussed in sec. 5.2.3, a model-based calibration approach was developed to adapt to the realities of air-coupled transducer technologies. This method combines the use of a reference sample that is a known source and propagating that source using the appropriate longitudinal propagation equations to determine the pressure

amplitude at the surface of the air-coupled transducer. This amplitude is then converted to a force value, which is correlated to the output voltage at the receiver obtained from experiments. This setup allows for high SNR calibration measurements and sidesteps the requirement of reciprocity of the transducer because we are only relying on its receiving properties. Because testing for reciprocity is extremely difficult[91], lifting this requirement is useful for calibrating a variety of transducer types.

5.3.1 Model-based calibration theory

The desired end-result of the air-couple transducer calibration is to provide a transfer function between a parameter obtained from the propagation modeling to the measured output from the transducer from experiments. Because the final result of the propagation modeling is the total force on the transducer face, it makes sense to choose this modeling parameter to relate to the measured experimental voltage. Therefore the desired transfer function that we are trying to calculate is the following:

$$H(\omega) = \frac{F^{\mathrm{CALC}}}{V^{\mathrm{MEAS}}} \tag{5.8}$$

This is justified by the fact that the electromechanical model used to define the transducer operation is based on the conversion of the received force to the electrical transducer output as shown in Fig. 4.10. In order to predict the force on the transducer face, we use a calibrated source as the basis for the modeling equations, and this setup is shown schematically in Fig. 5.6. There are therefore three steps to calculating the transfer function of the air-coupled transducer: Determine the source amplitudes to plug into the propagation modeling, Model the acoustic propagation from the source to the face of the transducer, and compare the modeling output to the measured voltage.

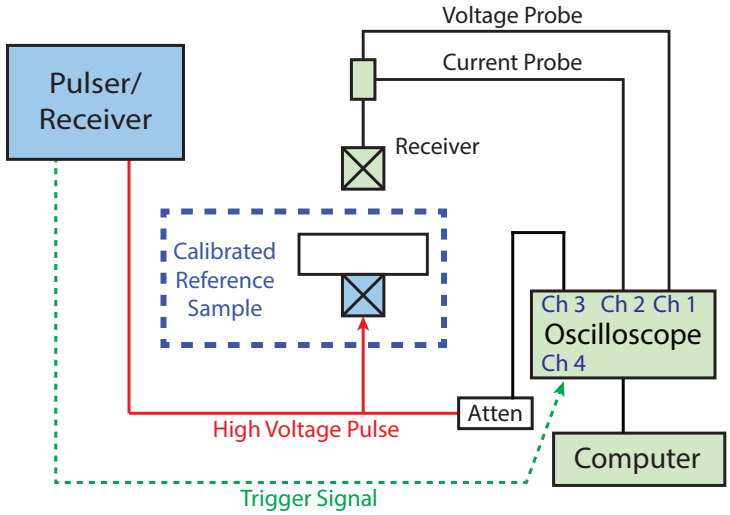

Figure 5.6: Experimental setup for model-based calibration method, using a commercial contact transducer coupled to an aluminum sample as the "calibrated reference sample".

5.3.1.1 Calibrated source characterization

The profile of the source is based on the measured source amplitudes of the calibrated reference sample in Fig. 5.6. This reference sample is comprised of a commercial contact transducer coupled to an aluminum block, and the amplitude of the vibration on the opposite face is measured by a laser interferometer, from which the source amplitude profile is obtained. This amplitude profile is then matched to a source profile defined by a summation of Gaussian beams as described in Eq. (4.18), which is used to propagate the acoustic waves through the air to the surface of the transducer. An example of a measurement obtained by laser interferometry for a commercial transducer coupled to an aluminum block and excited at 2 MHz is given in Fig. 5.7. The line scan in Fig. 5.7(a) shows excellent agreement of the calibration reference sample surface to the source function described by Eq. (4.18). Therefore the coefficients used to generate this source function can be used in the propagation model in air from the surface of the sample to the surface of the air-coupled transducer.

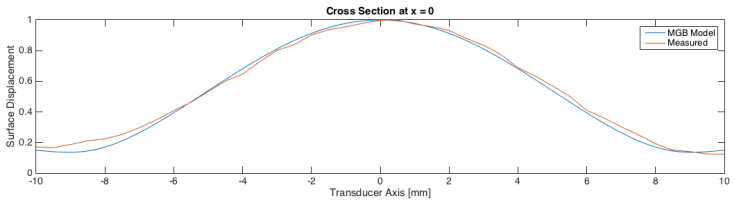

(a)

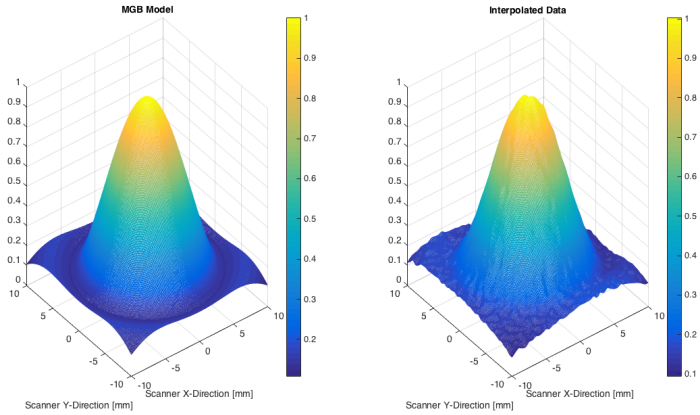

(b)

Figure 5.7: (a) Data taken by laser interferometer [red line] compared to the MGB source model predicted by Eq. (4.18) [blue line] at 2 MHz. (b) Sample surface [right] compared to the modeling output of the source conditions [left] shown on the sample surface for the same measurement conditions as (a).

This process was performed for frequencies between 1 MHz and 6 MHz, and the maximum velocity amplitudes for the source functions at each frequency are shown in Fig. 5.8. This closely mimics the frequency response of the generating contact transducer used to obtain these results, which has a nominal center frequency of 5 MHz, combined with the frequency content of the pulse generated by the pulser/receiver (which is not strictly flat across the bandwidth of the measurement).

5.3.1.2 Propagation modeling through air

In order to propagate the acoustic source through air, the MGB modeling framework discussed in sec. 4.2.2.4 is applied using the source conditions calculated and displayed in Fig. 5.8. The major advantage in this calibration procedure as contrasted to performing the ful field modeling for the fundamental and second harmonic wave fields is that all the

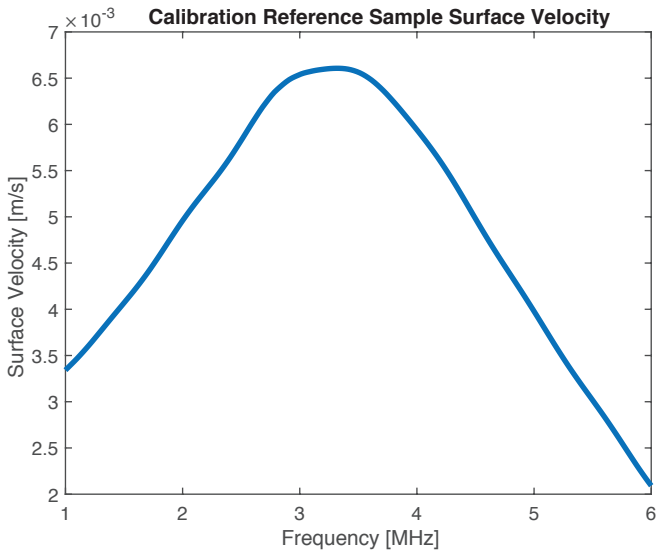

Figure 5.8: Maximum velocity amplitudes for calibration reference sample over the range of frequencies from 1 MHz to 6 MHz, which are then used to propagate acoustic waves through air to the receiver surface.

transmission information we are interested in is contained in the linear portion of the signal. This means that the only propagation equation we need to transmit the source information to the receiver surface is Eq. (4.19), which is reproduced and condensed here for reference.

$$p = \rho_0 c_0 v_0 \left[e^{-\alpha z}\right] \left[\sum_{n=1}^{N} \frac{A_n}{1 - iB_n z/D_R} \exp\left(\frac{B_n (r/a)^2}{1 - iB_n z/D_R}\right)\right] \tag{5.9}$$

The fact that we only require the linear portion of the wavefield greatly reduces the computational load of the calibration versus the SHG optimization procedure. All that remains then is comparing the modeling output at the receiver surface to the measured output voltages from the calibration experiment.

5.3.1.3 Receiver surface and voltage output

As in sec. 4.3.3, modeling the pressure field at the surface is followed by the integration across the receiver face, using Eq. (4.27) reproduced below:

$$F_n(x', y') = 2 \int_A p_n(x, y) \mathrm{d}A \tag{5.10}$$

The quantity $F_n(x', y')$ is the same quantity F^{CALC} that we require for calculation of the transfer function $H(\omega)$ in Eq. 5.8. This is then directly related to the measured voltages from the experimental output of the air-coupled transducer, which matches the values of V^{MEAS} in our desired transfer function. This is the final step in the model based calibration, and the details of how to obtain these quantities experimentally are described in the next section.

5.3.2 Experimental Setup

The experimental setup for the model-based calibration is shown in Fig. 5.6. The calibrated reference sample consists of a Panametrics V109 contact transducer with nominal center frequency of 5 MHz coupled with a light lubricant oil to the bottom side of a 27mm thick solid block of aluminum 2024 T351. This block is highly polished on both sides in order to both facilitate better coupling to the generating transducer and also to obtain a reflective surface for laser interferometric measurements on the opposite face. A polished surface greatly increases the SNR of the laser interferometry measurement, which is important for measuring the small amplitude surface displacements on the aluminum surface. A longitudinal acoustic wave is excited by a Panametrics 5072PR pulser-receiver broadcasting a 900 Vpp broadband pulse to the V109 transducer.

In order to measure the surface displacements of the calibrated reference sample, a Polytec laser interferomter comprised of an OFV-534 head and OFV-5000 controller is used to directly measure the surface displacements of the aluminum face opposite the V109 transducer. A 20 mm x 20 mm area was scanned with 0.5 mm steps using a custom scanning stage, and at each measurement point, 512 signal averages were taken in order to further increase SNR as much as possible. The end result of this laser interferometer scanning measurement was a 2D map of surface displacements at each of the frequencies of interest, shown in the first column of Fig. 5.9.

After the calibration reference sample was characterized, an Ultran NCT4-D13 (nom-

inal 4 MHz center frequency) was scanned in the same manner as the laser interferometer with the same level of input excitation to the generating transducer. At each scan point, the voltage output from the transducer was obtained, providing a 2D map of the measured voltages with the center of the air-coupled transducer aligned at each measurement point with the corresponding location on the laser interferometer map. The results of this scanning operation is shown in the final column of Fig. 5.9. One of the most important aspects of this experimental setup is the proper alignment of the air-coupled transducer. In the longitudinal wave experiments, the transducer must be as close to perfectly normal to the surface as possible because of the high degree of directionality of the air-coupled receiver. The alignment of the transducer can be extremely time consuming, as it must be aligned in the x and y directions simultaneously, and corrective action along one axis can alter the alignment along the other axis.

After receiving the voltage outputs from the air-coupled transducer, they are compared to the calculated force values obtained from the modeling results, and from this comparison the air-coupled transducer transfer function $H(\omega)$ can be determined.

5.3.3 Model-based calibration results

The scan results of the calibration measurement are shown in Fig. 5.9. The figure shows, according to each column, the steps described in the previous sections: the laser scan of the sample surface [left], the modeling of the pressure wave from sample surface to receiver surface [middle], and finally the measured voltages from the air-coupled transducer scanning measurement [right]. There are a few characteristics of the scans that are important to point out, most notably the radial symmetry of the laser interferometer scans of the sample surface, which confirms our modeling assumptions and validates the modeling approach used in this calibration. Additionally, the air-coupled transducer scans show radial symmetry at low frequencies, and somewhat reduced symmetry at higher frequencies. This is due to the difficulty of aligning the air-coupled transducer perfectly, which shows empirically

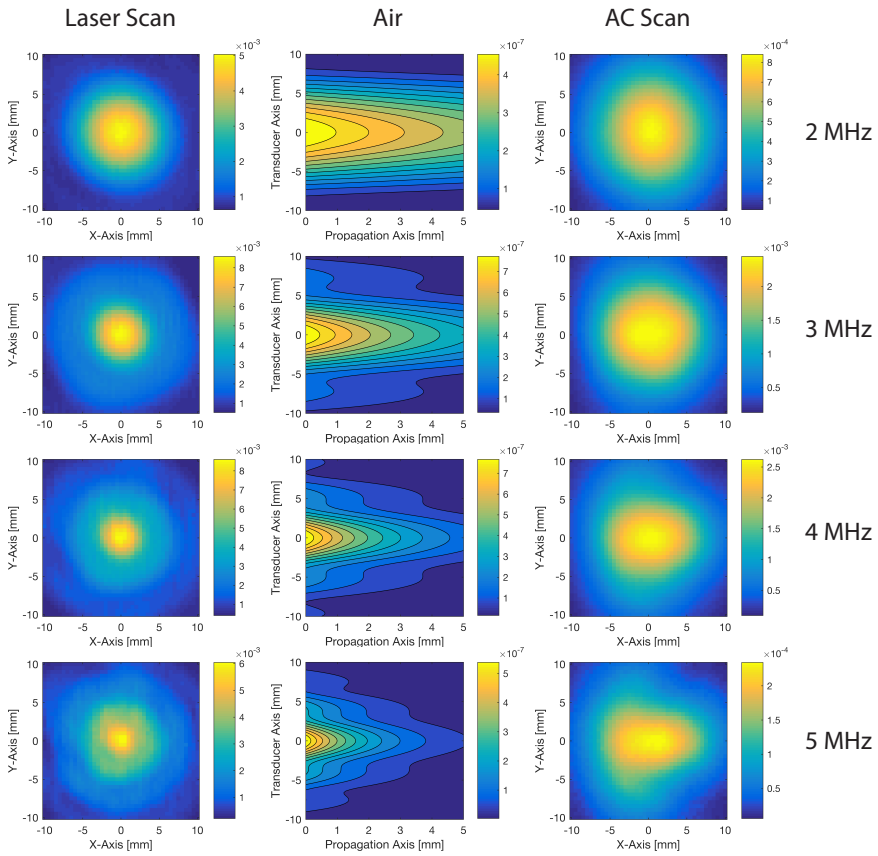

Figure 5.9: Modeling results and measurement scans from a frequency range of 2 to 5 MHz at 1 MHz increments. The first row contains the results from the lowest frequency and the last row contains the results from the highest frequency. The columns illustrate, from left to right, the laser scan of the aluminum calibration specimen surface at the interface between aluminum and air (plan view), the modeled pressure field in the air from sample surface to receiver surface (section view), and the result of the air-coupled transducer scan of the received pressure waves (plan view). The results in this figure highlight the quantitative and qualitative changes in the wave forms as the frequency of the input changes, most notably the decreasing radius of the main lobe in the measured results with increasing frequency.

at higher frequencies because of the increasing directionality of the transducer as frequency increases. This is a characteristic of nearly all air-coupled transducer measurements, which will be seen in the experimental results of the nonlinearity parameter calculations in the following sections. Finally, it is worth noting that measurements above 4 MHz are difficult with the air-coupled transducer regardless of alignment because of the high attenuation of acoustic waves through air at these frequencies and the high insertion loss of the transducer at these high frequency values.

Using the entire frequency range of data similar to that shown in Fig. 5.9, we can construct the calibration curve $H(\omega)$ that we desire for nonlinearity parameter measurements. This curve is shown in Fig. 5.10.

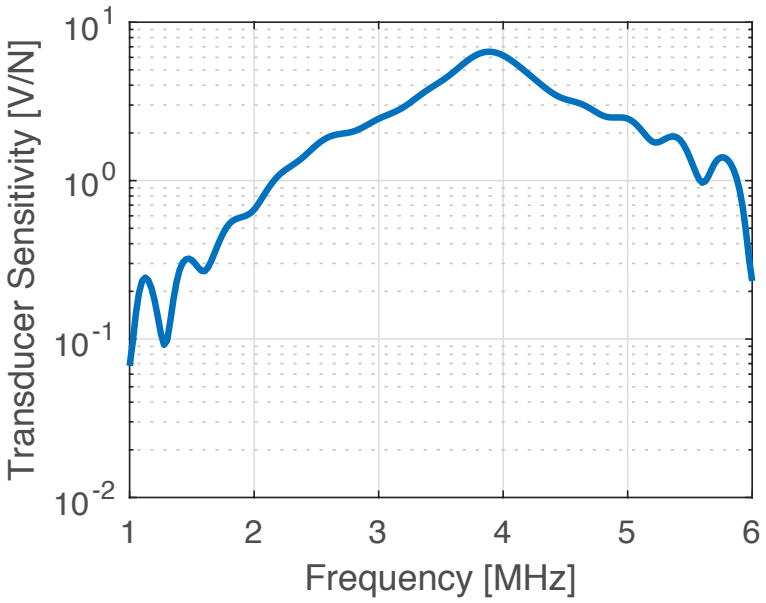

Figure 5.10: Calibration curve for the Ultran NCT4-D13 air-coupled transducer which allows for the conversion from the measured transducer output voltage (V) to the received force on the transducer surface (F) in Newtons.

The calibration curve obtained in these measurements matches the expected results for the Ultran NCT4-D13. The center frequency is around 3.9, which is just below the nominal 4 MHz according to the manufacturer specifications. Additionally, the spurious noise from the self-reciprocity calibration results from Fig. 5.5 are no longer present. This transfer function can now be used along with the modeling and optimization procedure outlined in ch. **??** to calculate absolute nonlinearity parameter values from air-coupled SHG experiments. These experimental results will be discussed in the next chapter.

5.4 Summary

This chapter discussed the motivation for developing a model-based calibration for air-coupled transducers, along with the experimental and computational framework for the

calibration and results of the calibration experiments. The major points of this chapter are listed as follows:

- While self-reciprocity calibrations are useful in many circumstances, they fail to adequately capture the behavior of air-coupled transducers because of attenuation concerns in air and high insertion loss of the transducer.

- A model-based calibration was proposed that would allow for more accurate calibration of air-coupled transducers involving a known calibration reference sample. This sample would provide a known pressure field in air that can be measured by the air-coupled transducer, which would them allow for a direct comparison of measured voltages to a known force on the transducer face.

- The calibration reference sample consists of a contact piezoelectric transducer coupled to a block of aluminum 2024, which was then measured with a laser interferometer on its exposed surface. This measurement was then turned into a summation of Gaussian sources using the MGB source modeling equations previously introduced, allowing for easy propagation of the acoustic wavefield to the receiver surface from modeling.

- The propagation modeling was handled by the MGB modeling equations discussed in the previous chapter, and from this the force at the receiver surface was calculated and compared directly to the measured voltage at the air-coupled receiver output. From this comparison, the transfer function $H(\omega)$ was calculated for use in extracting the absolute nonlinearity parameter β from air-coupled measurements.

CHAPTER 6

ABSOLUTE NONLINEARITY PARAMETER MEASUREMENTS

The primary objective of this research is finding the absolute nonlinearity parameter from measured data using air-coupled piezoelectric receivers. At the beginning of this dissertation, three steps were identified as requirements for calculating the absolute nonlinearity of a material: the characterization of the acoustic source, the determination of the appropriate propagation modeling and integrating that with a nonlinear optimization routine to solve the inverse problem connecting measured data to modeling results, and the characterization of the air-coupled ultrasonic receiver for measurement of absolute ultrasonic quantities. These steps were all discussed in great length in chapters 3, 4, and 5 respectively, and we now have the necessary tools to perform longitudinal and Rayleigh wave experiments for the calculation of β and β_{11}. This chapter will focus on those experiments and present the results of the mixed experimental and optimization solution for extracting the nonlinearity information from metallic samples.

6.1 Longitudinal wave nonlinearity parameter measurements

6.1.1 Experimental setup

The experimental setup for measuring β is shown in Fig. 4.1 and reproduced below for reference.

An Agilent 33250A signal generator generated a toneburst signal of 12 cycles at 2.1 MHz, which was amplified by a Ritec SNAP 5000 high power gated amplifier to 1000 Vpp with a pulse repetition rate of 20 ms. The signal was passed to the generating transducer, which is held in contact with the sample by a toggle clamp and positioned by the test apparatus. The acoustic signal from the piezoelectric source then propagated through the

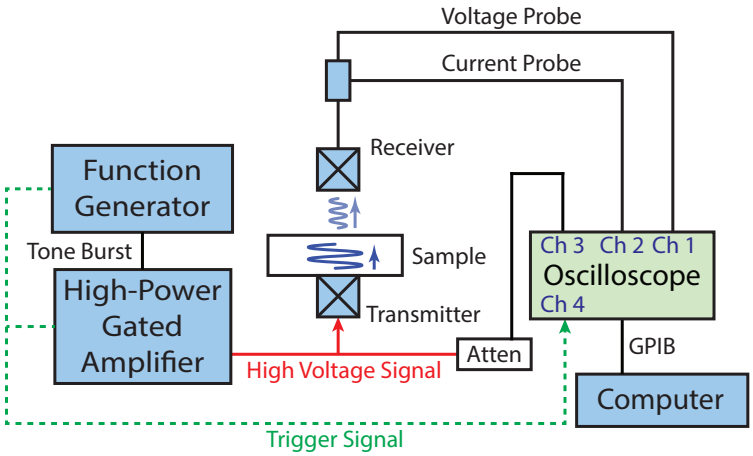

Figure 6.1: Typical longitudinal wave NLU setup for longitudinal SHG measurements. The generating transducer, labeled as "transmitter", is a contact piezoelectric transducer that is held via a clamp to the sample. The receiver is an air-coupled transducer with an air gap separation from the surface of the sample. The propagation field from source to receiver must include the wavefields through both the sample and this air gap in order to provide useful information from air-coupled measurements about the state of the sample surface.

sample and to the sample/air boundary where it transmitted across the interface and arrived at the face of the air-coupled receiver. The receiver was an Ultran NCT4-D13 piezoelectric transducer with a center frequency of 3.9 MHz and diameter of 12.5 mm.

The receiver was attached to a five axis scanning stage and held above the sample with a standoff height of 5 mm. For laser interferometry scans, the air-coupled receiver was replaced with a Polytec LDV which was used for verification measurements of the sample surface displacements. The Polytec model used in this work was the OFV-534 compact optical head in conjunction with an OFV-5000 controller equipped with the DD-300 displacement decoder, which has a flat measurement bandwidth up to 20 MHz.

Two different samples were used in these experiments: a 27 mm thick plate of aluminum 2024, and a 19mm thick specimen of fused silica. Additionally, a different generating transducer was used for each specimen. The aluminum sample was excited by a

Panametrics V106 commercial contact transducer with a nominal center frequency of 2.25 MHz and a half inch diameter. The fused silica sample was excited by a lithium niobate disc with a center frequency of 2 MHz and a half inch diameter. This was done to compare the effects of using a single crystal versus a PZT source on transducer nonlinearity.

While the air-coupled transducer is fairly insensitive to minor surface blemishes on the specimens, the laser LDV is not and requires a mirror-like reflectivity in order to have the SNR required to make second harmonic measurements. In order to make the aluminum sample reflective for use with the Polytec LDV, the surface was polished to a mirror-like finish with a combination of sandpaper grits up to 2000 and finished on a polishing wheel. The fused silica sample was partially covered with an extremely thin piece of aluminum reflective tape to achieve the same effect. The tape was thin enough that it did not contribute its own dynamics to the measurement, but provided an optically reflective surface for measurement.

The experimental data was recorded with a Tektronix TDS 5034B digital oscilloscope combined with a LabView script that timed data collection to scanning stage motion. The collected digital data was then analyzed in MATLAB to extract the relative signal amplitudes from the received waveforms of the air-coupled transducer or LDV output.

6.1.2 Experimental Procedure

The transducer was first applied to the bottom surface of the sample and clamped into place with a toggle clamp in order to ensure that the same clamping force and positioning is applied for each run of the experiment. A light oil was used as a couplant between the transducer and the sample to reduce contact nonlinearities and acoustic reflections.

The next step was to align the air-coupled transducer with respect to the sample surface. A standoff height of 5 mm was chosen between the face of the receiver and the sample as a compromise between signal strength and physical clearance issues through the entire experimental run. After setting the standoff height, the air-coupled transducer was aligned

to the surface normal. The geometric alignment of the air-coupled transducer is by far the most challenging aspect of this measurement and also one of the most critical aspects. A small misalignment will cause noticeable defects in line and surface scans with the air-coupled transducer[19, 72]. For laser interferometry measurements, the process is simpler because the alignment is more forgiving. For a piston-like generating transducer, the scans should be symmetric, and this is one of the best criteria to use when evaluating adjustment impacts and determining future adjustments.

Once the air-coupled transducer was aligned normal to the surface, the total scan in the xy-plane is performed (typically a 20 mm by 20 mm scan with 0.5 mm measurement increments). Each measurement location was time averaged on the oscilloscope over 512 cycles to improve SNR. After the data was acquired, it was then processed in MATLAB.

6.1.3 Data Processing

After the data was collected, the MATLAB FFT algorithm was used to obtain the fundamental and second harmonic frequency components of the signal. In measurements of relative signal amplitudes used to calculate measured of β^*, a Hann window is applied in the time domain to reduce the effects of amplifier and transducer transients. However, when the goal is to obtain amplitude-accurate signal components for the purpose of absolute nonlinearity measurements, the difficulty in correcting for amplitude and phase distortion of the signal is necessary. Once the signal amplitudes were extracted at the frequencies of interest, the transducer calibration determined in ch. 5 was applied to convert the values from electrical voltage to mechanical force.

The nonlinear least-squares curve fitting algorithm from ch. 4 was then used to extract the modeling parameters according to Eq. (4.39). The fundamental signal component was fit first using the framework outlined in section 4.4.2 in order to extract the values of p_0 and α_1. These values were then used as inputs to Eq. (4.39) in the fitting process for the second harmonic data, from which β was extracted. Because this data was taken with the

calibrated air-coupled ultrasonic receiver, the values of β obtained from this process were the absolute nonlinearity parameters we hoped to find.

6.1.4 Longitudinal wave results and discussion

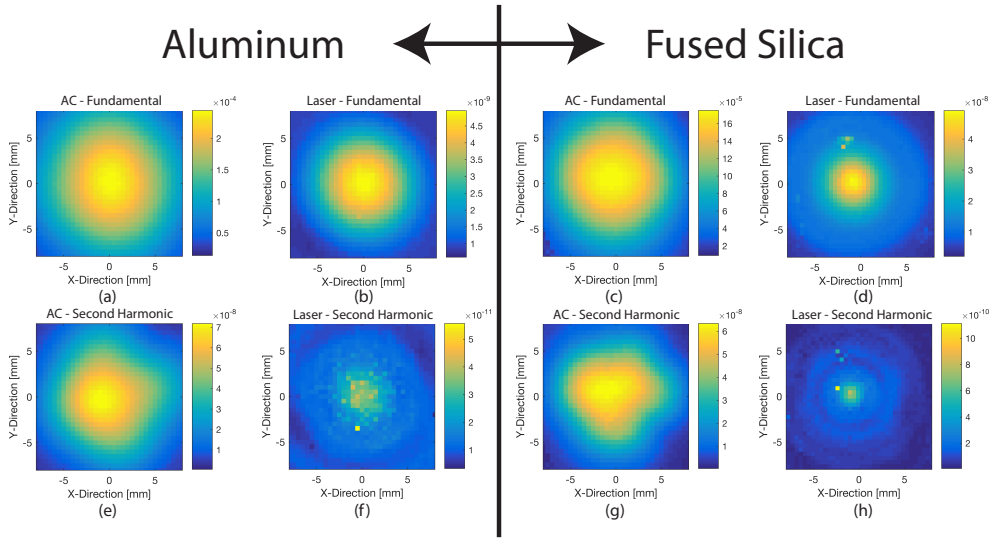

Figure 6.2: Air-coupled transducer and laser interferometer scan results of aluminum and fused silica specimens. The aluminum fundamental (a) and second harmonic results (e) show strong radial symmetry characteristic of an accurate alignment of the air-coupled receiver. This is highlighted by the similarity to the laser interferometer scan results shown in (b) and (f). The air-coupled measurements in fused silica at the fundamental (c) and second harmonic (g) frequencies show more asymmetry in the second harmonic measurement as contrasted to the laser interferometer measurements in (d) and (h), indicating that improvements can be made to the air-coupled receiver alignment. These air-coupled measurements demonstrate what the air-coupled receiver "sees" when it area-weights the pressure field in air at each scan location.

Air-coupled transducer and laser interferometer scanning measurement results are shown for the aluminum and fused silica samples in Fig. 6.2. Figure 6.2(a) and (e) show the fundamental and second harmonic scan results respectively measured by the air-coupled transducer from the aluminum specimen, while (b) and (f) show the laser interferometer surface scans from the same sample. The fundamental and second harmonic measurements in fused silica by the air-coupled transducer are shown in (c) and (g) respectively , with the corresponding laser interferometer measurements shown in (d) and (h). A few key features

of the measurement are highlighted nicely in these images. First is the impact of alignment of the air-coupled transducer to the sample surface. In (a) and (e), the scan results are approximately radially symmetric, which is predicted by the modeling equations and shown to be empirically true on the sample surface by the laser interferometer scans in (b) and (f). This radial symmetry of the air-coupled transducer scan result indicates that the tilt of the transducer relative to the sample surface is well calibrated in both scan directions. In the fused silica scans shown in (c) and particularly in (g), the measurement result is slightly asymmetric. It is likely that the sample and the air-coupled transducer are misaligned along one or both axes, which is indicated by the comparison to the laser scans of (d) and (h) which show that the waveform at the surface of the sample is indeed radially symmetric. However, the use of the full-field measurement in the optimization process helps to reduce the impact of small misalignment such as in Fig. 6.2(g).

Another observable effect from Fig. 6.2 is that the second harmonic measurement is much more directional and has a narrower main lobe than the fundamental measurement. This is a predictable result[73], but has experimental implications. Any misalignments are going to impact the second harmonic measurement more than the fundamental measurement for this reason. When performing the receiver alignment, generally there are two conditions that one must satisfy simultaneously. The first is that scans through the measurement center along the x and y axes are symmetric about the middle, and second is that the x and y scans are maximized at the same point (which becomes the measurement center). If both of these conditions are met, then the result will be a clean scan and increased accuracy of the data processing and extraction of β.

After processing the data according to the algorithm outlined in section 4.4.2, the resulting curves and matching laser interferometry measurements are shown in Fig. 6.3. Figures 6.3(a) and (b) show the results for the fundamental and second harmonic signals respectively from the aluminum specimen and (c) and (d) show the fundamental and second harmonic signal respectively from the fused silica specimen. Laser interferometry mea-

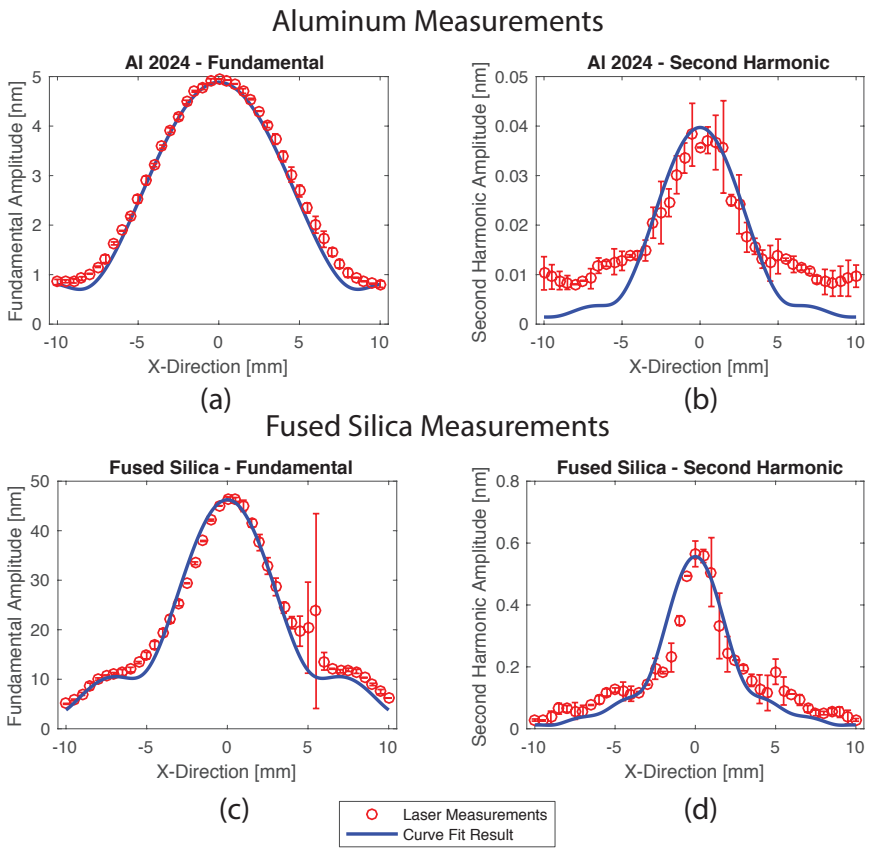

Figure 6.3: Results of the nonlinear curve-fitting operation in aluminum and fused silica. The aluminum fundamental results (a) show very close alignment between the measured (red circle with error bars) and curve-fit (blue solid line) results, while the second harmonic (b) demonstrates very accurate results in the main lobe but differences in the side lobe amplitudes. The fused silica fundamental (c) is similarly accurate, while the second harmonic results (d) look much more like the modeling picture. The high variation in the fused silica data around the 5 mm measurement point is due to surface defects in the reflective tape used to make the laser interferometer measurement.

surements are notoriously difficult for use in obtaining second harmonic amplitudes[35], one reason being the large error in measurements where the surface is imperfect in some way. This is clearly visible in figures 6.3(c) and (d) around 5 mm on the x axis of the plot from the large experimental error relative to the other measurement locations. While this is an important consideration, the relatively low error in the rest of the data points demonstrates sufficient surface quality for second harmonic measurements.

The fundamental aluminum results in Fig. 6.3(a) show very strong agreement with the interferometric measurements, as do the fundamental fused silica results in (c). The sec-

ond harmonic aluminum results show strong agreement in the center of the measurement, but the side lobe information begins to deviate from the curve-fitting output. One reason for this could be the presence of generating transducer nonlinearity introduced from the Panametrics commercial source. The transmitter in the modeling proposed in this work is assumed to be a linear, piston-like source, such that a monochromatic input will lead to a monochromatic output. In reality, the generating transducer may also operate in a weakly nonlinear fashion, creating an additional propagating acoustic wave through the sample at the second harmonic frequency that propagates as a fundamental as in Eq. (4.19), referred to as the source nonlinearity[20]. This nonlinearity from the transducer can affect the measured second harmonic signal both in amplitude and in spatial distribution because the diffraction pattern of a fundamentally propagating wave displays a wider main lobe and more pronounced side lobe characteristics. This would explain the presence of the side lobe information in Fig. 6.3(b). Commercial transducers such as the one used in measuring the aluminum sample tend to have a higher source nonlinearity than single crystal piezoelectric disc sources, such as the $\mathrm{LiNbO_3}$ disc used with the fused silica sample[2]. This assertion is strongly supported by the strong agreement of experimental results from the more linear source shown in Fig. 6.3(d) which does not display the variance between the measured side lobe information from the laser and air-coupled transducer.

Furthermore, a material with a higher nonlinearity such as fused silica, the generated material nonlinearity would more significantly overshadow the transducer nonlinearity. This would further justify the second harmonic results from the fused silica sample in Fig. 6.3(d) showing stronger agreement with the measured values than the aluminum sample in Fig. 6.3(b) given the presence of the transducer nonlinearity.

In the fused silica second harmonic results, the modeling shows strong correlation with measured values around the main lobe, and is more accurate regarding the side lobe predictions than in the aluminum sample as discussed previously. In particular, the geometric features of the curve-fit result match the features of the measured data, specifically the

shapes and locations of the side lobes. The locations of these side lobes are related to the apparent radius of the generating transducer in the model, and hand-tuning this quantity can have the effect of matching these geometric features even more closely.

In order to calculate the acoustic nonlinearity parameter, the optimization algorithm discussed in Sec. 4.4.2 requires the calculation of the other fitting parameters along with β. These parameters (p_0, α_1, α_2) are listed in table 6.1.

Table 6.1: Optimization variables for aluminum and fused silica specimens as a result of the process outlined in Sec. 4.4.2

Material	$p_0\,(Pa)$	$\alpha_1\,(Np/m)$	$\alpha_2\,(Np/m)$
Al 2024	9.57e5	2.3e-3	8.1e-3
Fused Silica	4.12e5	6.9e-3	1.4e-2

An important observation that can be made from the modeling parameters obtained from the optimization algorithm is that the attenuation coefficients are extremely small in both aluminum and air. This results in nearly negligible attenuation corrections in the modeling. This conclusion aligns with expectations for frequencies below 10 MHz, where very low magnitude attenuation coefficients in similar metallic and fused silica specimens have been reported[2, 6].

The major outcome of the optimization procedure is the value of the acoustic nonlinearity parameter β obtained from the model-based fitting of the experimental data. The use of the $\mathrm{LiNbO_3}$ disc for generation of the input wave clearly reduces the source nonlinearity as can be seen in Fig. 6.3(d), which instills confidence in the optimization to calculate an accurate measure of β. The reported results in fused silica range from 9.7 to 14[24, 31, 35, 103], thus the measured β in this work of $12.1 \pm .5$ is in excellent agreement with literature values. Fused silica is very well studied in longitudinal NLU measurements, so agreement with literature values is a strong verification that the methods presented in this work provide accurate β estimates.

Values of β in aluminum from literature span a variety of heat treatments and thus have a large range of reported values from 4 to 12[24, 104, 105]. That being said, the measured

value of β in this work of 5.0 ± 0.3, while falling in this range, is not a fully reliable estimate of the acoustic nonlinearity in the aluminum sample. The impact of source nonlinearity from the commercial transducer discussed earlier must be modeled more extensively or removed entirely through the use of an alternate source. Doing this will ensure that the measured second harmonic waveform is due primarily to second harmonic generation in the material and not from the measurement hardware. Electrical effects have thus far prevented the use of an $LiNbO_3$ disc (as in fused silica) with metallic samples to remedy this issue.

One final important consideration when using this approach is that the value of the nonlinearity parameter in some materials is known to be negative, producing a second harmonic out of phase with the fundamental wave form such as in fused silica[48]. This method obtains the magnitude of the nonlinearity parameter but does not obtain the phase relationship, and thus the result is the absolute value of the acoustic nonlinearity parameter for the material under test.

6.2 Rayleigh wave nonlinearity parameter measurements

6.2.1 Experimental setup and procedure

The air-coupled transducer measurements were obtained with the setup depicted in figure 2.4. The generating system was an acrylic wedge coupled with an ultrasonic generating transducer (Panametrics V-type, center frequency of 2.25 MHz and 12.5mm diameter) as described in sec. 3.2.1.2, excited by an Agilent 33250A signal generator amplified by a RITEC GA-2500A RF Amplifier. The input pulse shape was again a 2.1 MHz sine wave modulated by a rectangular window of 20 cycles with a pulse repetition rate of 20 ms. The receiver was an Ultran NCT4-D13 12.5mm diameter air-coupled transducer, amplified by a factor of 40 dB by the pulser/receiver and held at a distance of 3.5mm from the surface of the specimen under test.

Propagation distances for this experiment were chosen between x_{min} = 30 mm and x_{max} = 78 mm, with the starting distance chosen primarily because of restrictions from the size

of the air-coupled transducer and the assembly that houses it. Two millimeter step sizes provided adequate spatial resolution to see the major observable effects while maintaining a reasonable measurement time. The measurements were conducted first by calibrating the lateral position and angle and of the main lobe at the fundamental frequency and then the scans were performed by manually adjusting the x-y position of the air-coupled transducer to maintain this line. This is very important for repeatability of the results[19, 72].

The air-coupled transducer was scanned along this centerline at a constant standoff height of 3.5 mm from the surface at an angle of approximately 6.5 degrees for the aluminum sample. Because the physical principle behind air-coupled transducer detection of the out-of-plane displacement of the Rayleigh wave is the leakage of energy from the surface of the specimen into the air, it must be positioned in alignment with the direction of propagation of the leaked longitudinal waves through the air. According to the predictions and theory developed by Deighton et al[71] and Snell's Law, the predicted direction of propagation of the leaked waves is at an angle Θ_R relative to the surface of the sample, where

$$\Theta_R = \sin^{-1}\left(\frac{c_{air}}{c_R}\right) \tag{6.1}$$

This out of plane displacement was then related back to the definition of the Rayleigh displacement by the relationship established by equation (2.9).

The air-coupled transducer has a nominal center frequency of 4 MHz and an actual center frequency of 3.9 MHz. The second harmonic in this measurement system (at 4.2 MHz) falls within the bandwidth of the transducer. Amplification and averaging over 256 cycles resulted in an SNR of 54 dB for these measurements, which is enough to resolve the second harmonic data adequately. This data was recorded on the Tektronix oscilloscope and imported into MATLAB for data processing.

6.2.2 Data processing

The data processing conducted on the measurements follows the process diagram shown in figure 4.16. First the data is Hann windowed and processed with an FFT algorithm to provide the amplitudes of the harmonic components. Following this process, the fundamental frequency amplitude over propagation distance is fit to equation (2.13) using the nonlinear least squares method described in equation (4.39). From this we obtained values for $v_{0,1}$ and α_1, which propagate throughout the procedure.

When the second harmonic data is examined, there tends to be a "linear" region, where the data looks to more or less follow a linearly increasing trend. This region extends for an arbitrary number of data points depending on the material and measurement conditions and is difficult to consistently and accurately define. However, the current method relies on only a first order approximation of the source strength, which in this case is the y-intercept of the second harmonic amplitude data, and for this purpose, the first 5-10 data points served to provide the initial fitting condition for $v_{0,2}$.

Finally, the data is fit to equation (2.14) with the fitting variables $v_{0,2}$, α_2, and β_{11}. The initial guess value for α_2 is $16\alpha_1$ based on thermoviscous attenuation predictions of the form $\alpha_n = n^4\alpha_1$[45, 106], however the final value tends to change dramatically from the guessed value and is one of the most sensitive parameters in the fitting process. From this final curve-fit, the value of β_{11} is calculated and extracted.

In the case where the air-coupled receiver is calibrated using the procedure in ch. 5, all of the received values would be absolute and thus the extracted value of β_{11} would be absolute. However, the calibration of the air-coupled transducer is a calibration between the force on the transducer surface and the received voltage, which means that in order to use this calibration effectively a modeling step comparing the surface displacements to the pressure field in the air is required. The use of the RSI modeling framework in conjunction with the transducer calibration enables the extraction of absolute nonlinearity parameters from air-coupled transducer measurements.

6.2.3 Rayleigh wave results and discussion

The results of the Rayleigh wave nonlinearity parameter measurements are divided into two section: relative measurements based on reference or virgin samples followed by a discussion of the conversion of these relative measurements into absolute measurements using the transducer calibration.

6.2.3.1 Relative nonlinearity parameter measurements

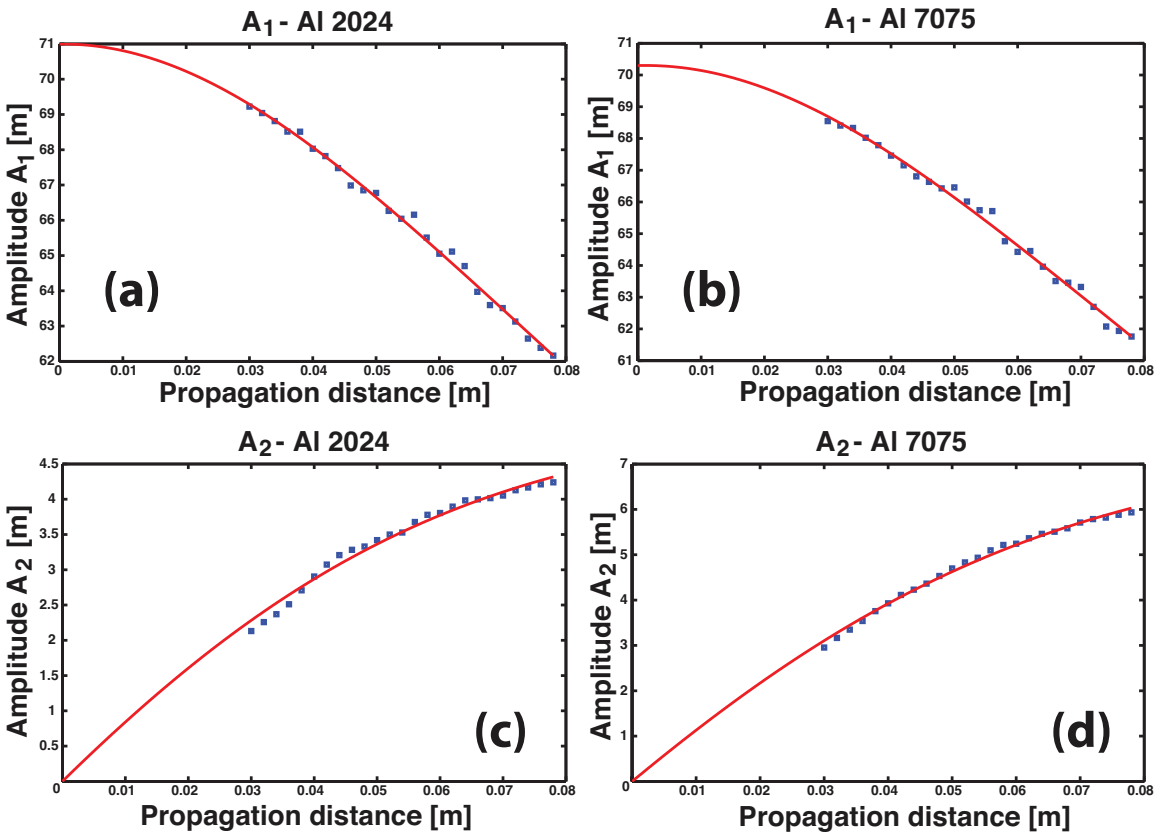

Figure 6.4: Nonlinear ultrasound testing results for the Al 2024 and 7075 samples. (a) and (b) show the fundamental amplitudes for the 2024 and 7075 specimens respectively. (c) and (d) show the second harmonic amplitudes for the 2024 and 7075 specimens respectively. Data points and best-fit lines from the optimization process outlined in figure 4.16 are shown for each case

The results of the aluminum 2024-T351 and 7075-T651 plate measurements[19] are shown in figure 6.4. In these figures, the fundamental components (a and b) and the second

harmonic components (c and d) of the received signals in Al 2024 and 7075 respectively are shown along with the results of the curve-fitting process. When interpreting these figures, it is again important to understand that fitting the values of parameters that exclusively affect the amplitude of the data will produce numerical results that are relative to transfer functions of the measurement equipment. Therefore, without precise calibration of these transfer functions, the numerical results must either be normalized or compared across specimens making sure that the source strength $v_{0,1}$ is comparable in value (which should be the case for consistent measurements regardless). In this case, the curve-fit value of $v_{0,1}$ was 9.368×10^8 [a.u.] for Al 2024 and 9.267×10^8 [a.u.] for Al 7075, which is a 1.08 % difference between the two. This means that the relative amplitudes between the two methods can be compared with confidence. Eventually, we will want to apply the air-coupled transducer calibration to these results to provide absolute values of $beta_{11}$ and avoid requiring relative comparisons at all.

The shapes of the figures are defined by their generation and decay rates, and are thus dependent on the terms inside the exponential, radical, and error functions of Eqs. (2.13) and (2.14). The relationships between the effects these terms have on the shape of the data versus scaling effects are quite complicated, which makes them very sensitive to change during the curve-fitting process. While the source strength values tend to converge very quickly, the terms that affect the shape of the data change dramatically and have a stronger influence on the quality of the fit. That being said, one of the great strengths of this curve-fitting procedure is that all of these considerations are taken care of simultaneously and automatically, and the process is repeatable and stable.

In figure 6.4(c) and (d), a noticeable oscillation of the data points about the prediction curve exists due to the kinematics of the manual positioning stages as they are adjusted between measurements. While these effects are worth mentioning because they appear consistently in the data sets, they do not heavily influence the results of the curve-fitting procedure.

From the process used to generate the results in Fig. 6.4, the calculated values of β_{11} are shown in Tab. 6.2 along with results from comparable works[19, 104, 105]

Table 6.2: Literature and current work data for nonlinearity parameter in comparable Al specimens

Data Source	Materials	$\beta_{11}^{7075}/\beta_{11}^{2024}$ (max - min)
Yost et al[105]	Al 7075 Al 2024	1.865 (2.03 - 1.70)
Li et al[104]	Al 7075-T551 Al 2024-T4	1.125 (1.28 - 0.97)
Thiele et al[19]	Al 7075-T651 Al 2024-T351	1.675 (1.85 - 1.50)
Current work	Al 7075-T651 Al 2024-T351	1.363 (1.52 - 1.25)

These results compare favorably to those found in literature, although it is important to note that the literature values in the cases of Yost et al[105] and Li et al[104] are for specimens of aluminum that have undergone different heat treatments and are of different chemical compositions from those tested in Thiele et al[19] and the current work. However, the fact that the current work falls within the ranges obtained by the other authors speaks to the accuracy of the proposed method for the calculation of the nonlinearity parameter.

Further results are obtained from a data set borrowed from Ruiz et al[6] in which heat treatment of a duplex steel sample (2205 stainless) was performed and nonlinear ultrasonic measurements taken with a contact transducer and wedge (identical to the one shown in Fig. 2.4 as a receiver. This method of measuring the nonlinearity parameter is inherently less precise than methods using air-coupled transducers because of the additional interfaces between the receiving wedge to the specimen and the receiving transducer to the receiving wedge. In cases like these where the variation of the data is large, guessing which points define the "linear region" of the data is highly prone to subjectivity, and avoiding this step makes results more reliable and repeatable.

By looking at the results of Fig. 6.5(a), the difference in the fitting of the calculated ratios of A_2/A_1^2 at 24 hours of heat treatment between the linear and nonlinear fitting meth-

ods is clearly shown both quantitatively and qualitatively. The process used to calculate the linear fit is difficult to automate or standardize because the metrics that are typically used to deduce goodness-of-fit, such as an R-squared value, can often be misleading. If the linear fit is conducted over the entire data region, then the R-squared value would, in this case, be higher than in all other data ranges. However, this fit clearly does not follow the qualitative trend of the data and will become much worse with longer propagation distances in addition to demonstrating poorer accuracy in shorter propagation ranges. A linear fit to the first n data points that collectively define the "linear region" will be much more accurate in short propagation ranges but will rapidly lose accuracy in the far field. This effect is primarily due to the smaller contributions of attenuation and diffraction with small propagation distances. Because standard goodness-of-fit metrics are hard to apply, the most easily conducted method of determining the "linear region" is therefor by inspection, which has obvious subjective disadvantages rooted in human error. The quantitative disadvantages, however, become glaringly obvious in Fig. 6.5(a) at the propagation distance of 100 mm, where the linear fit no longer passes through the error bars of the measured data.

The question of repeatability, consistency, and accurate accounting of acoustic considerations in the far field versus short range accuracy before attenuation and diffraction begin to dominate is answered by the nonlinear fitting method in this work, the results of which are shown as the black dash-dotted line in Fig. 6.5(a). The nonlinear fit clearly shows strong accuracy to the measured data points as well as the ability to accurately reflect the trend of the data as it enters the far field. At all points in the measurement region, the nonlinear fit passes through the error bars of the data. These advantages are present in all of the measurements conducted on every specimen in the 2205 duplex stainless steel data set, and because the subjectivity of the linear fitting method is removed, the results are repeatable as well.

The calculated β_{11} values from both the linear (Ruiz data) and nonlinear (current work) methods are shown in Fig. 6.5(b). The agreement of the general trends between the data sets

confirms that the nonlinear fitting method of extracting the nonlinearity parameter produces results that are comparable to those found in the earlier work. Additionally, one source of confusion with the results obtained from the linear fitting technique was the rise of the nonlinear parameter value at 24 hours, labeled (**) on Fig. 6.5(b), back to the heat treatment levels obtained at 10 minutes, labeled (*) on Fig. 6.5(b), of treatment time. This trend was not observed in other material tests[7, 18, 107], and the nonlinear fitting method proposed in the current work shows results more in line with those expected from experience and literature[107]. The accuracy and repeatability of the nonlinear fitting approach combined with the more realistic measures of β_{11} show the strengths of this procedure for calculating material nonlinearity.

6.2.3.2 Absolute nonlinearity parameter measurements

In order to convert the relative absolute nonlinearity parameter results presented in the previous section into absolute material nonlinearity results using the transducer calibration, a few more steps are required than are necessary for the relative measurements. The relative measurements are predicated on the idea that the propagation of the surface wave through the air to the face of the receiver is a process affected equally at all measurement points by the affects of diffraction and attenuation, which is generally true. What this means is that the received voltages at the air-coupled transducer face can be compared across specimens and treatments as long as the baseline measurement is conducted with the same equipment and in the same fashion as later measurements. Absolute measurements are harder to make because this assumption is no longer valid, and much more must be known about the setup and the propagation of the leaked pressure waves to draw valid conclusions from the optimization algorithm.

Instead of using only Eqs. (4.28) and (4.29) in the nonlinear optimization routine depicted in Fig. 4.16, these equations must be used in conjunction with the propagation of the leaked waves through the air according to the modeling discussed in Sec. 4.3.2.2. This

means that another set of equations is involved in the optimization which increases the complexity of the optimization routine significantly.

The difference in the computational effort required for the modeling of the pressure on the surface of the transducer is evident in the fact that, for the relative nonlinearity optimization, each iteration of the optimization required the solution of just one analytical equation, whereas for the absolute nonlinearity optimization, every iteration of the optimization procedure requires the solution of a quadruple integral over the surface and receiver domains. In order for the RSI modeling to be accurate, the domain size of the discrete point sources on the surface and reciever must be at least one tenth the size of the wavelength of the pressure wave in the material. For an aluminum sample at 2.1 MHz with a Rayleigh wave speed $c_R = 2865$ m/s, the wavelength of the Rayleigh wave is $\lambda_R = 3$ mm. This means that an element must be at least 0.3 mm in width, and for a common measurement length of 70 mm, this means that there are 2.3×10^5 elements in the propagation axis. For a field measurement, this means that, at a minimum, a 12mm width along the transducer axis is required resulting in another 4×10^4 elements, totaling 9.2×10^9 point sources *just for the sample surface domain* in the RSI integral, which accounts for two of the numerical integrations required out of the four total. The computation resources required to solve this problem are immense, and beyond the scope of the capabilities in our lab environment. One computation of the RSI integral for this problem given the computation resources available at the time of this work would require between 5 hours and upwards of one day.

Given the nature of nonlinear optimization algorithms, the RSI integral for the Rayleigh wave problem must be solved on average between $n \times 10^0$ and $n \times 10^1$ times, where n represents some scalar value. This means that an optimistic estimate of the amount of time required to solve the inverse problem for the calculation of absolute material nonlinearity would be multiple days, and likely the optimization would require several weeks not accounting for memory allocation issues with most lab computers. It is for this reason that this solution framework was not feasible to solve given the computational resources of the

laboratory at the time of this work.

That being said, the framework *is* ready to implement and the data is available for the optimization routine once the issue of computational resources is solved.

6.3 Summary

This chapter discussed the results of nonlinearity parameter measurements for longitudinal and Rayleigh wave experimental setups, presenting absolute nonlinearity parameter results for the longitudinal wave case and relative measurement results for Rayleigh wave experiments. The major points of this chapter are listed as follows:

- The longitudinal wave experiment yielded a measured absolute nonlinearity parameter value of 5.0 ± 0.3 in aluminum 2024, which matches the values reported in literature for similar samples between 4 and 12. Fused silica measurements yielded a β of 12.1 ± 0.5, which matched the literature values between 9.7 and 14 for similar specimens.

- The effects of different source types were explored and discussed based on the nonlinear signal components in the aluminum and fused silica measurement cases, and the results indicate that the LiNbO3 discs were a more spectrally pure source and thus provide more accurate absolute acoustic nonlinearity measurement results.

- The Rayleigh wave experiments were conducted on aluminum 2024 samples with the contact transdcuer/wedge assembly as the source and air-coupled transducer as receiver, and relative β_{11} parameters were found that agreed with literature values. Additionally, a measurement conducted in 2205 stainless steel was corrected for attenuation and diffraction effects using the optimization framework discussed in this work, leading to a corrected trend that more accurately describes similar trends observed in literature for the evolution of the nonlinearity parameter of the material over a heat treatment regiment.

- Limitations from computational resources prevented the application of the transducer calibration to the relative measurements in order to obtain absolute nonlinearity parameter results because of the massive computational load over the measurement domain from the RSI integral.

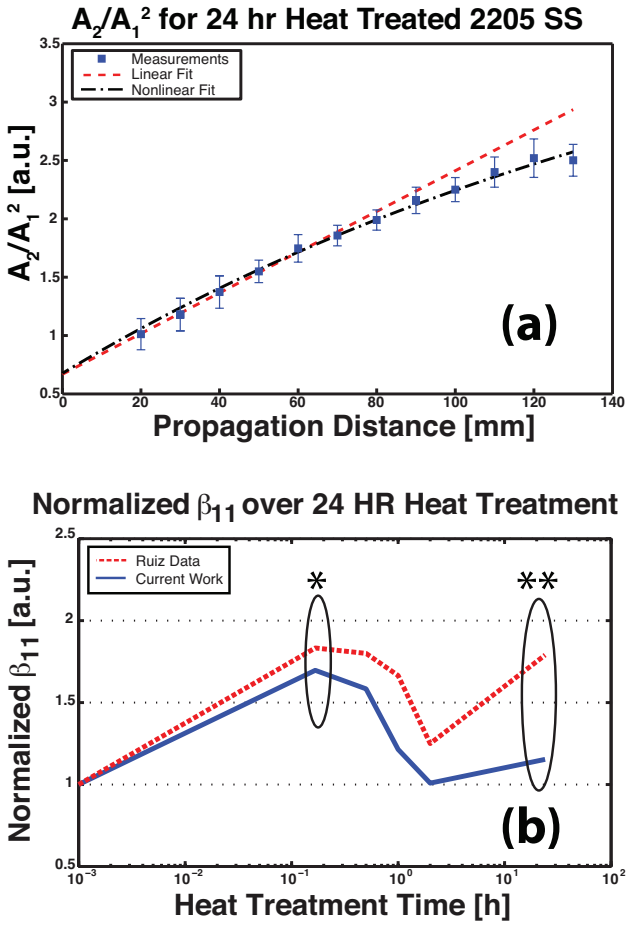

Figure 6.5: (a) shows a set of nonlinear measurements versus propagation distance for a 2205 SS sample heat treated over 24 hours. The red dotted line shows a linear fit to the "linear region" of the data, which is identified subjectively. The black dash-dotted line represents the results of the nonlinear fitting procedure. (b) shows the results of 2205 duplex stainless steel nonlinear parameter measurements as a function of heat treatment time for both the original analysis using a linear fitting approach (Ruiz et al) and the nonlinear fitting approach (current work). The data point labeled (*) represents data collected at 10 minutes, and the data point labeled (**) represents data collected at 24 hours. The β_{11} values represented by each fitting procedure in (a) can clearly be seen as the last data point in (b).

CHAPTER 7
CONCLUSIONS AND FUTURE WORK

7.1 Summary of Results

In this thesis, the second harmonic generation nonlinear ultrasonic technique was used to measure the nonlinearity parameter β of various materials using air-coupled piezoelectric receivers. There are many experimental and modeling frameworks from which material nonlinearity can be determined, two of which are longitudinal wave and Rayleigh wave measurements. Regardless of the physics involved, the determination of absolute material nonlinearity with air-coupled receivers requires three majors steps: The determination of the source profile and behavior, the propagation modeling from source to receiver, and the characterization of the air-coupled transducer in terms of frequency response.

For longitudinal wave experimental measurements, we outlined a modeling framework that allows for accurate calculation of the pressure field from the fundamental and second harmonic wave fields resulting from propagation through both a sample under test and the air column between the sample and the air-coupled receiver. These models account for attenuation and diffraction of the waves as they propagate through the combined stack of materials, and accounts for the various field components as they propagate across interfaces between these materials. By generating a new set of coefficients at each material interface, it is possible to extend this framework through any number of materials over any distance as long as there are sufficient computational resources to complete the calculations. The use of MGB modeling makes this much more efficient than the use of a direct solution such as an RSI model, Which is very important for the extraction of β from measured data because of the iterative nature of the process.

In addition to proposing a modeling framework for pressure field calculation, a method

for calibration air-coupled transducers is employed that circumvents the issues found with using self-reciprocity calibration methods as is standard for use with contact piezoelectric transducers. This calibration method employs the use of a calibration sample and the modeling framework proposed in this work, and was shown to produce results that are in agreement with those expected of resonant piezoelectric, narrow-band devices. A sample calibration curve confirms the resonance of the 4 MHz transducers to be closer to 3.9 MHz, which aligns with its observed behavior.

The modeling framework proposed in this work was used in a nonlinear optimization algorithm employing a least-squares curve-fitting technique which allows for the extraction of the absolute nonlinearity parameter β when combined with the air-coupled transducer calibration. This method was demonstrated by measuring β for two materials: aluminum 2024 and fused silica. The measured β value in the aluminum sample agrees with literature values but includes significant contributions from other sources of nonlinearity, and the measured β value in fused silica agrees with literature values in a strongly convincing fashion because of the low source nonlinearity of the lithium niobate transmitter. The agreement with the extracted values of β from the methods proposed in this work with those found in literature, particularly in the case of the fused silica result, validates the use of this framework for using air-coupled transducers to determine the absolute nonlinearity parameter in a non-contact environment.

The Rayleigh wave experimental setup required a very similar set of steps to those of the longitudinal wave setup, with a few notable differences. First, the acoustic source is not modeled as a piston because of the contact transducer/wedge assembly used to generate the surface waves. Instead it was determined that a Gaussian line source approximation is more appropriate for the generation of a Rayleigh wave, which yields physically accurate values for a relative measure of the nonlinearity parameter. This relative β_{11} can be extracted by fitting the data to models accounting for diffraction, attenuation and transducer nonlinearity effects. By showing that the source function, which is a result of the wedge and transducer

combination, can be accurately described as Gaussian in shape, we validate the use of this approach. Furthermore, the experiments show that there exists a second harmonic component to the source function prior to generation effects which exists because of the numerous contact interfaces and initial propagation of the acoustic wave through the wedge material. This initial second harmonic component was also Gaussian in shape, and this effect must be accounted for in the modeling and data processing. In order to fit the data taken from the air-coupled transducer setup to the proposed model, the use of a nonlinear least squares curve-fitting procedure is again necessary because many of the parameters required for the fit process are either difficult to measure or directly immeasurable. This process is done over multiple steps, the first fitting the fundamental frequency data, the second estimating the nonlinear source strength, and the third fitting the second harmonic attenuation and the nonlinear parameter, which is the ultimate desired result. This process is shown for Al 2024 and 7075 samples, and the results are consistent with previous literature and physical expectations. Additionally, a borrowed data set for heat-treated 2205 duplex stainless steel is re-processed with the updated analytical model and it is found that the new values for the nonlinear parameter both match with the general trends from the previous results and amend them to agree with past literature and physical expectations of the treatment process.

Finally, implementation of the necessary framework for converting the relative measurements to absolute measurement using the air-coupled transducer characterization was discussed, but the practical limitations of the RSI modeling framework prevented this from being feasible given the available resources at this time. However, the complete modeling picture is available and the process is fully realizable given the structure provided in this thesis, and is therefore available as a proof of concept when the necessary computational resources are available.

7.2 Recommendations for future work

Given that most of this work is experimental in nature, there are many aspects of the experimental portion of the measurement that can be improved, such as the automation of the alignment of the air-coupled transducer to the sample surface. As of now, the hand-tuning process is very labor intensive and fickle, and often the success of the alignment can take several hours to accomplish. This is due to the fact that each axis must be tuned individually, but the alignment of one axis is dependent on the alignment of the other axis, particularly for longitudinal wave measurements. By automating this process through the use of some optimization procedure such a conjugate gradients approach to rapidly converge on the proper air-coupled transducer orientation, this can be made into a relatively simple procedure. Doing this would require the mechanization of the rotation stages and height adjustment for CNC control.

Additionally, the disagreement between aspects of the modeled and measured longitudinal wave fields can be attributed to a variety of possible reasons which are worth exploring in further detail. It was shown that, for the Rayleigh wave transducer/wedge source, the generating transducer can introduce a generated transducer nonlinearity which acts as a fundamentally propagating wave (e.g. monotonically decreasing) at the second harmonic frequency of 2ω. The presence of this wave field component would explain the increased side lobe presence in aluminum longitudinal line scan results, as those side lobes match the results of a linearly propagating field components. The relative strengths of the transducer generated nonlinearity to the material generated nonlinearity could be estimated by careful calibration of the generating transducer, and could also be added to the curve-fitting operation by using a cost function that takes this generating transducer nonlinearity into account. This would provide the complete modeling picture, but would likely require careful tuning of the optimization process to deal with the added cost function complexity.

While this work details a more refined process for calculating the nonlinearity param-

eter from Rayleigh wave experimental results than in previous works, more experimental information could facilitate more accurate estimations of the fitting parameters. Measurement of the attenuation at the fundamental and second harmonics could serve to either confirm or directly substitute these values in the model, meaning fewer parameters to fit and thus more accuracy from the model. In addition, directly measuring the source strengths with the laser vibrometer before each data collection would allow for substitution of that information into the analytical formulation, leaving just the nonlinear parameter as the sole fitting variable. Essentially this boils down to reducing the number of optimization variables through careful experimental calibration and characterization, leaving the only optimization parameter as the desired output (β or β_{11}) to increase accuracy and speed.

One factor that is unknown in the procedure implemented in this work for Rayleigh wave modeling is the phase relationship between the fundamental and harmonic components of the source. This work treats these components as having the same phase, however phase differential could slightly alter the value of β_{11} calculated from the curve fitting procedure. While the reasonableness of the results in this work validate the assumption about the relative phase, an experimental setup that could accurately and repeatably calculate this quantity would answer this question definitively.

Ultimately, the most valuable future contribution to this work would be the development of an alternate modeling framework other than RSI modeling for use in the calculation of the pressure wavefield from the leaked wave in air from Rayleigh wave propagation. The incredibly large resource cost of computing the modeling over and over again in an optimization algorithm is prohibitive to the point of making the process impossible in most practical environments, and therefore other modeling frameworks or simplifications need to be made to realize the measurement of absolute material nonlinearity in Rayleigh wave setups with air-coupled receiver technology. Bring this computational cost down would enable a powerful new method of NLU measurement for the NDE community that is sorely lacking from the current range of available tools.

7.3 Significance and Impact

This work provides the first use of air-coupled ultrasonic receivers for use in absolute NLU measurements, a need which addresses a crucial shortcoming in the available tools for NDE technicians in diagnosing material and component health and remaining life estimates. In order to accomplish this, a number of improvements to existing modeling methods were developed, including the adaptation of MGB modeling of second harmonic waves to multiple materials by accounting for acoustic propagation of harmonics across interfaces. Another modeling improvement is the correction of air-coupled Rayleigh wave SHG measurements for diffraction and attenuation in the sample over the propagation path. Additionally, a new calibration methodology was proposed for the characterization of air-coupled piezoelectric transducers with numerous advantages over old methods, such as improved SNR for cleaner calibration curves and the removal of reciprocity as a requirement on the receiver. This calibration enables absolute measurements of material nonlinearity to be made in longitudinal and Rayleigh configurations with proper modeling support. Measurements of absolute β and β_{11} is crucially important for NDE purposes, particularly for health monitoring and end-of-life prediction of old, in-use structures with no baseline NLU measurements on record. Additional uses of this capability include fabrication quality control, when the baseline measurement is the *only* measurement that exists and useful material information is required from a single measurement point. While absolute nonlinearity measurements existed before this work, the use of air-coupled ultrasonic receivers removes many of the barriers to implementation, such as repeatability of measurements, preparation of surfaces, and expense of equipment. By negating these roadblocks, air-coupled SHG measurements have the power to take NLU from the laboratory the field and provide insight into the life-cycle of countless engineering materials and structures.

REFERENCES

[1] J. Herrmann, J.-Y. Kim, L. J. Jacobs, J. Qu, J. W. Littles, and M. F. Savage, "Assessment of material damage in a nickel-base superalloy using nonlinear rayleigh surface waves," *Journal of Applied Physics*, vol. 99, no. 12, pp. 124 913–124 913, 2006.

[2] J.-Y. Kim, L. J. Jacobs, J. Qu, and J. W. Littles, "Experimental characterization of fatigue damage in a nickel-base superalloy using nonlinear ultrasonic waves," *The Journal of the Acoustical Society of America*, vol. 120, no. 3, pp. 1266–1273, 2006.

[3] S. V. Walker, J.-Y. Kim, J. Qu, and L. J. Jacobs, "Fatigue damage evaluation in a36 steel using nonlinear rayleigh surface waves," *NDT & E International*, vol. 48, pp. 10–15, 2012.

[4] T. Apple, J. Cantrell, C. Amaro, C. Mayer, W. Yost, S. Agnew, and J. Howe, "Acoustic harmonic generation from fatigue-generated dislocation substructures in copper single crystals," *Philosophical Magazine*, vol. 93, no. 21, pp. 2802–2825, 2013.

[5] M. Liu, J.-Y. Kim, L. Jacobs, and J. Qu, "Experimental study of nonlinear rayleigh wave propagation in shot-peened aluminum plates—feasibility of measuring residual stress," *NDT & E International*, vol. 44, no. 1, pp. 67–74, 2011.

[6] A. Ruiz, N. Ortiz, A. Medina, J.-Y. Kim, and L. Jacobs, "Application of ultrasonic methods for early detection of thermal damage in 2205 duplex stainless steel," *NDT & E International*, vol. 54, pp. 19–26, 2013.

[7] D. Barnard, G. Dace, and O. Buck, "Acoustic harmonic generation due to thermal embrittlement of inconel 718," *Journal of Nondestructive Evaluation*, vol. 16, no. 2, pp. 67–75, 1997.

[8] J. S. Valluri, K. Balasubramaniam, and R. V. Prakash, "Creep damage characterization using non-linear ultrasonic techniques," *Acta Materialia*, vol. 58, no. 6, pp. 2079–2090, 2010.

[9] K. Matlack, J. Wall, J.-Y. Kim, J. Qu, L. Jacobs, and H.-W. Viehrig, "Evaluation of radiation damage using nonlinear ultrasound," *Journal of Applied Physics*, vol. 111, no. 5, pp. 054 911–054 911, 2012.

[10] M. Breazeale and D. Thompson, "Finite-amplitude ultrasonic waves in aluminum," *Applied Physics Letters*, vol. 3, no. 5, pp. 77–78, 1963.

[11] A. Gedroitz, V. Krasilnikov, and L. Zarembo, "Elastic waves of finite amplitude in solids and anharmonicity of the lattice," *Acta Acustica united with Acustica*, vol. 13, no. 2, pp. 108–110, 1963.

[12] M. Breazeale and J. Ford, "Ultrasonic studies of nonlinear behavior of solids," *Journal of Applied Physics*, vol. 36, no. 11, p. 3486, 1965.

[13] A. Hikata, B. B. Chick, and C. Elbaum, "Dislocation contribution to the second harmonic generation of ultrasonic waves," *Journal of Applied Physics*, vol. 36, no. 1, pp. 229–236, 1965.

[14] A. Hikata and C. Elbaum, "Generation of ultrasonic second and third harmonics due to dislocations. i," *Physical Review*, vol. 144, no. 2, p. 469, 1966.

[15] D. Thompson, O. Buck, R. Barnes, and H. Huntington, "Diffusional properties of the stage-iii defect in copper. i. experimental results," *Journal of Applied Physics*, vol. 38, no. 8, pp. 3051–3056, 1967.

[16] D. Thompson, O. Buck, H. Huntington, and P. Barnes, "Diffusional properties of the stage-iii defect in copper. ii. a model for defect-dislocation interactions," *Journal of Applied Physics*, vol. 38, no. 8, pp. 3057–3067, 1967.

[17] W. B. Gauster and M. Breazeale, "Ultrasonic measurement of the nonlinearity parameters of copper single crystals," *Physical Review*, vol. 168, no. 3, p. 655, 1968.

[18] A. Viswanath, B. P. C. Rao, S. Mahadevan, P. Parameswaran, T. Jayakumar, and B. Raj, "Nondestructive assessment of tensile properties of cold worked AISI type 304 stainless steel using nonlinear ultrasonic technique," *Journal of Materials Processing Technology*, vol. 211, no. 3, pp. 538–544, 2011.

[19] S. Thiele, J.-Y. Kim, J. Qu, and L. J. Jacobs, "Air-coupled detection of nonlinear rayleigh surface waves to assess material nonlinearity," *Ultrasonics*, vol. 54, no. 6, pp. 1470–1475, 2014.

[20] D. Torello, S. Thiele, K. H. Matlack, J.-Y. Kim, J. Qu, and L. J. Jacobs, "Diffraction, attenuation, and source corrections for nonlinear Rayleigh wave ultrasonic measurements," *Ultrasonics*, vol. 56, pp. 417–426, 2015.

[21] D. C. Hurley, D. Balzar, and P. T. Purtscher, "Nonlinear ultrasonic assessment of precipitation hardening in astm a710 steel," *Journal of Materials Research*, vol. null, pp. 2036–2042, Sep. 2000.

[22] C. Desilets, J. Fraser, and G. S. Kino, "The design of efficient broad-band piezoelectric transducers," *IEEE Transactions on Sonics and Ultrasonics*, vol. 25, no. 3, pp. 115–125, 1978.

[23] G. S. Kino, *Acoustic waves: Devices, imaging, and analog signal processing*. Prentice-Hall Englewood Cliffs, NJ, 1987, vol. 107.

[24] G. E. Dace, R. B. Thompson, and O. Buck, "Measurement of the acoustic harmonic generation for materials characterization using contact transducers," in *Review of Progress in Quantitative Nondestructive Evaluation. Vol. 11B*, vol. 11, 1992, pp. 2069–2076.

[25] G. Dace, R. B. Thompson, L. J. Brasche, D. K. Rehbein, and O. Buck, "Nonlinear acoustics, a technique to determine microstructural changes in materials," in *Review of progress in quantitative nondestructive evaluation*, Springer, 1991, pp. 1685–1692.

[26] A. L. Lopez-Sanchez and L. W. Schmerr Jr, "Determination of an ultrasonic transducer's sensitivity and impedance in a pulse-echo setup," *Ultrasonics, Ferroelectrics, and Frequency Control, IEEE Transactions on*, vol. 53, no. 11, pp. 2101–2112, 2006.

[27] L. Sun, S. S. Kulkarni, J. D. Achenbach, and S. Krishnaswamy, "Technique to minimize couplant-effect in acoustic nonlinearity measurements," *The Journal of the Acoustical Society of America*, vol. 120, no. 5, pp. 2500–2505, 2006.

[28] M. Treiber, J.-Y. Kim, L. J. Jacobs, and J. Qu, "Correction for partial reflection in ultrasonic attenuation measurements using contact transducers," *The Journal of the Acoustical Society of America*, vol. 125, p. 2946, 2009.

[29] I. Y. Solodov, N. Krohn, and G. Busse, "Can: An example of nonclassical acoustic nonlinearity in solids," *Ultrasonics*, vol. 40, no. 1, pp. 621–625, 2002.

[30] J. Cantrell and K. Salama, "Acoustoelastic characterisation of materials," *International materials reviews*, vol. 36, no. 1, pp. 125–145, 1991.

[31] D. Hurley and C. Fortunko, "Determination of the nonlinear ultrasonic parameter using a michelson interferometer," *Measurement Science and Technology*, vol. 8, no. 6, p. 634, 1997.

[32] W. T. Yost and J. H. Cantrell, "Anomalous nonlinearity parameters of solids at low acoustic drive amplitudes," *Applied Physics Letters*, vol. 94, no. 2, p. 1905, 2009.

[33] H. Ogi, M. Hirao, and S. Aoki, "Noncontact monitoring of surface-wave nonlinearity for predicting the remaining life of fatigued steels," *Journal of Applied Physics*, vol. 90, no. 1, pp. 438–442, 2001.

[34] A. Cobb, M. Capps, C. Duffer, J. Feiger, K. Robinson, and B. Hollingshaus, "Nonlinear ultrasonic measurements with EMATs for detecting pre-cracking fatigue

damage," in *REVIEW OF PROGRESS IN QUANTITATIVE NONDESTRUCTIVE EVALUATION: Volume 31*, AIP Publishing, vol. 1430, 2012, pp. 299–306.

[35] A. Moreau, "Detection of acoustic second harmonics in solids using a heterodyne laser interferometer," *The Journal of the Acoustical Society of America*, vol. 98, no. 5, pp. 2745–2752, 1995.

[36] A. Ruiz and P. B. Nagy, "Laser-ultrasonic surface wave dispersion measurements on surface-treated metals," *Ultrasonics*, vol. 42, no. 1-9, pp. 665–9, Apr. 2004.

[37] C. B. Scruby and L. E. Drain, *Laser ultrasonics techniques and applications*. CRC Press, 1990.

[38] D. Barnard, G. Dace, D. Rehbein, and O. Buck, "Acoustic harmonic generation at diffusion bonds," *Journal of nondestructive evaluation*, vol. 16, no. 2, pp. 77–89, 1997.

[39] F. Ingenito and A. O. Williams, "Calculation of second-harmonic generation in a piston beam," *Journal of the Acoustical Society of America*, vol. 49, pp. 319–328, 1971.

[40] H. Jeong, S. Zhang, D. Barnard, and X. Li, "Significance of accurate diffraction corrections for the second harmonic wave in determining the acoustic nonlinearity parameter," *AIP Advances*, vol. 5, no. 9, p. 097 179, 2015.

[41] D. J. Shull, E. E. Kim, M. F. Hamilton, and E. A. Zabolotskaya, "Diffraction effects in nonlinear rayleigh wave beams," *The Journal of the Acoustical Society of America*, vol. 97, no. 4, pp. 2126–2137, 1995.

[42] I. A. Viktorov, *Rayleigh and lamb waves: Physical theory and applications*. Plenum press, 1970.

[43] D. J. Shull, M. F. Hamilton, Y. A. Il'insky, and E. A. Zabolotskaya, "Harmonic generation in plane and cylindrical nonlinear rayleigh waves," *The Journal of the Acoustical Society of America*, vol. 94, no. 1, pp. 418–427, 1993.

[44] R. Smith, R. Stern, and R. Stephens, "Third-order elastic moduli of polycrystalline metals from ultrasonic velocity measurements," *The Journal of the Acoustical Society of America*, vol. 40, p. 1002, 1966.

[45] D. C. Hurley, "Nonlinear propagation of narrow-band rayleigh waves excited by a comb transducer," *The Journal of the Acoustical Society of America*, vol. 106, p. 1782, 1999.

[46] J. H. Cantrell and W. T. Yost, "Acoustic harmonic generation from fatigue-induced dislocation dipoles," *Philosophical magazine A*, vol. 69, no. 2, pp. 315–326, 1994.

[47] W. Cash and W. Cai, "Dislocation contribution to acoustic nonlinearity: The effect of orientation-dependent line energy," *Journal of Applied Physics*, vol. 109, no. 1, p. 014 915, 2011.

[48] J. A. Bains Jr and M. Breazeale, "Nonlinear distortion of ultrasonic waves in solids: Approach of a stable backward sawtooth," *The Journal of the Acoustical Society of America*, vol. 57, no. 3, pp. 745–746, 1975.

[49] J. Zhang, F.-z. Xuan, and Y. Xiang, "Dislocation characterization in cold rolled stainless steel using nonlinear ultrasonic techniques: A comprehensive model," *EPL (Europhysics Letters)*, vol. 103, no. 6, p. 68 003, 2013.

[50] J. Zhang and F.-Z. Xuan, "Fatigue damage evaluation of austenitic stainless steel using nonlinear ultrasonic waves in low cycle regime," *Journal of Applied Physics*, vol. 115, no. 20, p. 204 906, 2014.

[51] J. H. Cantrell and X.-G. Zhang, "Nonlinear acoustic response from precipitate-matrix misfit in a dislocation network," *Journal of applied physics*, vol. 84, no. 10, pp. 5469–5472, 1998.

[52] J. H. Cantrell and W. T. Yost, "Determination of precipitate nucleation and growth rates from ultrasonic harmonic generation," *Applied Physics Letters*, vol. 77, no. 13, pp. 1952–1954, 2000.

[53] J. H. Cantrell, "Quantitative assessment of fatigue damage accumulation in wavy slip metals from acoustic harmonic generation," *Philosophical Magazine*, vol. 86, no. 11, pp. 1539–1554, 2006.

[54] S. Hirose and J. Achenbach, "Higher harmonics in the far field due to dynamic crack-face contacting," *The Journal of the Acoustical Society of America*, vol. 93, no. 1, pp. 142–147, 1993.

[55] J.-Y. Kim and J.-S. Lee, "A micromechanical model for nonlinear acoustic properties of interfaces between solids," *Journal of applied physics*, vol. 101, no. 4, p. 043 501, 2007.

[56] V. E. Nazarov and A. M. Sutin, "Nonlinear elastic constants of solids with cracks," *The Journal of the Acoustical Society of America*, vol. 102, no. 6, pp. 3349–3354, 1997.

[57] Y. Zhao, Y. Qiu, L. J. Jacobs, and J. Qu, "A micromechanics model for the acoustic nonlinearity parameter in solids with distributed microcracks," in *42ND AN-*

NUAL REVIEW OF PROGRESS IN QUANTITATIVE NONDESTRUCTIVE EVALUATION: Incorporating the 6th European-American Workshop on Reliability of NDE, AIP Publishing, vol. 1706, 2016, p. 060 001.

[58] J. K. Na and M. A. Breazeale, "Ultrasonic nonlinear properties of lead zirconate-titanate ceramics," *The Journal of the Acoustical Society of America*, vol. 95, no. 6, pp. 3213–3221, 1994.

[59] J. Kim, K.-J. Lee, and K.-Y. Jhang, "Comparison of ultrasonic nonlinear parameters measured by pzt and linbo3 transducers," in *42ND ANNUAL REVIEW OF PROGRESS IN QUANTITATIVE NONDESTRUCTIVE EVALUATION: Incorporating the 6th European-American Workshop on Reliability of NDE*, AIP Publishing, vol. 1706, 2016, p. 060 008.

[60] D. J. Barnard and S. K. Chakrapani, "Measurement of nonlinearity parameter of water using commercial immersion transducers," in *42ND ANNUAL REVIEW OF PROGRESS IN QUANTITATIVE NONDESTRUCTIVE EVALUATION: Incorporating the 6th European-American Workshop on Reliability of NDE*, AIP Publishing, vol. 1706, 2016, p. 060 004.

[61] G. Shui, J.-Y. Kim, J. Qu, Y.-S. Wang, and L. J. Jacobs, "A new technique for measuring the acoustic nonlinearity of materials using rayleigh waves," *NDT & E International*, vol. 41, no. 5, pp. 326–329, Jul. 2008.

[62] M. Hirao and H. Ogi, "An sh-wave emat technique for gas pipeline inspection," *NDT & E International*, vol. 32, no. 3, pp. 127–132, 1999.

[63] R. Ribichini, F. Cegla, P. B. Nagy, and P. Cawley, "Study and comparison of different emat configurations for sh wave inspection," *Ultrasonics, Ferroelectrics, and Frequency Control, IEEE Transactions on*, vol. 58, no. 12, pp. 2571–2581, 2011.

[64] I. T. Incorporated. (). Emat technology.

[65] J. H. Cantrell and W. T. Yost, "Nonlinear ultrasonic characterization of fatigue microstructures," *International Journal of fatigue*, vol. 23, pp. 487–490, 2001.

[66] W. T. Yost and J. H. Cantrell, "The effects of fatigue on acoustic nonlinearity in aluminum alloys," in *Ultrasonics Symposium, 1992. Proceedings., IEEE 1992*, IEEE, 1992, pp. 947–955.

[67] S. Thiele, K. H. Matlack, J.-Y. Kim, J. Qu, J. J. Wall, and L. J. Jacobs, "Assessment of precipitation in alloy steel using nonlinear rayleigh surface waves," in *40TH ANNUAL REVIEW OF PROGRESS IN QUANTITATIVE NONDESTRUCTIVE EVALUATION: Incorporating the 10th International Conference on Barkhausen Noise and Micromagnetic Testing*, AIP Publishing, vol. 1581, 2014, pp. 682–689.

[68] M. Castaings and P. Cawley, "The generation, propagation, and detection of lamb waves in plates using air-coupled ultrasonic transducers," *The Journal of the Acoustical Society of America*, vol. 100, no. 5, pp. 3070–3077, 1996.

[69] W. Grandia and C. Fortunko, "Nde applications of air-coupled ultrasonic transducers," in *Ultrasonics Symposium, 1995. Proceedings., 1995 IEEE*, IEEE, vol. 1, 1995, pp. 697–709.

[70] J. Zhu, J. S. Popovics, and F. Schubert, "Leaky rayleigh and scholte waves at the fluid–solid interface subjected to transient point loading," *The Journal of the Acoustical Society of America*, vol. 116, no. 4, pp. 2101–2110, 2004.

[71] M. Deighton, A. Gillespie, R. Pike, and R. Watkins, "Mode conversion of rayleigh and lamb waves to compression waves at a metal-liquid interface," *Ultrasonics*, vol. 19, no. 6, pp. 249–258, 1981.

[72] C. Ramadas, A. Hood, I. Khan, and K. Balasubramaniam, "Effect of misalignment of air-coupled probes on A0 lamb mode propagating in a metal plate," *Ultrasonics*, vol. 54, no. 5, pp. 1401–1408, 2014.

[73] L. E. Kinsler, A. R. Frey, A. B. Coppens, and J. V. Sanders, *Fundamentals of acoustics*, 4th. Hoboken, NJ: John Wiley & Sons, 1999.

[74] S. Biwa, S. Nakajima, and N. Ohno, "On the acoustic nonlinearity of solid-solid contact with pressure-dependent interface stiffness," *Journal of applied mechanics*, vol. 71, no. 4, pp. 508–515, 2004.

[75] D. Torello and F. L. Degertekin, "Actuation of atomic force microscopy microcantilevers using contact acoustic nonlinearities," *Review of Scientific Instruments*, vol. 84, no. 11, p. 113 705, 2013.

[76] T. Oberhardt, J.-Y. Kim, J. Qu, and L. J. Jacobs, "A contact mechanics based model for partially-closed randomly distributed surface microcracks and their effect on acoustic nonlinearity in rayleigh surface waves," in *AIP Conference Proceedings*, AIP Publishing, vol. 1706, 2016, p. 020 024.

[77] O. Buck, W. Morris, and J. M. Richardson, "Acoustic harmonic generation at unbonded interfaces and fatigue cracks," *Applied Physics Letters*, vol. 33, no. 5, pp. 371–373, 1978.

[78] S. Liu, A. J. Croxford, S. A. Neild, and Z. Zhou, "Effects of experimental variables on the nonlinear harmonic generation technique," *IEEE transactions on ultrasonics, ferroelectrics, and frequency control*, vol. 58, no. 7, 2011.

[79] K. Lee, J. Kim, J. Lee, and K. Jhang, "Experimental comparison of ultrasonic nonlinearity measured by PZT and LiNbO3 transducers," in *Proceedings of 3rd International Conference on Materials and Reliability*, Jun. 2015.

[80] Y. Cho and K. Yamanouchi, "Nonlinear, elastic, piezoelectric, electrostrictive, and dielectric constants of lithium niobate," *Journal of applied physics*, vol. 61, no. 3, pp. 875–887, 1987.

[81] Y. Nakagawa, K. Yamanouchi, and K. Shibayama, "Third-order elastic constants of lithium niobate," *Journal of Applied Physics*, vol. 44, no. 9, pp. 3969–3974, 1973.

[82] J. Philip and M. Breazeale, "Ultrasonic harmonic generation in trigonal crystals: Measurements in LiNbO3," in *1982 Ultrasonics Symposium*, IEEE, 1982, pp. 1022–1025.

[83] W. Jiang and W. Cao, "Nonlinear properties of lead zirconate–titanate piezoceramics," *Journal of Applied Physics*, vol. 88, no. 11, pp. 6684–6689, 2000.

[84] G. Petersen, "L-matching the output of a ritec gated amplifier to an arbitrary load," *RITEC Inc., USA*, p. 8, 2006.

[85] P. H. Rogers and A. L. V. Buren, "An exact expression for the lommel-diffraction correction integral," *The Journal of the Acoustical Society of America*, vol. 55, no. 4, pp. 724–728, 1974.

[86] A. Williams Jr, "The piston source at high frequencies," *The Journal of the Acoustical Society of America*, vol. 23, no. 1, pp. 1–6, 1951.

[87] A. Ruiz and P. B. Nagy, "Diffraction correction for precision surface acoustic wave velocity measurements," *The Journal of the Acoustical Society of America*, vol. 112, p. 835, 2002.

[88] W. N. Cobb, "Finite amplitude method for the determination of the acoustic nonlinearity parameter b/a," *The Journal of the Acoustical Society of America*, vol. 73, no. 5, pp. 1525–1531, 1983.

[89] D. Kourtiche, L. Allies, M. Nadi, and A. Chitnalah, "Influences and simplifications of diffraction func-tions in nonlinear acoustical parameter measure-ment systems," *Int J Acoust Vib*, vol. 13, no. 4, pp. 151–6, 2008.

[90] A. D. Pierce, *Acoustics: An introduction to its physical principles and applications*. Acoustical Society of America Melville, NY, 1991.

[91] L. Schmerr and J.-S. Song, *Ultrasonic nondestructive evaluation systems*. Springer, 2007.

[92] L. Greengard and V. Rokhlin, "A fast algorithm for particle simulations," *Journal of computational physics*, vol. 73, no. 2, pp. 325–348, 1987.

[93] L. Grengard and V. Rokhlin, "The rapid evaluation of potential fields in three dimensions," in *Vortex Methods*, Springer, 1988, pp. 121–141.

[94] E. Zabolotskaya and R. Khokhlov, "Quasi-plane waves in the nonlinear acoustics of confined beams," *Sov. Phys. Acoust*, vol. 15, no. 1, pp. 35–40, 1969.

[95] M. F. Hamilton and D. T. Blackstock, *Nonlinear acoustics*. Academic Press San Diego, 1998, vol. 237.

[96] D. Huang and M. Breazeale, "A gaussian finite-element method for description of sound diffraction," *The Journal of the Acoustical Society of America*, vol. 106, no. 4, pp. 1771–1781, 1999.

[97] J. Wen and M. Breazeale, "A diffraction beam field expressed as the superposition of gaussian beams," *The Journal of the Acoustical Society of America*, vol. 83, no. 5, pp. 1752–1756, 1988.

[98] J.-J. Wen and M. Breazeale, "Computer optimization of the gaussian beam description of an ultrasonic field," *Computational Acoustics*, vol. 2, p. 181, 1990.

[99] S. Zhang, H. Jeong, S. Cho, and X. Li, "Simultaneous evaluation of acoustic nonlinearity parameter and attenuation coefficients using the finite amplitude method," *AIP Advances*, vol. 5, no. 7, p. 077 133, 2015.

[100] L. W. Schmerr and A. Sedov, "A modular multi-gaussian beam model for isotropic and anisotropic media," in *AIP CONFERENCE PROCEEDINGS*, IOP INSTITUTE OF PHYSICS PUBLISHING LTD, 2003, pp. 828–835.

[101] X. Zhao, L. W. Schmerr Jr, A. Sedov, and X. Li, "Simulation of ultrasonic surface waves with multi-gaussian and point source beam models," in *40TH ANNUAL REVIEW OF PROGRESS IN QUANTITATIVE NONDESTRUCTIVE EVALUATION: Incorporating the 10th International Conference on Barkhausen Noise and Micromagnetic Testing*, AIP Publishing, vol. 1581, 2014, pp. 556–562.

[102] S. Thiele, "Air-coupled detection of rayleigh surface waves to assess material nonlinearity due to precipitation in alloy steel," Master's thesis, Georgia Institute of Technology, Dec. 2013.

[103] J. H. Cantrell Jr and M. Breazeale, "Ultrasonic investigation of the nonlinearity of fused silica for different hydroxyl-ion contents and homogeneities between 300 and 3 K," *Physical Review B*, vol. 17, no. 12, p. 4864, 1978.

[104] P. Li, W. Yost, J. Cantrell, and K. Salama, "Dependence of acoustic nonlinearity parameter on second phase precipitates of aluminum alloys," in *IEEE 1985 Ultrasonics Symposium*, Oct. 1985, pp. 1113–1115.

[105] W. T. Yost and J. H. Cantrell, "The effects of artificial aging of aluminum 2024 on its nonlinearity parameter," in *Review of Progress in Quantitative Nondestructive Evaluation*, D. O. Thompson and D. E. Chimenti, Eds., Springer, 1993, pp. 2067–2073.

[106] D. Ensminger and L. J. Bond, *Ultrasonics: Fundamentals, technologies, and applications*. CRC Press, 2011.

[107] Y. Xiang, M. Deng, F.-Z. Xuan, and C.-J. Liu, "Experimental study of thermal degradation in ferritic cr–ni alloy steel plates using nonlinear lamb waves," *NDT & E International*, vol. 44, no. 8, pp. 768–774, 2011.